Author/s:
Petrie, SM;Butler, J;Barr, IG;McVernon, J;Hurt, AC;McCaw, JM

Title:
Quantifying relative within-host replication fitness in influenza virus competition experiments

Date:
2015-01-01

Citation:
Petrie, S. M., Butler, J., Barr, I. G., McVernon, J., Hurt, A. C. & McCaw, J. M. (2015). Quantifying relative within-host replication fitness in influenza virus competition experiments. Journal of Theoretical Biology, 382, pp.259-271. https://doi.org/10.1016/j.jtbi.2015.07.003.

Persistent Link:
https://hdl.handle.net/11343/56642

Quantifying relative within-host replication fitness in influenza virus competition experiments

Stephen M. Petrie[a], Jeff Butler[b], Ian G. Barr[b,c], Jodie McVernon[a,d], Aeron C. Hurt[b,c], James M. McCaw[a,d,e,*]

[a] *Melbourne School of Population and Global Health, The University of Melbourne, Parkville, Victoria, Australia*
[b] *WHO Collaborating Centre for Reference and Research on Influenza, Victorian Infectious Diseases Reference Laboratory at the Peter Doherty Institute for Infection and Immunity, Melbourne, Victoria, Australia*
[c] *School of Applied Sciences, Monash University, Churchill, Victoria, Australia*
[d] *Murdoch Childrens Research Institute, The Royal Children's Hospital, Parkville, Victoria, Australia*
[e] *School of Mathematics and Statistics, The University of Melbourne, Parkville, Victoria, Australia*

Abstract

Through accumulation of genetic mutations in the neuraminidase gene, the influenza virus can become resistant to antiviral drugs such as oseltamivir. Quantifying the fitness of emergent drug-resistant influenza viruses, relative to contemporary circulating viruses, provides valuable information to complement existing efforts in the surveillance of drug-resistance. We have previously developed a co-infection based method for the assessment of the relative *in vivo* fitness of two competing viruses. We have also introduced a model of within-host co-infection dynamics that enables relative within-host fitness to be quantified in these competitive-mixtures experiments. The model assumed that fitness differences between co-infecting strains were mediated by strain-dependent viral production rates from infected epithelial cells. Here we extend the model to enable a more complete exploration of biological processes that may differ between virus pairs and hence generate fitness differences. We use the extended model to re-analyse data from competitive-mixtures experiments that investigated the fitness of oseltamivir-resistant (OR) H1N1 pandemic 2009 ("H1N1pdm09") viruses that emerged during a community outbreak in Australia in 2011. Results are consistent with those of our previous analysis, suggesting that the within-host replication fitness of these OR viruses is not compromised relative to that of related oseltamivir-susceptible (OS) strains, and that potentially permissive mutations in the neuraminidase gene (V241I and N369K) significantly enhance the fitness of H1N1pdm09 OR viruses. These results are consistent regardless of the hypothesised biological cause of fitness difference.

Keywords: influenza, mathematical model, viral kinetics, drug-resistance, pathogen fitness

---

1. Introduction

Antiviral drugs are used to treat influenza infection and reduce the onward spread of infection [1, 2, 3]. Currently circulating influenza viruses are predominantly susceptible to the neuraminidase (NA) inhibitor oseltamivir, however the drug's utility as a treatment option for influenza may be severely compromised if resistance becomes prevalent [4]. During the Northern Hemisphere's 2007/08 influenza season, surveillance studies identified a rise in the proportion of A(H1N1) viruses carrying the resistance-conferring H275Y mutation in the NA gene [5, 6, 7, 8]. These resistant viruses spread globally and replaced wild-type H1N1 during 2008 [9, 10, 11, 12], largely *independently* of the use of oseltamivir [10, 7, 11, 8]. This event highlighted a need to be able to accurately assess the relative fitness of emergent drug-resistant influenza strains compared to contemporary circulating drug-susceptible wild-type strains.

Previous studies have quantified the relative replication fitness of different pathogens using mathematical models [13, 14, 15, 16, 17, 18]. A method introduced by Marée *et al.* [13] quantified relative *in vitro* fitness via the ratio of the infected cell replication rates of each competing strain. Marée *et al.* discussed alternatives to their assumption that the replication rate is the only parameter that differs by strain (e.g. the infected cell death rate could instead be assumed to be the source of strain difference), however other possible biological sources of strain difference were not considered, such as strain-dependence in the latent phase duration. Wu *et al.* [14] quantified relative *in vitro* fitness using the overall growth rate for each strain. This method is difficult to compare across different experiments because the growth rate incorporates the number of target cells, and so changes depending on experimental conditions. Wu *et al.* also did not consider alternative scenarios regarding the source of strain difference. In earlier work [15], we quantified relative *in vivo* fitness via the difference of the infected cell replication rates of each strain. However, we neglected other possible causes of strain difference, such as strain-dependence in the duration of either the latent or productive phase of infected cells. Holder *et al.* [16] and Pinilla *et al.* [17] quantified relative *in vitro* fitness by estimating several fundamental biological properties of each strain, gaining direct insight

---

*Corresponding author
Email address: `jamesm@unimelb.edu.au` (James M. McCaw)

into the underlying cause of strain-dependent infection dynamics and fitness differences. Quantifying relative fitness in this way is preferable to estimating experiment-specific properties that change depending upon modifications to the infection system (e.g. Wu *et al.* [14]), and depending on the biological properties of the pathogens being studied, may also be preferable to assuming that the infected cell replication rate or death rate are the only parameters that differ by strain (e.g. Marée *et al.* [13]).

In a recent experimental study involving the co-infection of animals with competing pairs of A(H1N1) pandemic 2009 ("H1N1pdm09") strains [18], we used a within-host model of the co-infection system to quantify relative replication fitness. The model assumed that fitness differences were caused by strain-dependence in the production rate of infectious virus by infected cells, and relative within-host fitness was quantified via the ratio of the production rates. Results indicated that: (1) H275Y drug-resistant influenza viruses that emerged in 2011 in the Hunter New England (HNE) region of New South Wales, Australia, did not have compromised *in vivo* fitness compared with related drug-sensitive viruses, and (2) the unusually robust fitness of these drug-resistant viruses may have been due to the presence of two permissive NA mutations — V241I and N369K — which have since become established in virtually all circulating H1N1pdm09 viruses. Here we first revisit the model introduced in Butler *et al.* [18], and then extend it to allow investigation of several different biologically plausible hypotheses regarding the cause of fitness difference. Of note, our focus throughout the analysis is to obtain accurate and precise estimates for the relative fitness, rather than individual model parameters.

2. Experimental data

We analyse data from a competitive-mixtures experimental study involving co-infection of ferrets with pairs of competing influenza viruses [18]. In these experiments, immunologically naive ferrets were inoculated with various mixtures of two different influenza strains ("A" and "B"). Each ferret was assigned either to one of three "mixed-infection groups" (80A:20B, 50A:50B, and 20A:80B), or to one of two "pure-infection groups" (100A:0B and 0A:100B). Each inoculum was prepared at the required proportion by combining known concentrations of each virus.

Nasal wash samples were taken daily from each ferret. The infectious viral load of each sample was measured using 50% tissue culture infectious dose (TCID_{50}) assays, and total (infectious + non-infectious) viral load was measured using real-time reverse transcription-polymerase chain reaction (rRT-PCR) assays of the matrix gene. The *proportion* of each co-infecting virus was also measured using pyrosequencing assays of the NA gene of each co-infecting strain. Dynamics in this vRNA proportion over the course of infection provide insight into relative replication fitness within the mixed-infection groups. Differences in viral load dynamics between the two pure-infection groups also provide insight into relative replication fitness. Pyrosequencing and rRT-PCR measurements were taken for each inoculum.

Reverse genetics techniques were used to generate drug-resistant viruses with or without certain potentially permissive NA mutations — V241I and N369K — that were hypothesised to have counteracted the fitness cost of the H275Y mutation. The different virus pairs investigated in each competitive-mixtures experiment are shown in Table 1, and full details of the experimental procedures have previously been presented [18].

3. Within-host co-infection model

Epithelial cells infected with influenza produce both infectious and non-infectious virus. In order to model competitive-mixtures experiments, we extended our previous model of infectious and non-infectious influenza viral dynamics [19] to incorporate two different co-infecting strains [18]. This "co-infection" model (Figure 1) assumes that target cells (T) may be infected by either strain A ($V_A^{\scriptscriptstyle TCID}$) or strain B ($V_B^{\scriptscriptstyle TCID}$) infectious virions; i.e. each strain competes for the same target cell resources [18]:

$$\frac{dT}{dt} = -\beta_A T V_A^{\scriptscriptstyle TCID} - \beta_B T V_B^{\scriptscriptstyle TCID}. \tag{1}$$

For each strain, infected target cells progress through a latent phase (L) before becoming infectious (I) as described by the following equations [18]:

$$\begin{aligned}
\frac{dL_A}{dt} &= \beta_A T V_A^{\scriptscriptstyle TCID} - k_A L_A \\
\frac{dL_B}{dt} &= \beta_B T V_B^{\scriptscriptstyle TCID} - k_B L_B \\
\frac{dI_A}{dt} &= k_A L_A - \delta_A I_A \\
\frac{dI_B}{dt} &= k_B L_B - \delta_B I_B \\
\frac{dV_A^{\scriptscriptstyle TCID}}{dt} &= p_A I_A - c_{h,A} V_A^{\scriptscriptstyle TCID} - d_{inf,A} V_A^{\scriptscriptstyle TCID} \\
\frac{dV_B^{\scriptscriptstyle TCID}}{dt} &= p_B I_B - c_{h,B} V_B^{\scriptscriptstyle TCID} - d_{inf,B} V_B^{\scriptscriptstyle TCID} \\
\frac{dV_A^{\scriptscriptstyle RNA}}{dt} &= \xi_A p_A I_A - c_{h,A} V_A^{\scriptscriptstyle RNA} \\
\frac{dV_B^{\scriptscriptstyle RNA}}{dt} &= \xi_B p_B I_B - c_{h,B} V_B^{\scriptscriptstyle RNA}.
\end{aligned} \tag{2}$$

Details of all state variables and parameters in this model are shown in Table 2, together with fixed parameter values and the biologically realistic bounds used to constrain fitted parameters. In order to produce more biologically accurate distributions for the latent and infected cell lifespans, the L and I compartments are each split into 20 stages, for both strain A and strain B [19]. The model is similar to that used by Pinilla *et al.* [17] to model competition between co-infecting strains in cell culture.

4. Fitting the model to data

When fitting model outputs to experimental data, three different assay types are used:

Table 1: **Virus pairs analysed in [18].** Each row shows the virus pair ("A" vs. "B") analysed in a given competitive-mixtures experiment, together with a description of each virus. One experiment involved naturally isolated viruses (row 1) while the other experiments involved viruses generated using reverse genetics (rg) techniques (rows 2–5). All oseltamivir-resistant (OR) viruses contained the H275Y NA mutation (tyrosine (Y) at position 275), whereas the oseltamivir-susceptible (OS) virus did not contain that mutation (histidine (H) at position 275).

A	B	Description
New17 OR	New163 OS	An OR virus isolated from the HNE outbreak (A/Newcastle/17/2011), paired with an OS wild-type virus isolated during the same outbreak (A/Newcastle/163/2011).
rgNew17 OR	rgNew17 I241V OR	A virus genetically identical to the New17 OR isolate which naturally encodes the V241I and N369K NA substitutions (rgNew17 OR), paired with the same virus except with V241I removed (rgNew17 I241V OR).
rgNew17 OR	rgNew17 K369N OR	The rgNew17 OR virus, paired with the same virus except with N369K removed (rgNew17 K369N OR).
rgNew17 OR	rgNew17 K369N,I241V OR	The rgNew17 OR virus, paired with the same virus except with both V241I and N369K removed (rgNew17 I241V, K369N OR).
rgPerth261 N369K,V241I OR	rgPerth261 OR	A virus genetically identical to an early (2009) OR isolate, A/Perth/261/2009, which does *not* naturally encode the V241I and N369K NA substitutions (rgPerth261 OR), paired with the same virus except containing the V241I and N369K mutations (rgPerth261 V241I, N369K OR).

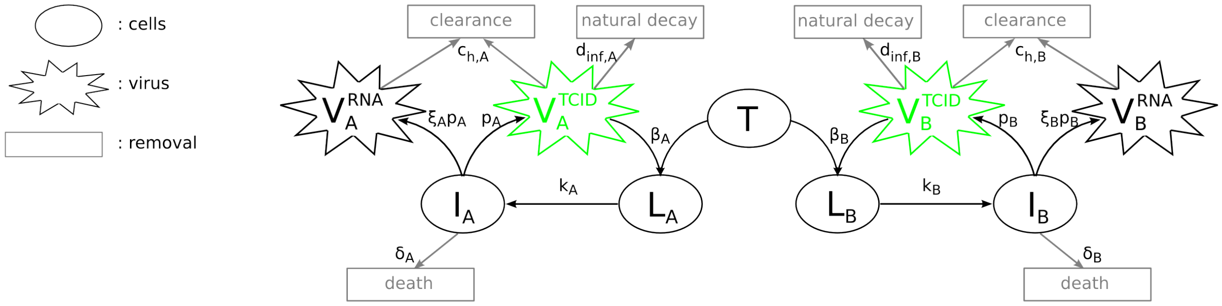

Figure 1: **Co-infection model.** For each strain, infectious virions (V^{TCID}) infect target cells (T) which, following a latent phase (L), become productively infected (I) and release both infectious (V^{TCID}) and total (V^{RNA}) virions. Infectious virions naturally decay into non-infectious virions, and we assume that the natural decay process does not affect vRNA concentration as measured by rRT-PCR assays. Host-driven clearance affects all viral particles. $V^{TCID}_{comb} = V^{TCID}_A + V^{TCID}_B$, $V^{RNA}_{comb} = V^{RNA}_A + V^{RNA}_B$, and $V^{RNA}_B = V^{RNA}_B / V^{RNA}_{comb}$ are fitted to TCID$_{50}$, rRT-PCR, and pyrosequencing data, respectively. For clarity, the colours of the V^{TCID}_A, V^{TCID}_B,V^{RNA}_A , and V^{RNA}_B compartments (green/black) are matched to the colours of the corresponding viral load curves in Figure 2. Adapted from the Supplementary Text of Butler *et al.* [18].

Table 2: **Co-infection model states and parameters.** Descriptions of all state variables (compartments) and parameters in the co-infection model (most descriptions are reproduced from the Supplementary Text of Butler *et al.* [18]). Biologically realistic lower and upper bounds for each fitted parameter are also shown; these are used to restrict parameters to realistic values during fitting.

	Description	Units	Fixed value	Fitting bounds	Source[a]
T	number of target cells	*cells*	–	–	–
$T(0)$	initial T value	*cells*	7×10^7	–	This estimate was calculated in our previous within-host modelling study of ferret infection [19].
L	number of latently infected cells	*cells*	–	–	–
$L(0)$	initial L value	*cells*	0	–	–
I	number of productively infected cells	*cells*	–	–	–
$I(0)$	initial I value	*cells*	0	–	–
V^{TCID}	concentration of free infectious virions measured via TCID$_{50}$ infectivity assay	$TCID_{50}/ml$ *of nasal wash*	–	–	–
$V^{TCID}(0)$	initial V^{TCID} concentration	$TCID_{50}/ml$	–	$[10^{-6}, 10^{4.699}]$	Upper bound based on a scenario in which *all* infectious virus in each inoculum given to donor ferrets — i.e. $10^{4.699}$ $TCID_{50}$ — is taken up into the URT. Hypothetically, if a nasal wash sample had been taken from a donor immediately after inoculation, it would be impossible for there to be more than $10^{4.699}$ $TCID_{50}$ within the 1 *ml* of solution that is used in such a nasal wash. Lower bound based on a previous theoretical estimate of the lowest possible TCID$_{50}$ value that corresponds to a single infectious virion in the URT [19].
V^{RNA}	concentration of free vRNA (present in both infectious and non-infectious virus) measured via RT-PCR assay	*vRNA copies*/*ml*	–	–	–
p	production rate of infectious virions	$(TCID_{50}/ml)\ cell^{-1}\ d^{-1}$	–	$[10^{-4}, 10^{2}]$	Previous *in vivo* and *in vitro* modelling estimates of p [22, 23, 24, 25, 26, 27, 28, 29, 30, 31].
β	infectivity/mixing rate governing infection of target cells by infectious virions	$(TCID_{50}/ml)^{-1}\ d^{-1}$	–	$[10^{-9}, 10^{-1}]$	Previous *in vivo* and *in vitro* modelling estimates of β [22, 23, 24, 25, 26, 27, 28, 30, 31].
k	transition rate from latent to productive infection	d^{-1}	–	$[1, 24]$	This range corresponds to average latently infected cell lifetimes (i.e. $\tau_L = 1/k$) from 1 *h* to 24 *h*, consistent with previous estimates obtained when fitting models (with normal or log-normal delay distributions for L and I) to *in vitro* data [29, 16, 17].
δ	death rate of productively infected cells	d^{-1}	–	$[0.24, 8]$	This range corresponds to average productively infected cell lifetimes (i.e. $\tau_I = 1/\delta$) from 3 *h* to 100 *h*, consistent with previous *in vitro* observations [32, 33, 22] as well as both *in vivo* and *in vitro* model-fitting estimates [22, 23, 24, 25, 26, 27, 29, 30, 17].
c_h	host-driven clearance rate (assumed to be the same for both infectious and non-infectious virus)	d^{-1}	–	$[10^{-2}, 10^{3}]$	Previous *in vivo* estimates for the clearance rate of infectious virions obtained from target cell-limited models (where infection progress is limited by the availability of susceptible cells, rather than by immune response dynamics) [23, 24, 27, 29, 30][b].
d_{inf}	degradation rate of infectious virus to non-infectious virus	d^{-1}	3.12	–	Consistent with the rate of loss of infectivity determined *in vitro* for two H1N1pdm09 strains [17]. This value is also consistent with other *in vitro* measurements [34, 35, 36, 37, 25, 26, 16].
ξ	ratio of total vRNA measured via rRT-PCR to infectious virions measured via TCID$_{50}$, as produced by infected cells	*vRNA copies*/$TCID_{50}$	–	$[10^{0}, 10^{6}]$	Based on the variability of the rRT-PCR:TCID$_{50}$ ratio within the Butler *et al.* [18] data.
$\rho(0)$	initial total:infectious ratio for both strains combined ($\rho(0) = V^{RNA}_{comb}(0)/V^{TCID}_{comb}(0)$)	*vRNA copies*/$TCID_{50}$	–	$[10^{0}, 10^{5}]$	Based on the variability of $\rho(0)$ across different inocula given to donor ferrets in Butler *et al.* [18].

---

[a] For reviews of parameter estimates obtained by within-host modelling influenza studies, see [20, 21].

[b] Note that previous estimates of the infectious virus clearance rate (usually referred to as c) implicitly include both c_h and d_{inf}; hence we expect c_h to be somewhat smaller than previous estimates of c.

1. the infectious virus concentration of both strains combined ($V^{TCID}_{comb} = V^{TCID}_{A} + V^{TCID}_{B}$) is fitted to TCID$_{50}$ data;
2. the viral RNA concentration of both strains combined ($V^{RNA}_{comb} = V^{RNA}_{A} + V^{RNA}_{B}$) is fitted to rRT-PCR data;
3. the proportion of viral RNA comprised of strain B ($V^{RNA}_{B}/V^{RNA}_{comb}$) is fitted to pyrosequencing data.

TCID$_{50}$ data were obtained using several separate runs of the assays in [18] (due to the limited number of samples able to be tested with any single assay), and inter-assay variability was controlled for by including, in each assay, 1–2 samples from stocks of control virus. We use these control samples to calibrate all TCID$_{50}$ data. Each measurement in a given assay is scaled up by adding, in log-space, the difference between that assay's average calibration value and the largest average calibration value obtained across all TCID$_{50}$ assays in all experiments.

Initial conditions for T, L, I, and V^{TCID}_{comb} are identical to those used in our previous within-host modelling study of ferret infection [19], i.e. $T(0) = 7 \times 10^7$, $L(0) = I(0) = 0$ (for each strain), and $V^{TCID}_{comb}(0)$ is a fitted parameter. For each infection group the initial proportion of infectious virus comprised of strain B ($V^{TCID}_{B}(0)/V^{TCID}_{comb}(0)$) is fixed to the proportion prepared in the inoculum. The initial total:infectious ratio for both strains combined ($\rho(0) = V^{RNA}_{comb}(0)/V^{TCID}_{comb}(0)$) is fitted to the rRT-PCR:TCID$_{50}$ ratio as measured in the inoculum. Measurements of the rRT-PCR:TCID$_{50}$ ratio varied systematically across the different mixed inocula, indicating that the two competing strains in a given experiment may have had different ratios. We assume that $\rho(0)$ is strain-dependent, introducing $\rho_A(0)$ and $\rho_B(0)$ as follows:

$$\begin{aligned}\rho(0) &= \frac{V^{RNA}_{comb}(0)}{V^{TCID}_{comb}(0)} = \frac{V^{RNA}_{A}(0) + V^{RNA}_{B}(0)}{V^{TCID}_{comb}(0)}\\ &= \frac{\rho_A(0)V^{TCID}_{A}(0) + \rho_B(0)V^{TCID}_{B}(0)}{V^{TCID}_{comb}(0)}\\ &= \rho_A(0)\left(1 - \frac{V^{TCID}_{B}(0)}{V^{TCID}_{comb}(0)}\right) + \rho_B(0)\frac{V^{TCID}_{B}(0)}{V^{TCID}_{comb}(0)}\ .\end{aligned} \tag{3}$$

The initial proportion of total virus comprised of strain B ($V^{RNA}_{B}(0)/V^{RNA}_{comb}(0)$) is fitted to inoculum pyrosequencing data.

For pure-infection group ferrets, the strain omitted from each group's inoculum is assumed to be absent throughout the entire course of infection. Those data are fitted with only a single strain present in the model. This assumption is supported by an inspection of the raw data [18], which suggest that the probability of spontaneous mutation from one strain to the other is low throughout the course of a pure infection. Data from mixed-infection group ferrets are fitted with the full two-strain version of the model.

Measurements that are outside detection thresholds are fitted as previously explained [19]. Pyrosequencing measurements are considered to be outside the threshold of detectability when they are outside the range $[0.02, 0.98]$, as the pyrosequencing error for each experiment was generally around 2%.

Model parameters are estimated by minimising the sum of squared residuals (SSR) between model outputs and data, using a similar method to previous within-host modelling studies [28, 19]. For a single set of model parameters ($\boldsymbol{\theta}$) the SSR is:

$$\begin{aligned}SSR(\boldsymbol{\theta}) = &\sum_{i=1}^{N_{TCID}}\left(\frac{\log_{10}\hat{V}^{TCID}_{i} - \log_{10}V^{TCID}_{comb}(t_i,\boldsymbol{\theta})}{\log_{10}\hat{V}^{TCID}_{max} - \log_{10}\hat{V}^{TCID}_{thr}}\right)^2\\ &+ \sum_{i=1}^{N_{PCR}}\left(\frac{\log_{10}\hat{V}^{PCR}_{i} - \log_{10}V^{RNA}_{comb}(t_i,\boldsymbol{\theta})}{\log_{10}\hat{V}^{PCR}_{max} - \log_{10}\hat{V}^{PCR}_{thr}}\right)^2\\ &+ \sum_{i=1}^{N_{\rho(0)}}\left(\frac{\log_{10}\hat{\rho}_i(0) - \log_{10}\rho(0,\boldsymbol{\theta})}{\log_{10}\hat{\rho}_{max}(0) - \log_{10}\hat{\rho}_{min}(0)}\right)^2\\ &+ \sum_{i=1}^{N_{pyro}}\left(\hat{V}^{pyro}_{B,i} - V^{RNA}_{B}(t_i,\boldsymbol{\theta})\right)^2,\end{aligned} \tag{4}$$

where N_{TCID}, N_{PCR}, $N_{\rho(0)}$, and N_{pyro} are the number of TCID$_{50}$, rRT-PCR, $\hat{\rho}(0)$ (i.e. rRT-PCR/TCID$_{50}$), and pyrosequencing data points being fitted, respectively; t_i is the time that the ith data point was measured; $\hat{V}^{TCID}_{i}$, $\hat{V}^{PCR}_{i}$, $\hat{\rho}_i(0)$, and $\hat{V}^{pyro}_{B,i}$ denote the ith measurement for each respective assay; $\hat{V}^{TCID}_{max}$, $\hat{V}^{PCR}_{max}$, and $\hat{\rho}_{max}(0)$ are the maximum values that were obtained (for the particular experiment being fitted) across all TCID$_{50}$, rRT-PCR, and $\hat{\rho}(0)$ measurements respectively; $\hat{\rho}_{min}(0)$ is the minimum value that was obtained across all $\hat{\rho}(0)$ measurements; and $\hat{V}^{TCID}_{thr}$ and $\hat{V}^{PCR}_{thr}$ denote detection thresholds for each respective assay.

MATLAB 2011b's genetic algorithm (GA) is used to ensure that a good candidate for the global minimum of the SSR is obtained and to generate likelihood confidence regions (LCRs) and confidence intervals (CIs) for parameter estimates, as detailed previously [19, 38, 39]. The rate of degradation of infectious to non-infectious virus is fixed to $d_{inf} = 3.12\ d^{-1}$; a value estimated previously *in vitro* for two H1N1pdm09 viruses [17]. This value is also consistent with other *in vitro* measurements [34, 35, 36, 37, 25, 26, 16]. For all fitted parameters in the co-infection model, a range of biologically plausible values are specified (Table 2) which restrict the parameter space searchable by the GA. Different hypothesised models are compared statistically using the Akaike information criterion (AIC) in the case of least squares estimation with normally distributed errors [40]. The AIC corrected for datasets with few data points (AIC$_c$) is used.

5. Quantifying relative fitness using ratios of strain-dependent model parameters

Once model parameters have been estimated for each competing strain, relative replication fitness is quantified via the ratio of each pair of strain-dependent parameters. As the underlying biological cause of experimentally observed strain-dependence in infection dynamics is unknown and may differ depending on which two strains are being compared, we investigate several different hypotheses regarding the biological processes that may differ (Section 6). To avoid parameter identifiability issues, each hypothesis is investigated separately by allowing one biological parameter to be strain-dependent at a time, while all other biological parameters are assumed to be equivalent for both strains. Note that $\rho(0)$ is also assumed to be strain-dependent (see Section 4), however that parameter is simply an initial condition of the infection system which is affected by each virus' storage conditions leading up to a given experiment, rather than a fundamental biological property of each virus.

For each hypothesis, strain-dependence in the associated biological parameter generates a fitness difference between strains. Relative fitness is quantified via the ratio of these two strain-dependent parameters. An estimated value of one for the ratio indicates equivalent fitness between the two strains; values either side of one indicate greater or lesser fitness, driven by differences in the parameter under study.

6. Hypothesised explanations for a fitness difference between strains that have distinct NA genes

In the competitive-mixtures experiments analysed here (Table 1) co-infecting viruses differ (primarily or solely) via mutations in the NA gene. Hence the hypothesised causes for a fitness difference that we choose to investigate are informed by previous *in vitro* experiments that examined functions of influenza NA ([41, 42, 43, 44, 45, 46, 47, 48, 49, 50, 51, 52, 53, 54, 55, 56, 57, 58, 59, 60, 61, 62]; summarised in Appendix A).

6.1. The p-diff model

Previous *in vitro* work has indicated the importance of NA in the production of free virions, and in regulating the balance of infectious and non-infectious virions during production from infected cells (see Appendix A). One hypothesis we investigate is that the production rate of infectious virus (p) differs between strains while all other rate parameters are identical for both strains; hence *relative fitness* $= p_B/p_A$. This assumption was made in our previous analysis of these experiments [18]. We refer to the resulting model as the "p-diff" model. Under the p-diff model, a larger estimated value for p indicates greater replication fitness, as a greater rate of production of infectious virus leads to a greater exponential growth rate for infectious virus and infected cells (assuming that target cells are available for infection once progeny virus production begins).

6.2. The β-diff model

Previous experimental results have indicated that NA is important for virus entry into susceptible cells (see Appendix A). Other *in vitro* work has also indicated that NA is important in counteracting the effects of decoy receptors in mucins that (1) restrict the spatial spread of free virus throughout the site of infection, and (2) clear free virus (see Appendix A).

To account for the first of these mucin-counteracting functions of NA, as well as the possibility that NA may affect the infectivity of each infectious virion, we investigate a hypothesis that only the infectivity/mixing rate (β) differs between strains (the "β-diff" model), where *relative fitness* $= \beta_B/\beta_A$. This hypothesis embodies a scenario in which NA counteracts the inhibition of the spatial spread of free virus, and/or alters the infectivity of infectious virions, in a strain-dependent manner. Under the β-diff model, a larger estimated value for β indicates greater replication fitness, as faster spatial spread of infectious virus and/or greater infectivity per virion leads to a greater exponential growth rate for numbers of infected cells.

6.3. The τ_{V}-diff model

To account for the second of the previously mentioned mucin-counteracting functions of NA, we also investigate a hypothesis in which only host-driven clearance (c_h) is strain-dependent. This embodies a scenario in which NA counteracts the host-driven clearance of free virus in a strain-dependent manner. Under this hypothesis, a larger estimated c_h rate indicates that virions are cleared more quickly from the site of infection, leading to a relatively decreased exponential growth rate in numbers of infected cells and a more rapid exponential decay rate for free virus. Larger c_h values are associated with decreased within-host fitness. To aid in presentation we therefore use an alternative parameterisation of host-driven clearance: strain-dependence in the expected lifetime of infectious virions ($\tau_{Vinf} = 1/[c_h + d_{inf}]$, with d_{inf} fixed); hence *relative fitness* $= \tau_{Vinf,B}/\tau_{Vinf,A}$. This hypothesised model is referred to as the "τ_V-diff" model.

6.4. The τ_{I}-diff model

Other *in vitro* work has indicated that NA may be important in determining the lifetime of infected cells (see Appendix A), which in the co-infection model is dependent upon the average duration of both the latent phase ($\tau_L = 1/k$) and productive phase ($\tau_I = 1/\delta$). One way to incorporate this possible function of NA is to investigate a hypothesis in which only δ is strain-dependent. Under this hypothesis, a larger estimated value for δ indicates that infected cells produce infectious virus for shorter durations on average (shorter τ_I), leading to relatively lower amounts of free infectious virus, a decreased rate of exponential growth for infected cells (if there are still target cells available for infection once infected cells start dying), and more rapid reduction of infected cell numbers towards the end of infection. Larger δ values are associated with decreased replication fitness. Similar to the τ_V-diff model, to aid presentation relative fitness is quantified using the infected cell productive phase duration (τ_I) rather than death rate (δ); hence *relative fitness* $= \tau_{I,B}/\tau_{I,A}$.

6.5. The k-diff model

As mentioned above in the context of the τ_I-diff hypothesis, NA may be important in determining the lifetime of infected cells. Another way to account for this possible function of NA is to investigate a hypothesis in which only the transition rate from latent to productive infection (k) differs between strains (the "k-diff" model), where *relative fitness* $= k_B/k_A$. Under this hypothesis, a larger estimated k value indicates that the average latent phase duration is shorter so infected cells initiate production of infectious virus more quickly, leading to an increased rate of exponential growth for both infected cells (if there are still target cells available for infection once progeny virus production begins) and infectious virus. Larger k values are associated with increased within-host fitness. This hypothesis is also supported by experimental results indicating that NA is important in the release of progeny virions from the surface of infected cells (see Appendix A).

7. The relative within-host replication fitness of an OR strain isolated during the HNE outbreak

Here we quantify the relative replication fitness of the New17 OR and New163 OS viruses isolated from the HNE outbreak (see Table 1, row 1). We refer to this competitive-mixtures experiment as the natural isolate experiment.

7.1. Fits to data using the *p-diff hypothesis*

Given that virus particle release from infected cells is often considered to be the primary function of NA, we first present our analyses of the p-diff model, in which strain-dependence in the production rate of infectious virus is hypothesised to be the underlying cause of fitness difference. All analyses performed using the p-diff model are identical to those presented in [18]. Figure 2 shows fits of the p-diff model to TCID_{50}, rRT-PCR, and pyrosequencing data from hosts in the natural isolate experiment [18]. Fits of the other four hypothesised models to the natural isolate experiment are shown in Supplementary Figures S2–S5.

Note that the pyrosequencing proportion data in the inocula of the natural isolate experiment are systematically lower than the proportions that were prepared according to TCID_{50} mix (Figure 2, centre column, blue squares at $t = 0$). Also the rRT-PCR:TCID_{50} ratio measured in the inocula (right column, black dots at $t = 0$) increases systematically across the different infection groups with increasing New163 OS inoculum proportions, suggesting that the New163 OS isolate had a larger ratio of *total vRNA*:*infectious virus* compared with the New17 OR isolate. The co-infection model is able to reproduce each of these systematic effects by assuming that the initial *total vRNA*:*infectious virus* ratio in the inoculum ($\rho(0)$) differs by strain, as discussed further in Section 9.

TCID_{50} and rRT-PCR viral load generally decrease over time in the natural isolate experiment, with TCID_{50} reaching undetectable levels by $t \approx$ 6–7 *d (post-infection; p.i.)* (Figure 2, left column). Comparing the two pure-infection groups, there are no substantial differences in TCID_{50} or rRT-PCR viral load dynamics between each group.

In the three mixed-infection groups, there is a general trend for the New17 OR pyrosequencing proportion (Figure 2, centre column) to increase relative to its value in the inoculum (at $t = 0$); i.e. the New17 OR virus tends to outgrow the New163 OS virus within hosts. The slope of this increase also appears to become steeper with greater amounts of New163 OS virus in the inoculum. This trend is reproduced by the best-fit of the p-diff model (Figure 2, solid blue line) but not by most other fits that lie within the 95% confidence level of the LCR (Figure 2, faded dotted blue lines), which rapidly increase and then plateau prior to 24 *h (p.i.)*. Note that this bimodality (i.e. two mechanistically distinct solutions that are each capable of reproducing observed infection dynamics) is a limitation of the p-diff model fitted to the natural isolate experiment, but does not typically occur for the other model-experiment combinations analysed in this work.

7.2. Fits to data using the four alternative hypotheses

Having analysed the natural isolate experiment using the p-diff model, we now analyse fits of the four other hypothesised models to that experiment:

- β-diff (infectivity/mixing rate differs by strain),
- τ_V-diff (lifetime of infectious virions differs by strain),
- τ_I-diff (infected cell productive phase duration differs by strain),
- k-diff (transition rate from latent to productive infection differs by strain).

Fits to infectious viral load, total viral load, and $\rho(0)$ inoculum measurements are similar for all four models (Figures S2–S5, left and right columns). However, fits to pyrosequencing data (Figures S2–S5, centre column) exhibit different behaviours for different models, as does the predicted coupling between infectious and total A:B ratios. The infectious A:B ratio under the τ_I-diff hypothesis (Figure S4, dashed black line) decouples from the total vRNA A:B ratio (solid blue line) after $t \approx$ 2–3 *d (p.i.)*. This decoupling is also present in some of the fits of the τ_V- and k-diff hypotheses (as well as the p-diff hypothesis; Figure 2), but does not occur under the β-diff hypothesis. The fact that predicted infectious proportion dynamics decouple from total vRNA proportion dynamics is crucial, because pyrosequencing assays measure the total vRNA proportion, yet infectious proportion dynamics provide a more direct insight into relative fitness. This highlights the importance of considering both infectious and total virus dynamics in competitive-mixtures experiments.

7.3. Differences in the ability of the five hypothesised models to reproduce observed infection dynamics

All models are able to generate some form of increase in the New17 OR vRNA proportion over time, yet certain models reproduce particular aspects of the pyrosequencing data better than others. The β-diff model is unable to generate the continual increase present in the pyrosequencing data from $t = 0\,d$ *(p.i.)* to $t \approx 6\,d$ *(p.i.)* (Figure S2, centre column). Instead, the New17 OR vRNA proportion rapidly increases and then plateaus within the first 24 *h (p.i.)*, similar to most of the fits generated using the p-diff model (Figure 2, centre column). Both the p- and τ_V-diff models are able to generate fits that reproduce the increase in vRNA proportion between

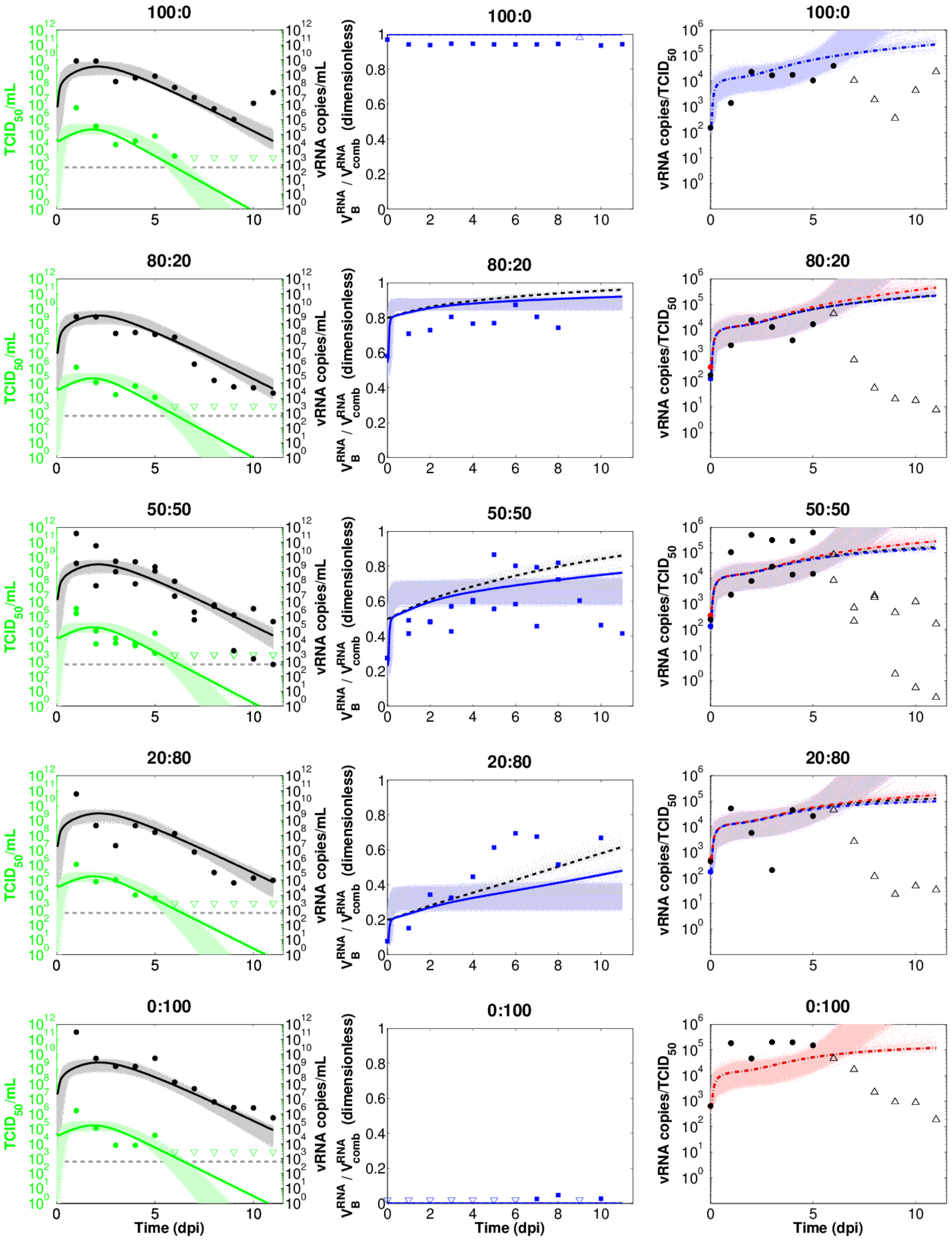

Figure 2: **Fits of the p-diff model to data from the natural isolate experiment.** Each row shows viral load data for a given infection group. The 50:50 mixture was inoculated into two different ferrets in order to provide more data on infections that begin on equal footing; therefore data points may overlap in that group. *Left column:* Best fits are shown of infectious (solid green line; $V_{comb}^{TCID}(t)$) and total (solid black line; $V_{comb}^{RNA}(t)$) viral load to calibrated TCID$_{50}$ data (green dots) and rRT-PCR data (black dots; dashed grey line indicates detection threshold), respectively. *Centre column:* Best fits of the New17 OR vRNA proportion (solid blue line; V_B^{RNA}/V_{comb}^{RNA}) to pyrosequencing data (blue squares). The New17 OR *infectious* proportion is also shown (dashed black line; $V_B^{TCID}/V_{comb}^{TCID}$). *Right column:* Data of the rRT-PCR:TCID$_{50}$ ratio (black dots), together with the total:infectious ratio of both strains combined (dot-dashed black line; $\rho(t) = V_{comb}^{RNA}(t)/V_{comb}^{TCID}(t)$). Note that only the initial condition, $\rho(0)$, is fitted to data. The total:infectious ratio of the New163 OS (dot-dashed red line; red dot indicates initial value) and New17 OR (dot-dashed blue line; blue dot indicates initial value) strains are also shown. In all plots, non-filled arrows indicate that the measured concentration or proportion was outside of the range of detectability for the corresponding assay, with arrow direction indicating the direction of the actual, unknown quantity. In addition to the best fit lines, 5000 randomly sampled fits with SSR values that lie within the 95% confidence level of the LCR are also shown (faded dotted lines).

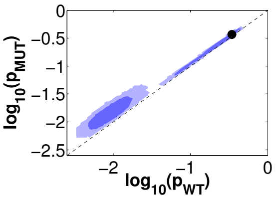

Figure 3: **Correlation between strain-dependent parameters.** The best-fit (black dot) and 2-dimensional projections of the 68% LCR (dark blue contour) and 95% LCR (light blue contour) are shown for the two strain-dependent parameters in the p-diff model, when fitted to the natural isolate dataset. The dashed line shows the line of equivalent fitness. The estimated relative fitness (p_{MUT}/p_{WT}) lies above the line (see Table 3).

$t = 0\,d\,(p.i.)$ and $t \approx 6\,d\,(p.i.)$ (Figures 2 and S3, centre column). However, the vRNA proportion continues to increase beyond $t \approx 6\,d\,(p.i.)$ in those fits, whereas the pyrosequencing data appear to plateau beyond $t \approx 6\,d\,(p.i.)$ and perhaps even decrease following $t \approx 8\,d\,(p.i.)$. The pyrosequencing dynamics in this final stage are, however, difficult to discern due to a relative lack of data following $t \approx 8\,d\,(p.i.)$.

The τ_I- and k-diff models are the most capable of reproducing all of the aforementioned features in the pyrosequencing data (Figures S4 and S5, centre column), and are the best-fitting models overall for the natural isolate experiment. Each model's AIC$_c$ value correlates well with its capacity to reproduce pyrosequencing data (Table 3), simply because model fits differ most prominently when fitting pyrosequencing data. However, these differences in the ability of each hypothesised model to fit data are minor; our results do not provide strong evidence that any particular hypothesised model is more biologically plausible than the others. Table 4, row 1, provides a qualitative comparison of the performance of different models when fitting data from the natural isolate experiment.

7.4. Strain-dependent parameters are highly correlated

Estimates of strain-dependent parameters — e.g. p_{WT} for the OS wild-type strain and p_{MUT} for the OR mutant strain in the p-diff model — have a large degree of uncertainty and overlap. For example, this is evident in estimates of p_{WT} and p_{MUT} obtained when fitting the p-diff model to the natural isolate dataset (see Table 3 and Figure S1 for all p-diff model parameter estimates and LCR projections, respectively).

Despite this uncertainty and overlap, which is present to some degree in all model-fits analysed in this work, each pair of strain-dependent parameters is generally highly correlated to the extent that their *ratio* is well estimated. This is evident in the LCR projection in Figure 3, which shows the correlation of the two strain-dependent parameters in the p-diff model.

7.5. The H275Y mutation does not compromise the within-host replication fitness of the New17 OR virus, regardless of the hypothesised cause of fitness difference

Under each of the p-, β-, τ_V-, and τ_I-diff hypotheses, estimates of relative within-host fitness (Table 3) indicate that the New17 OR virus has significantly greater within-host fitness than the New163 OS virus, although in each case the lower bound of the 95% CI is close to one (equivalent fitness). Under the k-diff hypothesis, although the model fits the data relatively well (comparable AIC$_c$), large uncertainty in the relative fitness estimate leads to a lack of evidence for a fitness difference. These results suggest that the H275Y mutation does not compromise the within-host replication fitness of the New17 OR virus; indeed the New17 OR virus likely has enhanced replication fitness compared with related OS strains.

8. The effects of the V241I and N369K neuraminidase mutations upon the replication fitness of H275Y OR strains

As discussed in Section 2, Butler *et al.* [18] analysed reverse genetics (rg)-derived virus pairs in four additional competitive-mixtures experiments (see Table 1, rows 2–5) to investigate the effect of the V241I and N369K mutations upon the intrinsic fitness of H275Y OR strains.

8.1. Fits to data

When fitting each alternative model to the *rgNew17 OR vs. rgNew17 I241V OR* (Figures S6–S10), *rgNew17 OR vs. rgNew17 K369N OR* (Figures S11–S15), *rgNew17 OR vs. rgNew17 I241V, K369N OR* (Figures S16–S20), and *rgPerth261 V241I, N369K OR vs. rgPerth261 OR* (Figures S21–S25) experiments, fits of infectious viral load, total viral load, and $\rho(0)$ inoculum measurements are reproduced similarly well for all five hypothesised models (Figures S6–S25, left and right columns). For a given hypothesised model, total vRNA A:B ratio dynamics are generally similar for all four reverse genetics experiments (Figures S6–S25, centre column, solid blue lines) and also for the natural isolate experiment (Figures 2 and S2–S5, centre column, solid blue lines). A notable exception to this consistency is evident in fits of the τ_I-diff model, where the increase in total A:B ratio begins at different times for different experiments. This increase occurs latest when fitting the *rgNew17 OR vs. rgNew17 I241V OR* dataset (Figure S9), such that the fitted total A:B ratio is substantially lower than pyrosequencing data in each of the mixed-infection ferrets during $t \lesssim 4\,d\,(p.i.)$. This strong systematic failure indicates that the τ_I-diff model produces a biologically implausible fit to the *rgNew17 OR vs. rgNew17 I241V OR* dataset. We do not interpret relative fitness estimates obtained from that particular experiment–model combination.

8.2. Differences in the ability of the five hypothesised models to reproduce observed infection dynamics

Table 5 also shows the AIC$_c$ values for the five alternative hypothesised models fitted to each of the four reverse genetics experiments. For all four reverse genetics experiments the p-, β-, and k-diff models reproduce infection dynamics most accurately (lowest AIC$_c$ values of the five models; note that AIC$_c$ values are only compared within an experiment (row)). The τ_V- and τ_I-diff models produce relatively poor fits to data. Table 4, rows 2–5, provide a qualitative comparison of model performance when fitting the reverse genetics datasets. The varying ability of each model to reproduce infection dynamics across the different experiments is discussed further in Section 9.

Table 3: **AIC$_c$ values and estimates of fitted parameters and relative replication fitness, for the natural isolate experiment.** Best-fit estimates of relative within-host replication fitness are shown (row 1; 95% CIs in parentheses) together with AIC$_c$ values (row 2) and parameter estimates (rows 3–10), for each model fitted to the natural isolate dataset. Parameters that have separate values for the WT and MUT viruses are shown with the MUT estimate (e.g. $\rho_{MUT}(0)$) below the WT estimate (e.g. $\rho_{WT}(0)$).

	Hypothesised model				
	p-diff	β-diff	τ_V-diff	τ_I-diff	k-diff
RelFit	1.07 (1.02;2.59)	1.56 (1.05;2.92)	1.03 (1.01;1.10)	1.18 (1.06;1.39)	0.07 (0.05;6.06)
AIC$_c$	−719	−713	−717	−732	−728
$log_{10}(V^{TCID}_{comb}(0))$	4.70 (−5.54; 4.70)	4.70 (−6.00; 4.70)	4.70 (−6.00; 4.70)	4.70 (−6.00; 4.70)	4.70 (−0.92; 4.70)
$log_{10}(\rho(0))$	2.66 (2.46; 2.85) 2.13 (1.83; 2.39)	2.66 (2.44; 2.86) 2.14 (1.82; 2.41)	2.66 (2.47; 2.84) 2.14 (1.86; 2.37)	2.66 (2.45; 2.86) 2.13 (1.83; 2.41)	2.66 (2.45; 2.86) 2.14 (1.83; 2.41)
$log_{10}(\beta)$	−5.62 (−5.80; −1.00)	−4.00 (−5.41; −1.04) −3.80 (−5.36; −1.00)	−5.62 (−5.74; −1.00)	−1.03 (−4.50; −1.00)	−1.03 (−3.53; −1.00)
$log_{10}(k)$	1.38 (0.22; 1.38)	1.38 (0.16; 1.38)	1.38 (0.19; 1.38)	1.38 (0.14; 1.38)	1.38 (0.29; 1.38) 0.23 (0.05; 1.38)
$log_{10}(\delta)$	0.90 (−0.61; 0.90)	−0.52 (−0.62; 0.90)	0.90 (−0.60; 0.90)	−0.47 (−0.56; −0.33) −0.54 (−0.62; −0.43)	−0.49 (−0.61; −0.40)
$log_{10}(p)$	−0.46 (−2.49; −0.25) −0.43 (−2.29; −0.22)	(−2.50; −0.58)	−0.45 (−2.35; −0.35)	−1.86 (−2.40; −1.30)	−1.90 (−2.41; −1.35)
$log_{10}(c_h)$	0.21 (0.05; 0.46)	0.20 (0.02; 0.48)	0.31 (0.07; 0.56) 0.27 (−0.01; 0.53)	0.18 (0.01; 0.32)	0.21 (0.06; 0.35)
$log_{10}(\xi)$	3.81 (2.88; 4.54)	3.69 (2.68; 4.62)	3.94 (2.76; 4.54)	3.63 (2.69; 4.53)	3.76 (2.88; 4.61)

Table 4: **Model performance summary.** Qualitative comparison of the performance of each model when fitted to each experimental dataset. The symbols are to be interpreted as follows: **✓✓:** best-fitting model(s) for a given dataset, which capture the trends in data well; **✓:** good-fitting model(s) that capture the majority of trends in data; **?:** marginal model(s) that, while plausible, reproduce some of the trends in data poorly; **×:** poor model(s) that are implausible based on an inability to fit the data. Note that there is no reason to believe that the biological cause of fitness difference should be the same for different experiments.

Dataset	Hypothesised model				
	p-diff	β-diff	τ_V-diff	τ_I-diff	k-diff
New17 OR vs. New163 OS	✓	?	✓	✓✓	✓✓
rgNew17 OR vs. rgNew17 I241V OR	✓✓	✓✓	✓	×	✓✓
rgNew17 OR vs. rgNew17 K369N OR	✓✓	✓	✓	?	✓
rgNew17 OR vs. rgNew17 K369N,I241V OR	✓	✓✓	?	✓	✓✓
rgPerth261 N369K,V241I OR vs. rgPerth261 OR	✓✓	✓✓	?	?	✓✓

Table 5: **Relative replication fitness and AIC$_c$ for the reverse genetics experiments.** Best-fit estimates of relative within-host replication fitness are shown (95% CIs in parentheses) together with AIC$_c$ values, for each model fitted to each of the reverse genetics experiments.

Dataset		Hypothesised model				
		p-diff	β-diff	τ_V-diff	τ_I-diff	k-diff
rgNew17 OR vs. rgNew17 I241V OR	RelFit	3.96 (1.17;6.83)	3.98 (1.12;7.02)	1.79 (1.10;4.58)	–	1.51 (1.08;7.39)
	AIC$_c$	−566	−562	−556	−529	−561
rgNew17 OR vs. rgNew17 K369N OR	RelFit	3.14 (1.17;5.30)	2.44 (1.14;4.79)	2.05 (1.12;3.63)	1.35 (1.15;1.67)	1.94 (1.07;6.91)
	AIC$_c$	−671	−659	−654	−650	−662
rgNew17 OR vs. rgNew17 K369N,I241V OR	RelFit	1.82 (1.35;7.46)	6.33 (1.38;30.92)	1.38 (1.17;2.60)	1.49 (1.28;1.97)	2.97 (1.22;12.77)
	AIC$_c$	−710	−719	−689	−708	−718
rgPerth261 N369K,V241I OR vs. rgPerth261 OR	RelFit	1.86 (1.37;7.24)	5.43 (1.39;15.35)	1.71 (1.23;5.61)	1.31 (1.24;2.18)	1.74 (1.14;9.89)
	AIC$_c$	−769	−776	−693	−690	−775

8.3. The V241I and N369K substitutions improve the *in vivo* replication fitness of H1N1pdm09 H275Y OR viruses, regardless of the hypothesised cause of fitness difference

Table 5 shows estimates of relative within-host replication fitness for each of the five different hypothesised models fitted to the four rg experiments. For each of the three experiments that involve the rgNew17 OR virus, removing either one or both of the V241I and N369K substitutions results in a statistically significant reduction in within-host replication fitness. Conversely, adding the two substitutions to an early H1N1pdm09 virus improves its within-host replication fitness. These results are consistent regardless of the hypothesised biological cause of fitness difference. These relative fitness estimates suggest that the V241I and N369K mutations improve the *in vivo* replication fitness of H1N1pdm09 H275Y OR viruses.

9. Discussion

Results from four of the five hypothesised models indicated that the New17 OR virus has significantly improved replication fitness relative to the New163 OS virus, while there was no evidence for a fitness difference under the *k*-diff hypothesis. If the New17 OR and New163 OS isolates are representative of other viruses from the HNE outbreak, then these results suggest that the H275Y mutation did not compromise the within-host fitness of HNE OR viruses. We come to this conclusion regardless of the hypothesised cause of fitness difference, reinforcing the conclusion presented in our earlier study [18] in which we used the *p*-diff hypothesis.

Our modelling analyses of the rg experiments demonstrates that the V241I and N369K mutations significantly increase the *in vivo* replication fitness of H1N1pdm09 H275Y OR strains. As the V241I and N369K mutations were present in the HNE viruses, this ability to compensate for the fitness cost of the H275Y mutation may have played an important role in enabling those OR viruses to spread amongst the community of the HNE region.

Pinilla *et al.* [17] previously quantified relative fitness *in vitro* by allowing many model parameters to be strain-dependent and directly comparing estimates obtained for each strain. That same technique would not have been suitable for our purposes, as the *in vivo* experiments analysed here involved relatively sparse data and a more complex infection system compared with the *in vitro* experiments analysed by Pinilla *et al.* Instead, we investigated several different hypothesised causes of fitness differences separately, each involving a model with a single strain-dependent biological parameter. The fitting method employed here, while unable to identify some parameters (e.g. $V^{TCID}(0)$ and k, which often have large uncertainties; Figures S1 and S26–S49), was able to consistently generate precise estimates of relative fitness. These robust estimates were possible, despite a large degree of uncertainty and overlap in the strain-dependent parameter estimates, because each parameter pair was found to be highly correlated such that their ratio was well-estimated (e.g. Figure 3), providing a viable method for quantifying relative fitness in competitive-mixtures experiments. These ratios involve comparatively little uncertainty primarily because each model is fitted to pyrosequencing data which, from the inoculum to the end of infection, show one strain consistently outgrowing the other across the different mixed-infection groups (Figures 2 and S2–S25, centre column). Such consistent outgrowth in an experiment can only be reproduced if one strain-dependent parameter is larger than the other; hence their ratio is well-estimated regardless of uncertainty in the actual estimates of each parameter. Fitting this strong trend of outgrowth also tends to generate a consistent picture of which virus is fitter in a given experiment, regardless of the hypothesised biological cause of strain difference.

In the mixed-infection groups, each inoculum was prepared at the desired mixture (i.e. 20:80, 50:50, or 80:20) by measuring the infectivity titre of each virus, and then combining an appropriate amount of each virus together to generate the required proportion [18]. However, for the natural isolate experiment, pyrosequencing measurements of the inocula were systematically lower than the intended proportions (Figure 2). This systematic variation was also present (with a maximum discrepancy of almost 40%) in the *rgNew17 OR vs. rgNew17 K369N OR* (Figure S11) and *rgPerth261 V241I, N369K OR vs. rgPerth261 OR* (Figure S21) experiments. Additionally, measurements of the rRT-PCR:TCID$_{50}$ ratio in the inocula varied systematically across the five different infection groups in each of these three experiments, suggesting that the two competing strains in each experiment had different ratios of infectious and total virus. Under the assumption that the initial *total vRNA*:*infectious virus* ratio ($\rho(0)$) is strain-dependent, the co-infection model is capable of generating not only the systematic variation in rRT-PCR:TCID$_{50}$ ratio but also the systematic discrepancy between intended and measured inoculum proportions. Estimates of $\rho(0)$ were consistent with observed trends in inocula data, in that $\rho(0)$ was significantly different between strains in each of the three experiments where systematic variations were present, whereas no evidence of a significant difference was found in the other two experiments (data not shown). These results reinforce the importance of considering both infectious and total virus when analysing data from competitive-mixtures experiments.

Another possible explanation for the systematic discrepancy between intended and measured inoculum proportions is that the infectivity titres of each virus, taken prior to mixing, were simply inaccurate (e.g. if an A virus infectivity titre measurement had been inaccurate by just 0.1 $TCID_{50}/ml$, then an intended inoculum ratio of 50:50 would actually have led to a 56:44 ratio). This would lead to inoculum proportions that systematically differ from the intended proportions, however it would not explain the systematic change in rRT-PCR:TCID$_{50}$ ratio across different infection groups. Such a hypothesis is not as well supported by the data as the aforementioned hypothesis involving strain-dependence in $\rho(0)$. Nevertheless in future competitive-mixtures experiments it may be useful to more accurately measure the infectious concentration of each virus prior to mixing, e.g. by taking a greater number of replicates of infectivity measurements of each virus in order to reduce uncertainty ($\approx$ 3–5 measurements were performed in the experiments analysed in this work). Such a reduction in uncertainty would allow further scrutiny of the plausibility of the assumption that the initial infectious proportion in each ferret is identical to the intended proportion in the corresponding inoculum.

Previous ferret competitive-mixtures experiments performed by Pinilla *et al.* [17] indicated that an early H1N1pdm09 H275Y OR virus, in which the V241I and N369K mutations were absent, had reduced *in vivo* replication fitness relative to a related OS virus (each of these viruses were generated from the A/Québec/144147/09 isolate using reverse genetics techniques). Our results from the natural isolate competitive-mixtures experiment generally indicated an *in vivo* replication fitness advantage for the OR isolate from the HNE outbreak. If the isolates analysed in [17] and here are representative of similar contemporaneously circulating viruses, then these contrasting results suggest an improvement in the fitness of late H1N1pdm09 OR viruses relative to early H1N1pdm09 OR viruses. This is consistent with the hypothesis that the V241I and N369K mutations enhance the fitness of H1N1pdm09 OR strains.

The *p*-, *β*-, and *k*-diff hypotheses (in which the infectious virus production rate, infectivity/mixing rate, and latent phase duration differ by strain, respectively) are supported not only by experimental results (Section 6) but also by results from previous *in vitro* modelling studies that compared the infection kinetics of H275Y MUT and related WT strains [16, 17]. Pinilla *et al.* [17] found that the production rate of total vRNA from infected cells was statistically significantly different between WT and MUT strains in the H1N1pdm09 background, and that the average duration of the latent phase differed between WT and MUT strains in both the seasonal H1N1 and H1N1pdm09 backgrounds. The infecting time was also found to be different between strains in the seasonal H1N1 background, consistent with the results of Holder *et al.* [16] who performed a different analysis on the same dataset. Note that the infecting time ($\tau_{infect} = \sqrt{2/[p\beta T(0)]}$) is dependent upon both p and β in the co-infection model; thus one or both of the equivalent parameters within the model used by Pinilla *et al.* may have been strain-dependent. The standard deviation in the distribution of latent phase durations (σ_L) was also found by both Pinilla *et al.* [17] and Holder *et al.* [16] to be strain-dependent within the seasonal H1N1 background. Although we did not explicitly estimate σ_L, the estimates by Pinilla *et al.* [17] and Holder *et al.* [16] were roughly correlated with average latent phase duration (τ_L) in both the H1N1pdm09 [17] and seasonal H1N1 [16, 17] backgrounds — the longer the average latent phase, the larger the standard deviation. This behaviour was replicated within the co-infection model, as splitting the L compartment into n_L stages generates an Erlang distribution for latent phase lifetimes with a standard deviation dependent upon the average latent phase duration via $\sigma_L = \tau_L/\sqrt{n_L}$.

For the natural isolate experiment, the *k*-diff model (i.e. latent phase duration differs by strain) and τ_I-diff model (i.e. productive phase duration differs by strain) provided the best fits to data (Figures S4 and S5, and Table 4). For the rg experiments, relatively poor fits were obtained when fitting the τ_V-diff (viral clearance differs by strain) and τ_I-diff models to the *rgPerth261 V241I, N369K OR vs. rgPerth261 OR* dataset, the τ_V-diff model to the *rgNew17 OR vs. rgNew17 I241V, K369N OR* dataset, and the τ_I-diff model to both the *rgNew17 OR vs. rgNew17 I241V OR* and *rgNew17 OR vs. rgNew17 K369N OR* datasets (Tables 4 and 5). It is interesting that the τ_I-diff model produced the best fit to the natural isolate experiment, yet repeatedly produced poor fits to the rg experiments. Indeed biological differences between strains in the natural isolate experiment may be distinct from those in the rg experiments, as all virus pairs used in the rg experiments differ only via NA substitutions, whereas the viruses used in the natural isolate experiment differ via substitutions in both the NA gene and other genes. We have previously noted that none of the extra amino acid differences between the natural isolates have been linked to any functional process [18]. Nonetheless it is possible that one or more of those substitutions have some yet to be established functional effect. This analysis highlights the potential to examine which hypothesised causes of fitness differences are the most plausible given observed competitive-mixtures data. Yet it is crucial to caution against overinterpretation of our results, as the co-infection model (1) involves relatively simple dynamics when compared with the complexities of the influenza infection system [21, 20, 63]; and (2) is fitted to data that give only partial insight into those complex dynamics. More realistic within-host models coupled with more comprehensive datasets will be required to improve confidence in model selection.

Previous *in vitro* modelling of H275Y OR and related OS strains in the H1N1pdm09 background indicated that the ratio of *total vRNA*:*infectious virus* produced by infected cells significantly differed by strain [17]. A hypothesis in which the ratio of *total vRNA*:*infectious virus* produced by infected cells (ξ) is assumed to differ by strain could potentially generate strain-dependent viral load dynamics *without* an associated fitness difference, because only *non*-infectious virus production would differ by strain. We did not investigate such a model in this work because, in each competitive-mixtures experiment, observed outgrowth in pyrosequencing data across serial host-to-host transmission lines suggested that the fitness of each virus pair was indeed different [18]. For future competitive-mixtures studies in which outgrowth is *not* evident in mixture data, or in which multiple different hypotheses regarding functional differences between strains are investigated simultaneously, this alternative hypothesis may be a relevant biologically plausible scenario to investigate.

It is possible for predicted infectious A:B ratio dynamics to decouple from total vRNA ratio dynamics (e.g. Figure S4, centre column). As infectious ratio dynamics provide more direct insight into relative fitness compared with total vRNA ratio dynamics, future development of an assay capable of measuring the infectious ratio would likely improve the capacity of competitive-mixtures experiments to assess relative fitness.

Furthermore, predicted infectious ratio dynamics sometimes differ substantially between different hypothesised models (e.g. compare the dashed black lines in the centre column of Figure S2 to those of Figure S4). These markedly different infectious ratios could lead to very different predictions regarding the proportion of each strain that is transmitted during any given transmission event. Such model-dependent behaviour can be explored in greater detail if transmission dynamics are incorporated into the co-infection model, and such an extended model is currently under development.

We have detailed a method for quantifying the relative within-host replication fitness of two competing influenza strains in competitive-mixtures experiments. Our results have relevance for drug-resistant influenza surveillance, and were consistent regardless of which underlying mechanism was assumed to generate a fitness difference between strains. The method may also have relevance for acute infections other than influenza, particularly those where drug-resistant or highly pathogenic strains have the potential to out-compete established strains.

10. Acknowledgements

We thank Mathew Dafilis for his assistance with the implementation of an optimised ODE solver using the CVode package for MATLAB. We acknowledge use of computing resources from the NeCTAR research cloud (`http://www.nectar.org.au`). NeCTAR is an Australian Government project conducted as part of the Super Science initiative and financed by the Education Investment Fund. This research was supported by a Victorian Life Sciences Computation Initiative (VLSCI) grant (VR0274) on its Peak Computing Facility at the University of Melbourne, an initiative of the Victorian Government, Australia. We also acknowledge use of computing resources from the High Performance Computing Cluster at the University of Melbourne. The Melbourne WHO Collaborating Centre for Reference and Research on Influenza at the Peter Doherty Institute for Infection and Immunity is supported by the Australian Government Department of Health. Jodie McVernon was supported by a National Health and Medical Research Council Career Development Award (1061321). James McCaw was supported by an Australian Research Council Future Fellowship (110100250).

Appendix A. Known functions of the NA surface protein

NA is important in facilitating the release of virus particles via cleavage of sialic acid residues, following the budding of those particles on the surface of infected cells (for related reviews, see [41, 42, 43, 44, 45, 46]). Similarly, recent *in vitro* experiments have indicated that NA is capable of counteracting the effects of the antiviral factor tetherin, which also facilitates the release of progeny virions [47]. Other recent work has indicated that NA may be important in the budding of viral particles on the surface of infected cells and in the resulting morphogenesis of those particles [48, 49, 47], and that the presence of NA alone within cells can lead to the release of non-infectious viral particles [48]. Taken together, these known functions of NA indicate that it is important in the process of virion production, and in regulating the balance between production of infectious and non-infectious virions.

Previous results have indicated that NA may be important in reducing the inhibiting effects of decoy receptors in mucins [42, 50, 51, 52, 53, 54], thus counteracting the effect of mucins in restricting the spatial spread of free virions throughout the site of infection. This function of NA may also inhibit host-driven clearance of virions from the site of infection, as decoy receptors in mucins, upon binding to free virions, also promote the clearance of those virions [55, 56].

Some studies have indicated that NA is important for influenza virus entry into susceptible cells [57, 58, 59]. NA may also be important in determining the lifetime of infected cells [60, 61].

The results of Huang *et al.* [62] suggest that NA also plays a role in inhibiting super-infection (i.e. the infection of a host cell by multiple influenza virions). However, we do not investigate strain-dependence in this process as a possible biological hypothesis for the source of fitness difference in this work, because a core assumption of the co-infection model was that susceptible cells are infected by a *single* infectious virion.

References

[1] K. G. Nicholson, J. M. Wood, M. Zambon, Influenza., Lancet 362 (9397) (2003) 1733–45. doi:10.1016/S0140-6736(03)14854-4.
URL http://www.ncbi.nlm.nih.gov/pubmed/19799843

[2] S. J. Sullivan, R. M. Jacobson, W. R. Dowdle, G. A. Poland, 2009 H1N1 influenza., Mayo Clinic Proceedings. Mayo Clinic 85 (1) (2010) 64–76. doi:10.4065/mcp.2009.0588.
URL http://www.ncbi.nlm.nih.gov/pubmed/20007905

[3] U. Grienke, M. Schmidtke, S. von Grafenstein, J. Kirchmair, K. R. Liedl, J. M. Rollinger, Influenza neuraminidase: a druggable target for natural products., Natural Product Reports 29 (1) (2012) 11–36. doi:10.1039/c1np00053e.
URL http://www.ncbi.nlm.nih.gov/pubmed/22025274

[4] A. Kelso, A. C. Hurt, Drug-resistant influenza viruses: why fitness matters, Nature Medicine 18 (10) (2012) 1470–1472.

[5] T. G. Sheu, V. M. Deyde, M. Okomo-Adhiambo, R. J. Garten, X. Xu, R. a. Bright, E. N. Butler, T. R. Wallis, A. I. Klimov, L. V. Gubareva, Surveillance for neuraminidase inhibitor resistance among human influenza A and B viruses circulating worldwide from 2004 to 2008, Antimicrobial Agents and Chemotherapy 52 (9) (2008) 3284–92. doi:10.1128/AAC.00555-08.
URL http://www.pubmedcentral.nih.gov/articlerender.fcgi?artid=2533500&tool=pmcentrez&rendertype=abstract

[6] Centers for Disease Control and Prevention (CDC), Update: Influenza Activity United States, September 30, 2007April 5, 2008, and Composition of the 200809 Influenza Vaccine, MMWR. Morbidity and Mortality Weekly Report 57 (15) (2008) 404–409.

[7] S. H. Hauge, S. Dudman, K. Borgen, A. Lackenby, O. Hungnes, Oseltamivir-Resistant Influenza Viruses A (H1N1), Norway, 2007-08, Emerging Infectious Diseases 15 (2) (2009) 155–162. doi:10.3201/eid1502.081031.
URL http://www.cdc.gov/eid/content/15/2/155.htm

[8] A. Meijer, A. Lackenby, O. Hungnes, B. Lina, S. van der Werf, B. Schweiger, M. Opp, J. Paget, J. van der Kassteele, A. Hay, M. Zambon, Oseltamivir-Resistant Influenza Virus A (H1N1), Europe, 2007-08 Season, Emerging Infectious Diseases 15 (4) (2009) 552–560. doi:10.3201/eid1504.081280.
URL http://www.cdc.gov/eid/content/15/4/552.htm

[9] Centers for Disease Control and Prevention (CDC), Update: influenza activity–United States, September 28, 2008-April 4, 2009, and composition of the 2009-10 influenza vaccine., MMWR. Morbidity and Mortality Weekly Report 58 (14) (2009) 369–74.
URL http://www.ncbi.nlm.nih.gov/pubmed/21918493

[10] N. J. Dharan, L. V. Gubareva, J. J. Meyer, M. Okomo-Adhiambo, R. C. McClinton, S. A. Marshall, K. St George, S. Epperson, L. Brammer, A. I. Klimov, J. S. Bresee, A. M. Fry, Infections with oseltamivir-resistant influenza A(H1N1) virus in the United States., JAMA : the Journal of the American Medical Association 301 (10) (2009) 1034–41. doi:10.1001/jama.2009.294.
URL http://www.ncbi.nlm.nih.gov/pubmed/21737049

[11] A. C. Hurt, J. Ernest, Y.-M. Deng, P. Iannello, T. G. Besselaar, C. Birch, P. Buchy, M. Chittaganpitch, S.-C. Chiu, D. Dwyer, A. Guigon, B. Harrower, I. P. Kei, T. Kok, C. Lin, K. McPhie, A. Mohd, R. Olveda, T. Panayotou, W. Rawlinson, L. Scott, D. Smith, H. D'Souza, N. Komadina, R. Shaw, A. Kelso, I. G. Barr, Emergence and spread of oseltamivir-resistant A(H1N1) influenza viruses in Oceania, South East Asia and South Africa., Antiviral Research 83 (1) (2009) 90–3. doi:10.1016/j.antiviral.2009.03.003.
URL http://www.ncbi.nlm.nih.gov/pubmed/19501261

[12] A. Moscona, Global transmission of oseltamivir-resistant influenza., The New England Journal of Medicine 360 (10) (2009) 953–6. doi:10.1056/NEJMp0900648.
URL http://www.pubmedcentral.nih.gov/articlerender.fcgi?artid=3089626&tool=pmcentrez&rendertype=abstract

[13] A. F. M. Marée, W. Keulen, C. A. B. Boucher, R. J. De Boer, Estimating relative fitness in viral competition experiments., Journal of Virology 74 (23) (2000) 11067–72.
URL http://www.pubmedcentral.nih.gov/articlerender.fcgi?artid=113186&tool=pmcentrez&rendertype=abstract

[14] H. Wu, Y. Huang, C. Dykes, D. Liu, J. Ma, A. S. Perelson, L. M. Demeter, Modeling and estimation of replication fitness of human immunodeficiency virus type 1 in vitro experiments by using a growth competition assay, Journal of Virology 80 (5) (2006) 2380–2389. doi:10.1128/JVI.80.5.2380.
URL http://jvi.asm.org/cgi/content/abstract/80/5/2380

[15] A. C. Hurt, S. S. Nor'e, J. M. McCaw, H. R. Fryer, J. Mosse, A. R. McLean, I. G. Barr, Assessing the viral fitness of oseltamivir-resistant influenza viruses in ferrets, using a competitive-mixtures model., Journal of Virology 84 (18) (2010) 9427–38. doi:10.1128/JVI.00373-10.
URL http://www.pubmedcentral.nih.gov/articlerender.fcgi?artid=2937593&tool=pmcentrez&rendertype=abstract

[16] B. P. Holder, P. Simon, L. E. Liao, Y. Abed, X. Bouhy, C. A. A. Beauchemin, G. Boivin, Assessing the in vitro fitness of an oseltamivir-resistant seasonal A/H1N1 influenza strain using a mathematical model., PloS ONE 6 (3) (2011) e14767. doi:10.1371/journal.pone.0014767.
URL http://www.pubmedcentral.nih.gov/articlerender.fcgi?artid=3063785&tool=pmcentrez&rendertype=abstract

[17] L. T. Pinilla, B. P. Holder, Y. Abed, G. Boivin, C. A. A. Beauchemin, The H275Y Neuraminidase Mutation of the Pandemic A/H1N1 Influenza Virus Lengthens the Eclipse Phase and Reduces Viral Output of Infected Cells, Potentially Compromising Fitness in Ferrets., Journal of Virology 86 (19) (2012) 10651–60. doi:10.1128/JVI.07244-11.
URL http://www.ncbi.nlm.nih.gov/pubmed/22837199

[18] J. Butler, K. A. Hooper, S. Petrie, R. Lee, S. Maurer-Stroh, L. Reh, T. Guarnaccia, C. Baas, L. Xue, S. Vitesnik, S.-K. Leang, J. McVernon, A. Kelso, I. G. Barr, J. M. McCaw, J. D. Bloom, A. C. Hurt, Estimating the Fitness Advantage Conferred by Permissive Neuraminidase Mutations in Recent Oseltamivir-Resistant A(H1N1)pdm09 Influenza Viruses, PLoS Pathogens 10 (4) (2014) e1004065. doi:10.1371/journal.ppat.1004065.
URL http://dx.plos.org/10.1371/journal.ppat.1004065

[19] S. M. Petrie, T. Guarnaccia, K. L. Laurie, A. C. Hurt, J. McVernon, J. M. McCaw, Reducing uncertainty in within-host parameter estimates of influenza infection by measuring both infectious and total viral load., PloS ONE 8 (5) (2013) e64098. doi:10.1371/journal.pone.0064098.
URL http://www.pubmedcentral.nih.gov/articlerender.fcgi?artid=3655064&tool=pmcentrez&rendertype=abstract

[20] A. M. Smith, A. S. Perelson, Influenza A virus infection kinetics: quantitative data and models, Wiley Interdisciplinary Reviews: Systems Biology and Medicine 3 (4) (2011) 429–445. doi:10.1002/wsbm.129.
URL http://onlinelibrary.wiley.com/doi/10.1002/wsbm.129/abstract

[21] C. A. A. Beauchemin, A. Handel, A review of mathematical models of influenza A infections within a host or cell culture: lessons learned and challenges ahead., BMC Public Health 11 Suppl 1 (Suppl 1) (2011) S7. doi:10.1186/1471-2458-11-S1-S7.
URL http://www.ncbi.nlm.nih.gov/pubmed/21356136

[22] L. Möhler, D. Flockerzi, H. Sann, U. Reichl, Mathematical model of influenza A virus production in large-scale microcarrier culture., Biotechnology and Bioengineering 90 (1) (2005) 46–58. doi:10.1002/bit.20363.
URL http://www.ncbi.nlm.nih.gov/pubmed/15736163

[23] P. Baccam, C. A. A. Beauchemin, C. A. Macken, F. G. Hayden, A. S. Perelson, Kinetics of influenza A virus infection in humans., Journal of Virology 80 (15) (2006) 7590–9. doi:10.1128/JVI.01623-05.
URL http://www.ncbi.nlm.nih.gov/pubmed/16840338

[24] A. Handel, I. M. Longini, R. Antia, Neuraminidase inhibitor resistance in influenza: assessing the danger of its generation and spread., PLoS Computational Biology 3 (12) (2007) e240. doi:10.1371/journal.pcbi.0030240.
URL http://www.pubmedcentral.nih.gov/articlerender.fcgi?artid=2134965&tool=pmcentrez&rendertype=abstract

[25] C. A. A. Beauchemin, J. J. McSharry, G. L. Drusano, J. T. Nguyen, G. T. Went, R. M. Ribeiro, A. S. Perelson, Modeling amantadine treatment of influenza A virus in vitro., Journal of Theoretical Biology 254 (2) (2008) 439–51. doi:10.1016/j.jtbi.2008.05.031.
URL http://www.pubmedcentral.nih.gov/articlerender.fcgi?artid=2663526&tool=pmcentrez&rendertype=abstract

[26] J. Schulze-Horsel, M. Schulze, G. Agalaridis, Y. Genzel, U. Reichl, Infection dynamics and virus-induced apoptosis in cell culture-based influenza vaccine production-Flow cytometry and mathematical modeling., Vaccine

27 (20) (2009) 2712–22. doi:10.1016/j.vaccine.2009.02.027.
URL http://www.ncbi.nlm.nih.gov/pubmed/19428884

[27] H. Miao, J. A. Hollenbaugh, M. S. Zand, J. Holden-Wiltse, T. R. Mosmann, A. S. Perelson, H. Wu, D. J. Topham, Quantifying the early immune response and adaptive immune response kinetics in mice infected with influenza A virus., Journal of Virology 84 (13) (2010) 6687–98. doi:10.1128/JVI.00266-10.
URL http://www.pubmedcentral.nih.gov/articlerender.fcgi?artid=2903284&tool=pmcentrez&rendertype=abstract

[28] R. A. Saenz, M. Quinlivan, D. Elton, S. Macrae, A. S. Blunden, J. A. Mumford, J. M. Daly, P. Digard, A. Cullinane, B. T. Grenfell, J. W. McCauley, J. L. N. Wood, J. R. Gog, Dynamics of influenza virus infection and pathology., Journal of Virology 84 (8) (2010) 3974–83. doi:10.1128/JVI.02078-09.
URL http://www.ncbi.nlm.nih.gov/pubmed/20130053

[29] B. P. Holder, C. A. A. Beauchemin, Exploring the effect of biological delays in kinetic models of influenza within a host or cell culture., BMC Public Health 11 Suppl 1 (Suppl 1) (2011) S10. doi:10.1186/1471-2458-11-S1-S10.
URL http://www.ncbi.nlm.nih.gov/pubmed/21356129

[30] A. M. Smith, F. R. Adler, J. L. McAuley, R. N. Gutenkunst, R. M. Ribeiro, J. A. McCullers, A. S. Perelson, Effect of 1918 PB1-F2 Expression on Influenza A Virus Infection Kinetics, PLoS Computational Biology 7 (2) (2011) e1001081. doi:10.1371/journal.pcbi.1001081.
URL http://dx.plos.org/10.1371/journal.pcbi.1001081

[31] K. A. Pawelek, G. T. Huynh, M. Quinlivan, A. Cullinane, L. Rong, A. S. Perelson, Modeling within-host dynamics of influenza virus infection including immune responses., PLoS Computational Biology 8 (6) (2012) e1002588. doi:10.1371/journal.pcbi.1002588.
URL http://www.pubmedcentral.nih.gov/articlerender.fcgi?artid=3386161&tool=pmcentrez&rendertype=abstract

[32] U. Arndt, G. Wennemuth, P. Barth, M. Nain, Y. Al-Abed, A. Meinhardt, D. Gemsa, M. Bacher, Release of macrophage migration inhibitory factor and CXCL8/interleukin-8 from lung epithelial cells rendered necrotic by influenza A virus infection, Journal of Virology 76 (18) (2002) 9298. doi:10.1128/JVI.76.18.9298.
URL http://jvi.asm.org/cgi/content/abstract/76/18/9298

[33] O. Zhirnov, H.-D. Klenk, Human influenza A viruses are proteolytically activated and do not induce apoptosis in CACO-2 cells, Virology 313 (1) (2003) 198–212. doi:10.1016/S0042-6822(03)00264-2.
URL http://linkinghub.elsevier.com/retrieve/pii/S0042682203002642

[34] F. L. Horsfall, On the reproduction of influenza virus. Quantitative studies with procedures which enumerate infective and hemagglutinating virus particles, The Journal of Experimental Medicine 100 (2) (1954) 135–161.
URL http://www.ncbi.nlm.nih.gov/pmc/articles/PMC2136364/

[35] K. Paucker, W. Henle, Studies on host-virus interactions in the chick embryo-influenza virus system. XI. The effect of partial inactivation of standard seed virus at 37C upon the progeny, The Journal of Experimental Medicine 101 (5) (1955) 479–492.
URL http://jem.rupress.org/content/90/1/23.abstract

[36] C. R. Gaush, T. F. Smith, Replication and plaque assay of influenza virus in an established line of canine kidney cells., Applied Microbiology 16 (4) (1968) 588–94.
URL http://www.pubmedcentral.nih.gov/articlerender.fcgi?artid=547475&tool=pmcentrez&rendertype=abstract

[37] F. W. Orthel, Influenza virus titrations and the inhibitor of hemagglutination in normal allantoic fluid., Archiv für die gesamte Virusforschung 38 (4) (1972) 347–56.
URL http://www.ncbi.nlm.nih.gov/pubmed/5083408

[38] M. Schwaab, E. Biscaiajr, J. Monteiro, J. Pinto, Nonlinear parameter estimation through particle swarm optimization, Chemical Engineering Science 63 (6) (2008) 1542–1552. doi:10.1016/j.ces.2007.11.024.
URL http://linkinghub.elsevier.com/retrieve/pii/S0009250907008755

[39] J. Donaldson, R. Schnabel, Computational experience with confidence regions and confidence intervals for nonlinear least squares, Technometrics 29 (1) (1987) 67–82.
URL http://www.jstor.org/stable/10.2307/1269884

[40] K. P. Burnham, D. R. Anderson, Multimodel Inference: Understanding AIC and BIC in Model Selection, Sociological Methods & Research 33 (2) (2004) 261–304. doi:10.1177/0049124104268644.
URL http://smr.sagepub.com/cgi/doi/10.1177/0049124104268644

[41] P. M. Colman, Influenza virus neuraminidase: structure, antibodies, and inhibitors., Protein Science 3 (10) (1994) 1687–96. doi:10.1002/pro.5560031007.
URL http://www.pubmedcentral.nih.gov/articlerender.fcgi?artid=2142611&tool=pmcentrez&rendertype=abstract

[42] L. V. Gubareva, L. Kaiser, F. G. Hayden, Influenza virus neuraminidase inhibitors, The Lancet 355 (2000) 827–835.
URL http://www.sciencedirect.com/science/article/pii/S0140673699114338

[43] R. Wagner, M. Matrosovich, H.-D. Klenk, Functional balance between haemagglutinin and neuraminidase in influenza virus infections., Reviews in Medical Virology 12 (3) (2002) 159–66. doi:10.1002/rmv.352.
URL http://www.ncbi.nlm.nih.gov/pubmed/11987141

[44] D. P. Nayak, E. K.-W. Hui, S. Barman, Assembly and budding of influenza virus., Virus Research 106 (2) (2004) 147–65. doi:10.1016/j.virusres.2004.08.012.
URL http://www.ncbi.nlm.nih.gov/pubmed/15567494

[45] J. Gong, W. Xu, J. Zhang, Structure and functions of influenza virus neuraminidase., Current Medicinal Chemistry 14 (1) (2007) 113–22.
URL http://www.ncbi.nlm.nih.gov/pubmed/17266572

[46] J. S. Rossman, R. a. Lamb, Influenza virus assembly and budding., Virology 411 (2) (2011) 229–36. doi:10.1016/j.virol.2010.12.003.
URL http://www.pubmedcentral.nih.gov/articlerender.fcgi?artid=3086653&tool=pmcentrez&rendertype=abstract

[47] M. a. Yondola, F. Fernandes, A. Belicha-Villanueva, M. Uccelini, Q. Gao, C. Carter, P. Palese, Budding capability of the influenza virus neuraminidase can be modulated by tetherin., Journal of Virology 85 (6) (2011) 2480–91. doi:10.1128/JVI.02188-10.
URL http://www.pubmedcentral.nih.gov/articlerender.fcgi?artid=3067929&tool=pmcentrez&rendertype=abstract

[48] J. C. C. Lai, W. W. L. Chan, F. Kien, J. M. Nicholls, J. S. M. Peiris, J.-M. Garcia, Formation of virus-like particles from human cell lines exclusively expressing influenza neuraminidase., The Journal of General Virology 91 (Pt 9) (2010) 2322–30. doi:10.1099/vir.0.019935-0.
URL http://www.ncbi.nlm.nih.gov/pubmed/20505010

[49] H. Ushirogawa, M. Ohuchi, Novel antiviral activity of neuraminidase inhibitors against an avian influenza A virus., Virology Journal 8 (2011) 411. doi:10.1186/1743-422X-8-411.
URL http://www.pubmedcentral.nih.gov/articlerender.fcgi?artid=3170304&tool=pmcentrez&rendertype=abstract

[50] M. N. Matrosovich, T. Y. Matrosovich, T. Gray, N. A. Roberts, H.-D. Klenk, Neuraminidase Is Important for the Initiation of Influenza Virus Infection in Human Airway Epithelium, Journal of Virology 78 (22) (2004) 12665–12667. doi:10.1128/JVI.78.22.12665.

[51] E. de Vries, R. P. de Vries, M. J. Wienholts, C. E. Floris, M.-S. Jacobs, A. van den Heuvel, P. J. M. Rottier, C. a. M. de Haan, Influenza A virus entry into cells lacking sialylated N-glycans., Proceedings of the National Academy of Sciences of the United States of America 109 (19) (2012) 7457–62. doi:10.1073/pnas.1200987109.
URL http://www.pubmedcentral.nih.gov/articlerender.fcgi?artid=3358892&tool=pmcentrez&rendertype=abstract

[52] T. Gerlach, L. Kühling, J. Uhlendorff, V. Laukemper, T. Matrosovich, V. Czudai-Matwich, F. Schwalm, H.-D. Klenk, M. Matrosovich, Characterization of the neuraminidase of the H1N1/09 pandemic influenza virus., Vaccine 30 (51) (2012) 7348–52. doi:10.1016/j.vaccine.2012.09.078.
URL http://www.ncbi.nlm.nih.gov/pubmed/23063828

[53] T. Nishikawa, K. Shimizu, T. Tanaka, K. Kuroda, T. Takayama, T. Yamamoto, N. Hanada, Y. Hamada, Bacterial neuraminidase rescues influenza virus replication from inhibition by a neuraminidase inhibitor., PloS ONE 7 (9) (2012) e45371. doi:10.1371/journal.pone.0045371.
URL http://www.pubmedcentral.nih.gov/articlerender.fcgi?artid=3445474&tool=pmcentrez&rendertype=abstract

[54] D. D. Y. Wong, K.-T. Choy, R. W. Y. Chan, S. F. Sia, H.-P. Chiu, P. P. H. Cheung, M. C. W. Chan, J. S. M. Peiris, H.-L. Yen, Com-

parable fitness and transmissibility between oseltamivir-resistant pandemic 2009 and seasonal H1N1 influenza viruses with the H275Y neuraminidase mutation., Journal of Virology 86 (19) (2012) 10558–70. `doi:10.1128/JVI.00985-12`.
URL `http://www.ncbi.nlm.nih.gov/pubmed/22811535`

[55] C. L. Hattrup, S. J. Gendler, Structure and function of the cell surface (tethered) mucins, Annual Review of Physiology 70 (2008) 431–57. `doi:10.1146/annurev.physiol.70.113006.100659`.
URL `http://www.ncbi.nlm.nih.gov/pubmed/17850209`

[56] D. J. Thornton, K. Rousseau, M. A. McGuckin, Structure and function of the polymeric mucins in airways mucus., Annual Review of Physiology 70 (2008) 459–86. `doi:10.1146/annurev.physiol.70.113006.100702`.
URL `http://www.ncbi.nlm.nih.gov/pubmed/17850213`

[57] T. Suzuki, T. Takahashi, C.-T. Guo, K. I.-P. J. Hidari, D. Miyamoto, H. Goto, Y. Kawaoka, Y. Suzuki, Sialidase activity of influenza A virus in an endocytic pathway enhances viral replication, Journal of Virology 79 (18) (2005) 11705–15. `doi:10.1128/JVI.79.18.11705`.
URL `http://jvi.asm.org/content/79/18/11705.short`

[58] B. Su, S. Wurtzer, M.-A. Rameix-Welti, D. E. Dwyer, S. van der Werf, N. Naffakh, F. Clavel, B. Labrosse, Enhancement of the influenza A hemagglutinin (HA)-mediated cell-cell fusion and virus entry by the viral neuraminidase (NA)., PloS ONE 4 (12) (2009) e8495. `doi:10.1371/journal.pone.0008495`.
URL `http://www.ncbi.nlm.nih.gov/pubmed/20041119`

[59] X. Zhu, R. McBride, C. M. Nycholat, W. Yu, J. C. Paulson, I. a. Wilson, Influenza virus neuraminidases with reduced enzymatic activity that avidly bind sialic acid receptors., Journal of Virology 86 (24) (2012) 13371–83. `doi:10.1128/JVI.01426-12`.
URL `http://www.ncbi.nlm.nih.gov/pubmed/23015718`

[60] S. J. Morris, G. E. Price, J. M. Barnett, S. A. Hiscox, H. Smith, C. Sweet, Role of neuraminidase in influenza virus-induced apoptosis, Journal of General Virology 80 (1) (1999) 137–146.
URL `http://vir.sgmjournals.org/content/80/1/137.short`

[61] P. Gaur, P. Ranjan, S. Sharma, J. R. Patel, J. B. Bowzard, S. K. Rahman, R. Kumari, S. Gangappa, J. M. Katz, N. J. Cox, R. B. Lal, S. Sambhara, S. K. Lal, Influenza A virus neuraminidase protein enhances cell survival through interaction with carcinoembryonic antigen-related cell adhesion molecule 6 (CEACAM6) protein., The Journal of Biological Chemistry 287 (18) (2012) 15109–17. `doi:10.1074/jbc.M111.328070`.
URL `http://www.pubmedcentral.nih.gov/articlerender.fcgi?artid=3340274&tool=pmcentrez&rendertype=abstract`

[62] I.-C. Huang, W. Li, J. Sui, W. Marasco, H. Choe, M. Farzan, Influenza A virus neuraminidase limits viral superinfection., Journal of Virology 82 (10) (2008) 4834–43. `doi:10.1128/JVI.00079-08`.
URL `http://www.pubmedcentral.nih.gov/articlerender.fcgi?artid=2346733&tool=pmcentrez&rendertype=abstract`

[63] H. M. Dobrovolny, M. B. Reddy, M. A. Kamal, C. R. Rayner, C. A. A. Beauchemin, Assessing Mathematical Models of Influenza Infections Using Features of the Immune Response, PLoS ONE 8 (2) (2013) e57088. `doi:10.1371/journal.pone.0057088`.
URL `http://dx.plos.org/10.1371/journal.pone.0057088`

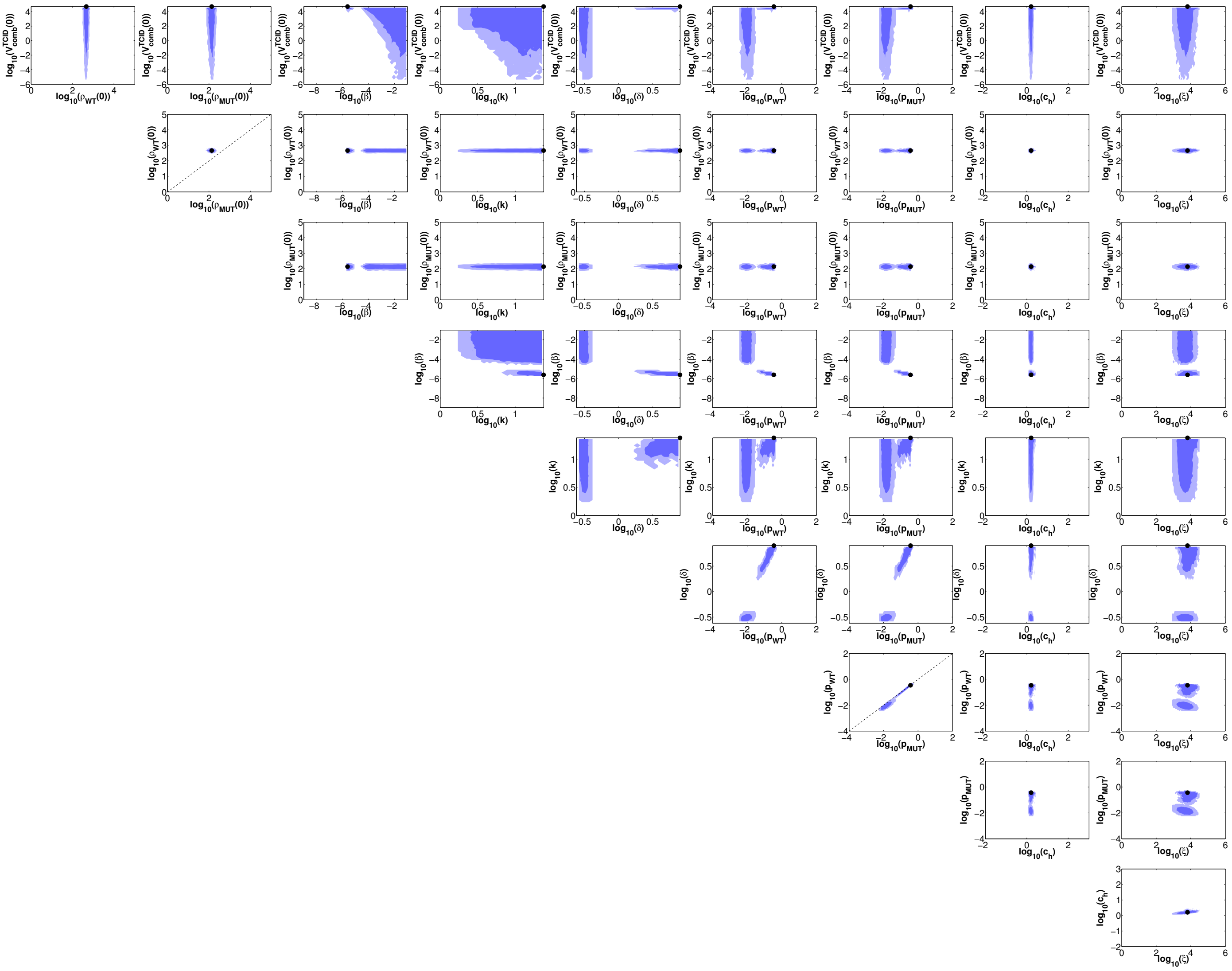

Figure S1: **LCR projections for the p-diff model fitted to the natural isolate dataset.** Best-fits (black dots) and 2-dimensional projections of the 68% LCR (dark blue contours) and 95% LCR (light blue contours) are shown for each model parameter, for the p-diff model fitted to data from the natural isolate experiment. Dashed lines show $\rho_{WT}(0) = \rho_{MUT}(0)$ and $p_{WT} = p_{MUT}$. All axis bounds correspond to the biologically realistic ranges imposed during fitting (see Table 2).

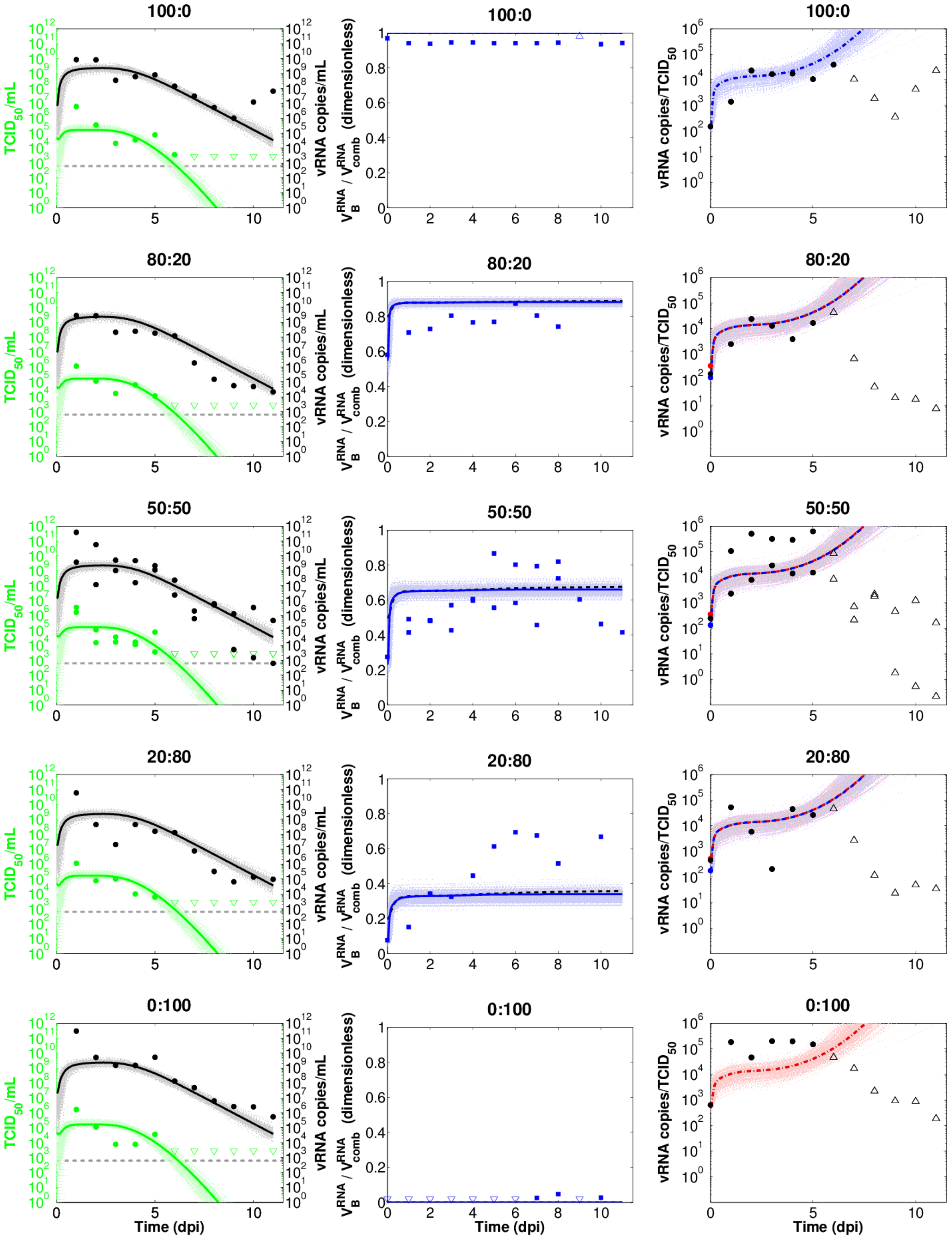

Figure S2: **Fits of the β-diff model to data from the natural isolate experiment.** Each row shows viral load data for a given infection group. The 50:50 mixture was inoculated into two different ferrets in order to provide more data on infections that begin on equal footing; therefore data points may overlap in that group. *Left column:* Best fits are shown of infectious (solid green line; $V^{TCID}_{comb}(t)$) and total (solid black line; $V^{RNA}_{comb}(t)$) viral load to calibrated TCID$_{50}$ data (green dots) and rRT-PCR data (black dots; dashed grey line indicates detection threshold), respectively. *Centre column:* Best fits of the New17 OR vRNA proportion (solid blue line; $V^{RNA}_{B}/V^{RNA}_{comb}$) to pyrosequencing data (blue squares). The New17 OR *infectious* proportion is also shown (dashed black line; $V^{TCID}_{B}/V^{TCID}_{comb}$). *Right column:* Data of the rRT-PCR:TCID$_{50}$ ratio (black dots), together with the total:infectious ratio of both strains combined (dot-dashed black line; $\rho(t) = V^{RNA}_{comb}(t)/V^{TCID}_{comb}(t)$). Note that only the initial condition, $\rho(0)$, is fitted to data. The total:infectious ratio of the New163 OS (dot-dashed red line; red dot indicates initial value) and New17 OR (dot-dashed blue line; blue dot indicates initial value) strains are also shown. In all plots, non-filled arrows indicate that the measured concentration or proportion was outside of the range of detectability for the corresponding assay, with arrow direction indicating the direction of the actual, unknown quantity. In addition to the best fit lines, 5000 randomly sampled fits with SSR values that lie within the 95% confidence level of the LCR are also shown (faded dotted lines).

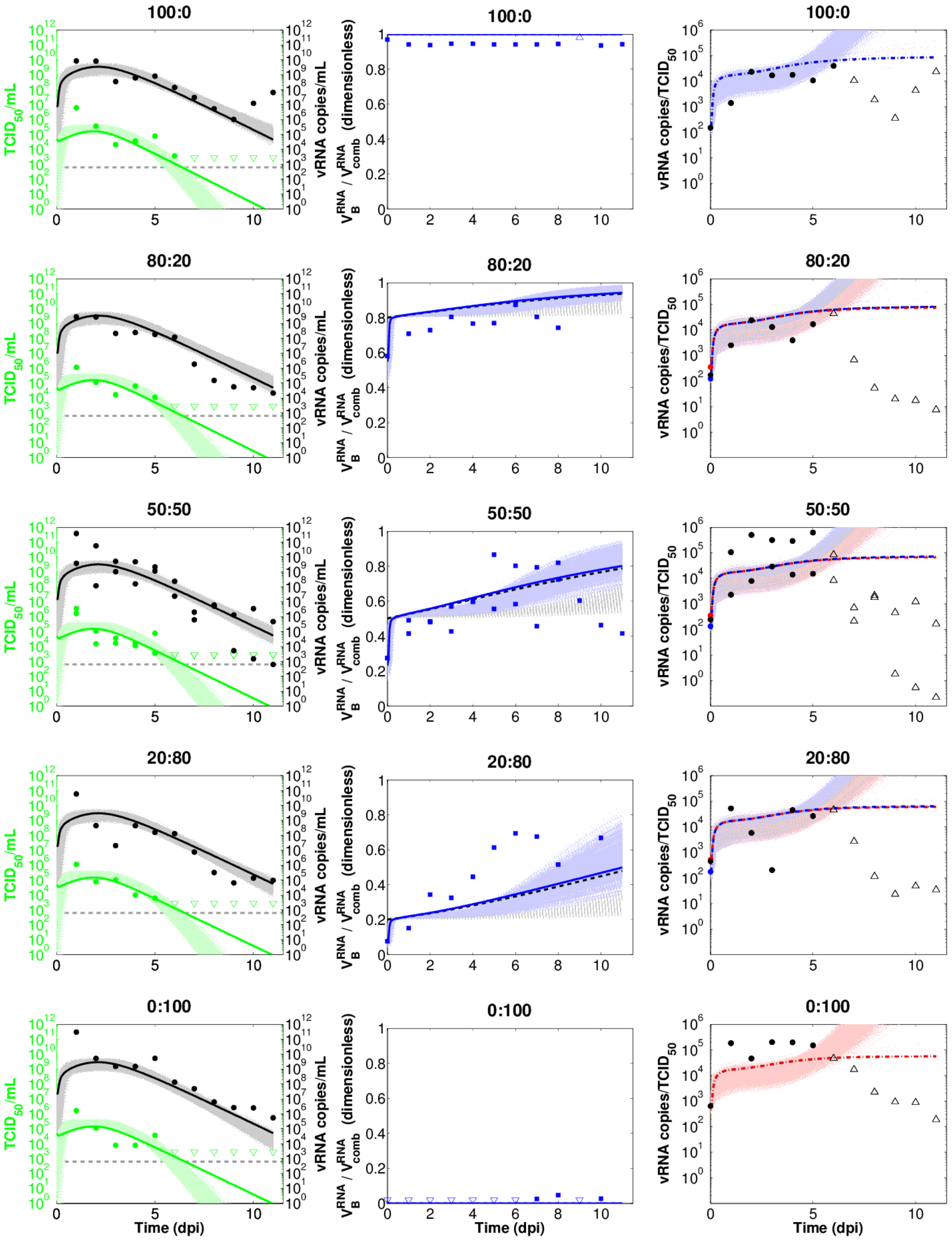

Figure S3: **Fits of the τ_V-diff model to data from the natural isolate experiment.** Each row shows viral load data for a given infection group. The 50:50 mixture was inoculated into two different ferrets in order to provide more data on infections that begin on equal footing; therefore data points may overlap in that group. *Left column:* Best fits are shown of infectious (solid green line; $V^{TCID}_{comb}(t)$) and total (solid black line; $V^{RNA}_{comb}(t)$) viral load to calibrated TCID$_{50}$ data (green dots) and rRT-PCR data (black dots; dashed grey line indicates detection threshold), respectively. *Centre column:* Best fits of the New17 OR vRNA proportion (solid blue line; $V^{RNA}_{B}/V^{RNA}_{comb}$) to pyrosequencing data (blue squares). The New17 OR *infectious* proportion is also shown (dashed black line; $V^{TCID}_{B}/V^{TCID}_{comb}$). *Right column:* Data of the rRT-PCR:TCID$_{50}$ ratio (black dots), together with the total:infectious ratio of both strains combined (dot-dashed black line; $\rho(t) = V^{RNA}_{comb}(t)/V^{TCID}_{comb}(t)$). Note that only the initial condition, $\rho(0)$, is fitted to data. The total:infectious ratio of the New163 OS (dot-dashed red line; red dot indicates initial value) and New17 OR (dot-dashed blue line; blue dot indicates initial value) strains are also shown. In all plots, non-filled arrows indicate that the measured concentration or proportion was outside of the range of detectability for the corresponding assay, with arrow direction indicating the direction of the actual, unknown quantity. In addition to the best fit lines, 5000 randomly sampled fits with SSR values that lie within the 95% confidence level of the LCR are also shown (faded dotted lines).

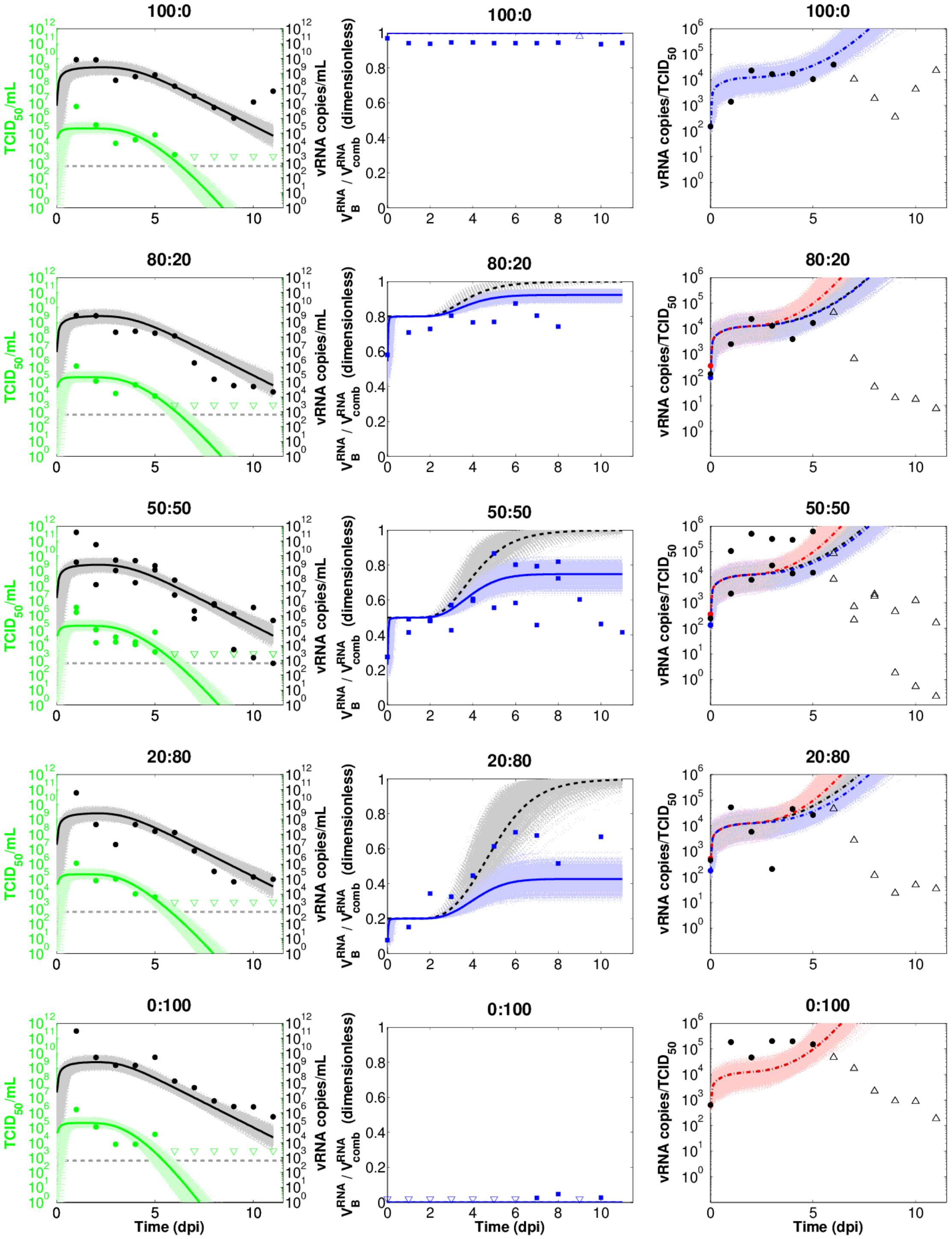

Figure S4: **Fits of the τ_I-diff model to data from the natural isolate experiment.** Each row shows viral load data for a given infection group. The 50:50 mixture was inoculated into two different ferrets in order to provide more data on infections that begin on equal footing; therefore data points may overlap in that group. *Left column:* Best fits are shown of infectious (solid green line; $V^{TCID}_{comb}(t)$) and total (solid black line; $V^{RNA}_{comb}(t)$) viral load to calibrated TCID$_{50}$ data (green dots) and rRT-PCR data (black dots; dashed grey line indicates detection threshold), respectively. *Centre column:* Best fits of the New17 OR vRNA proportion (solid blue line; V^{RNA}_B/V^{RNA}_{comb}) to pyrosequencing data (blue squares). The New17 OR *infectious* proportion is also shown (dashed black line; $V^{TCID}_B/V^{TCID}_{comb}$). *Right column:* Data of the rRT-PCR:TCID$_{50}$ ratio (black dots), together with the total:infectious ratio of both strains combined (dot-dashed black line; $\rho(t) = V^{RNA}_{comb}(t)/V^{TCID}_{comb}(t)$). Note that only the initial condition, $\rho(0)$, is fitted to data. The total:infectious ratio of the New163 OS (dot-dashed red line; red dot indicates initial value) and New17 OR (dot-dashed blue line; blue dot indicates initial value) strains are also shown. In all plots, non-filled arrows indicate that the measured concentration or proportion was outside of the range of detectability for the corresponding assay, with arrow direction indicating the direction of the actual, unknown quantity. In addition to the best fit lines, 5000 randomly sampled fits with SSR values that lie within the 95% confidence level of the LCR are also shown (faded dotted lines).

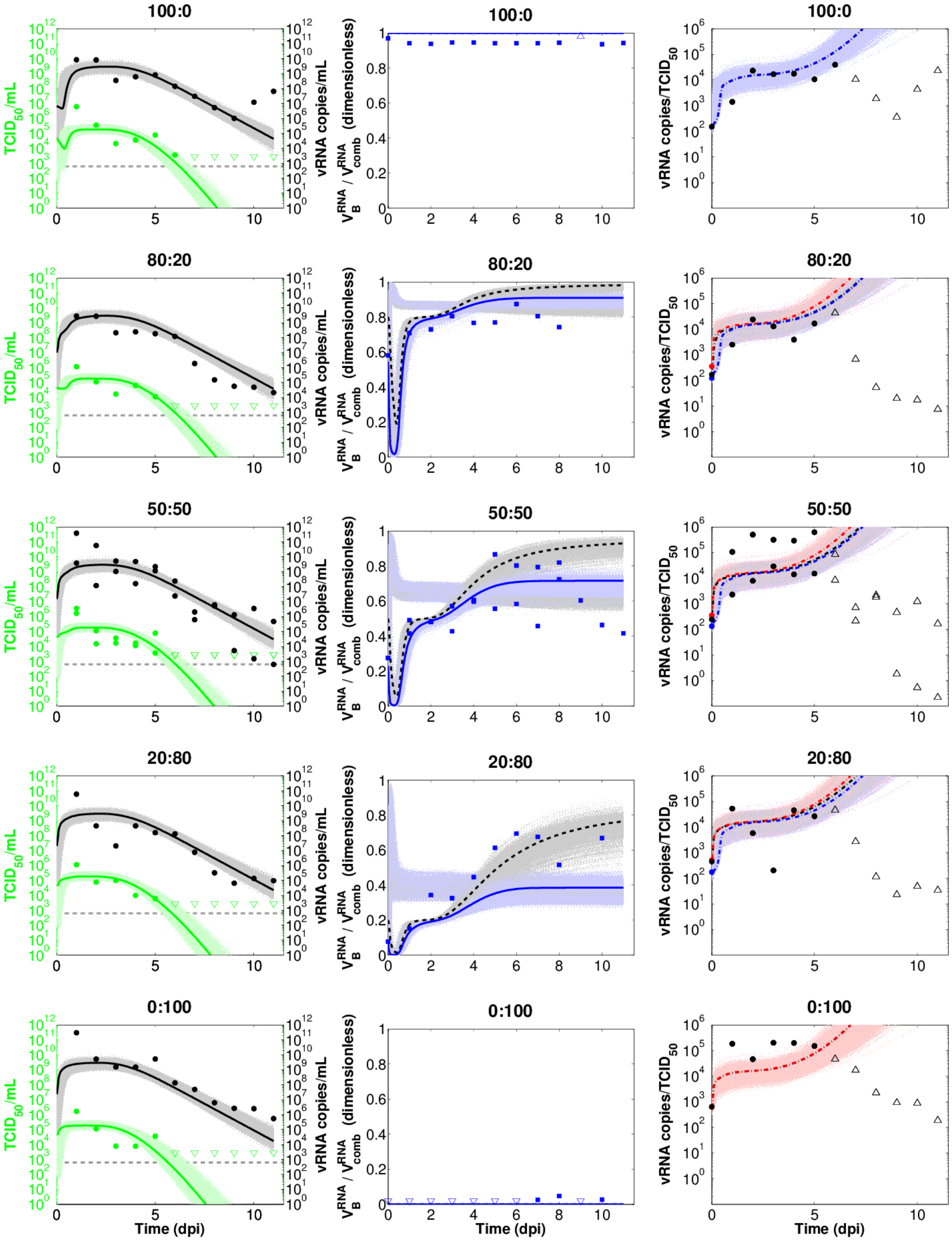

Figure S5: **Fits of the k-diff model to data from the natural isolate experiment.** Each row shows viral load data for a given infection group. The 50:50 mixture was inoculated into two different ferrets in order to provide more data on infections that begin on equal footing; therefore data points may overlap in that group. *Left column:* Best fits are shown of infectious (solid green line; $V_{comb}^{TCID}(t)$) and total (solid black line; $V_{comb}^{RNA}(t)$) viral load to calibrated TCID$_{50}$ data (green dots) and rRT-PCR data (black dots; dashed grey line indicates detection threshold), respectively. *Centre column:* Best fits of the New17 OR vRNA proportion (solid blue line; V_B^{RNA}/V_{comb}^{RNA}) to pyrosequencing data (blue squares). The New17 OR *infectious* proportion is also shown (dashed black line; $V_B^{TCID}/V_{comb}^{TCID}$). *Right column:* Data of the rRT-PCR:TCID$_{50}$ ratio (black dots), together with the total:infectious ratio of both strains combined (dot-dashed black line; $\rho(t) = V_{comb}^{RNA}(t)/V_{comb}^{TCID}(t)$). Note that only the initial condition, $\rho(0)$, is fitted to data. The total:infectious ratio of the New163 OS (dot-dashed red line; red dot indicates initial value) and New17 OR (dot-dashed blue line; blue dot indicates initial value) strains are also shown. In all plots, non-filled arrows indicate that the measured concentration or proportion was outside of the range of detectability for the corresponding assay, with arrow direction indicating the direction of the actual, unknown quantity. In addition to the best fit lines, 5000 randomly sampled fits with SSR values that lie within the 95% confidence level of the LCR are also shown (faded dotted lines).

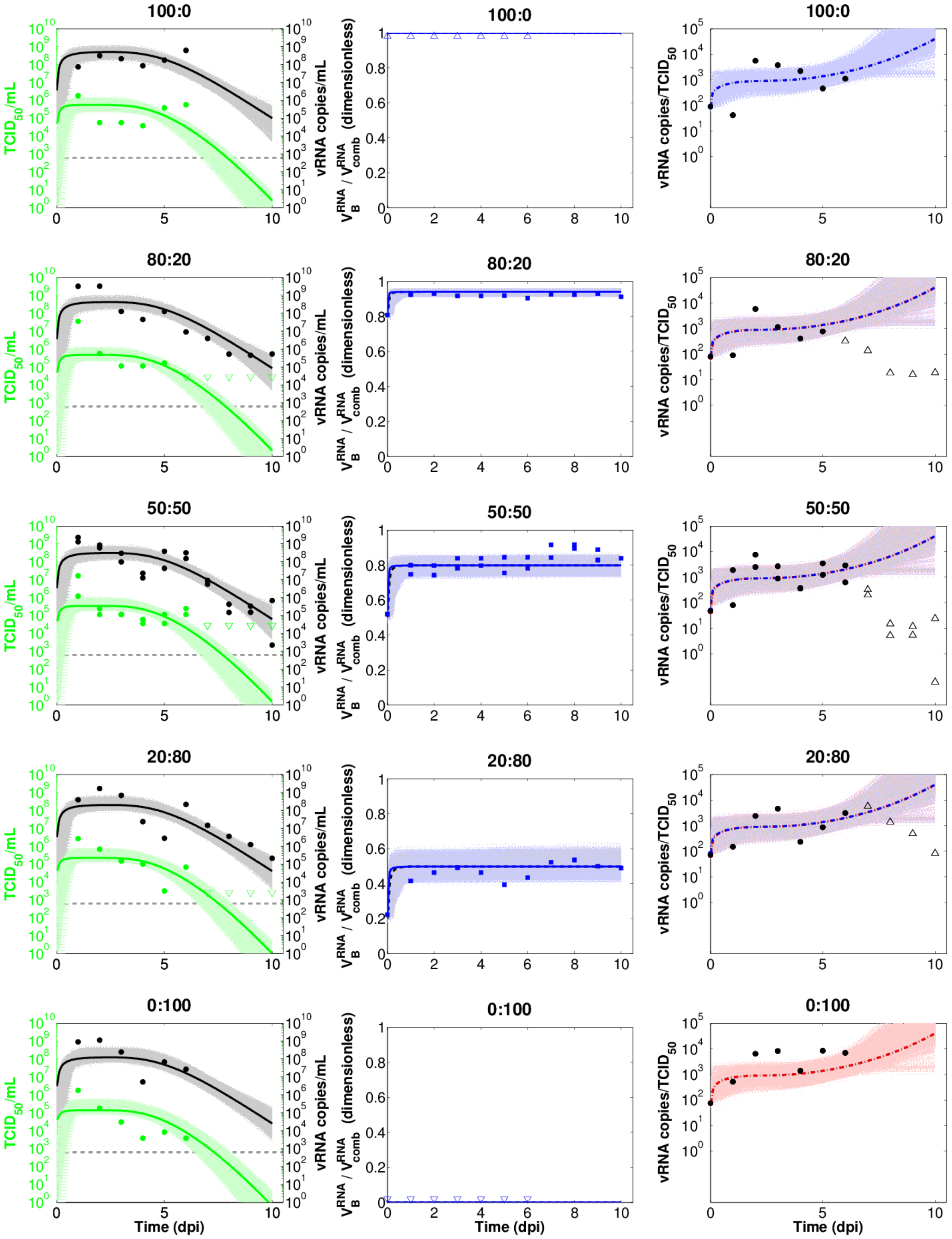

Figure S6: **Fits of the *p*-diff model to data from the *rgNew17 OR vs. rgNew17 I241V OR* experiment.** Same as Figure S5, except for the *p*-diff model fitted to the *rgNew17 OR vs. rgNew17 I241V OR* experiment.

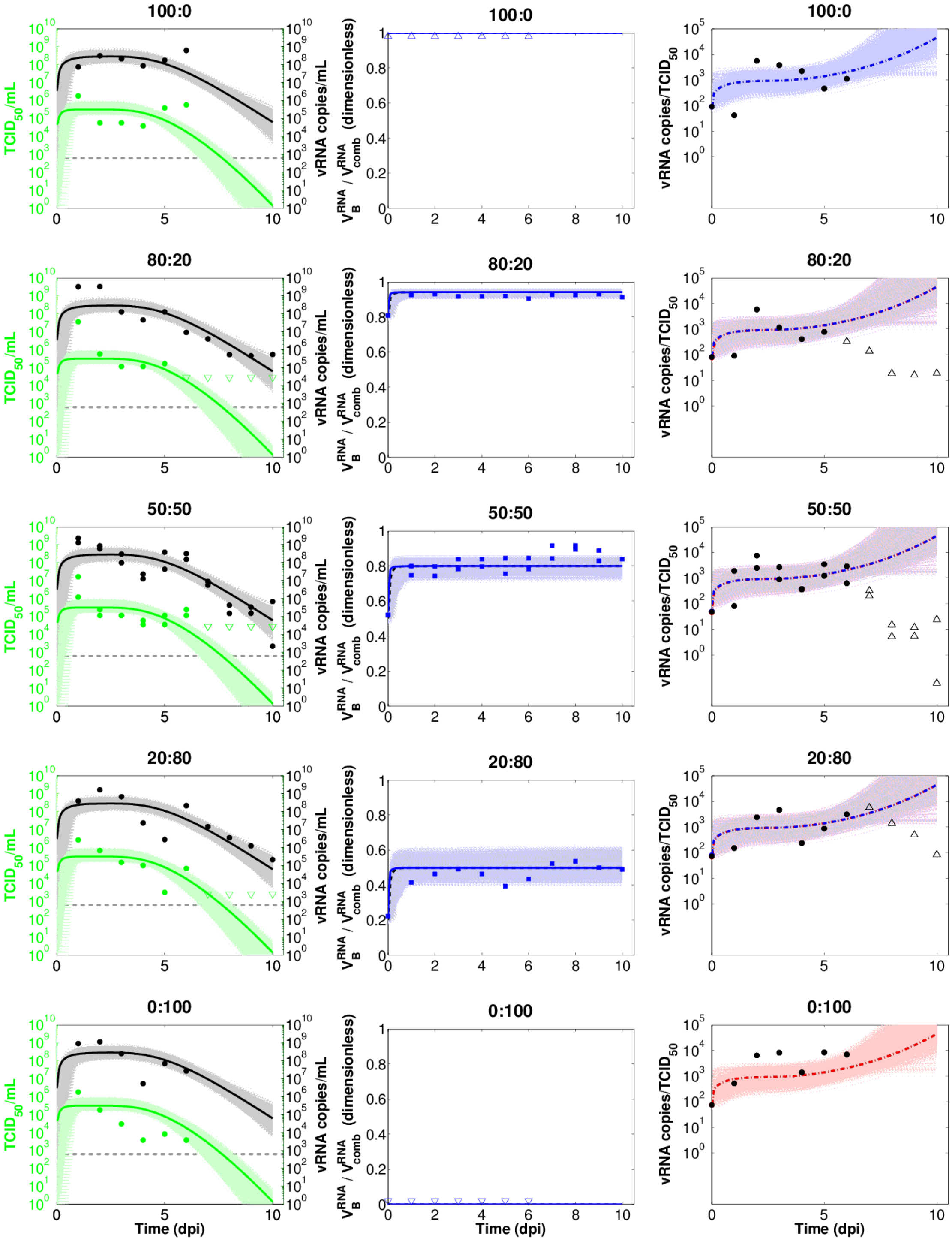

Figure S7: **Fits of the β-diff model to data from the *rgNew17 OR vs. rgNew17 I241V OR* experiment.** Same as Figure S5, except for the β-diff model fitted to the *rgNew17 OR vs. rgNew17 I241V OR* experiment.

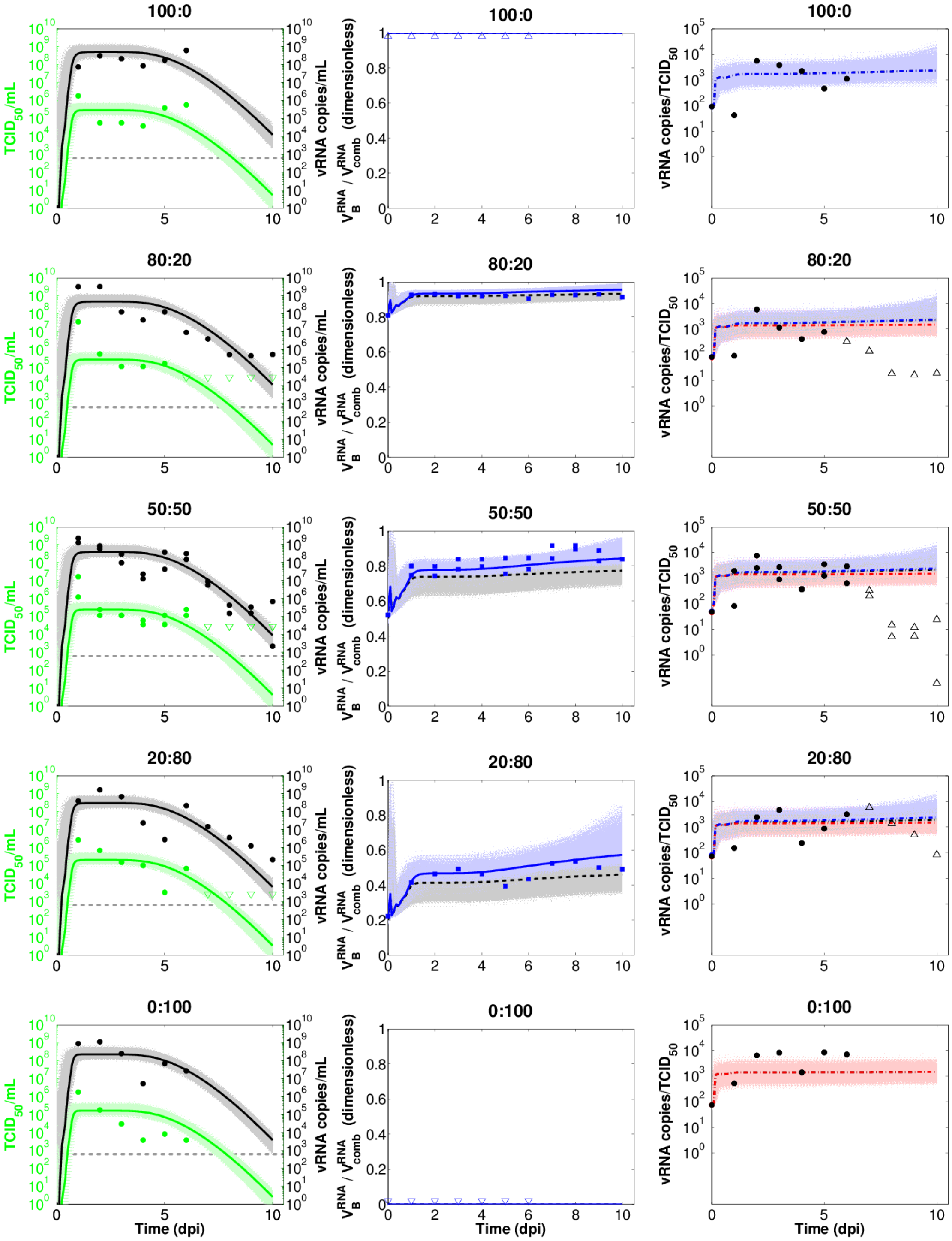

Figure S8: **Fits of the τ_V-diff model to data from the *rgNew17 OR vs. rgNew17 I241V OR* experiment.** Same as Figure S5, except for the τ_V-diff model fitted to the *rgNew17 OR vs. rgNew17 I241V OR* experiment.

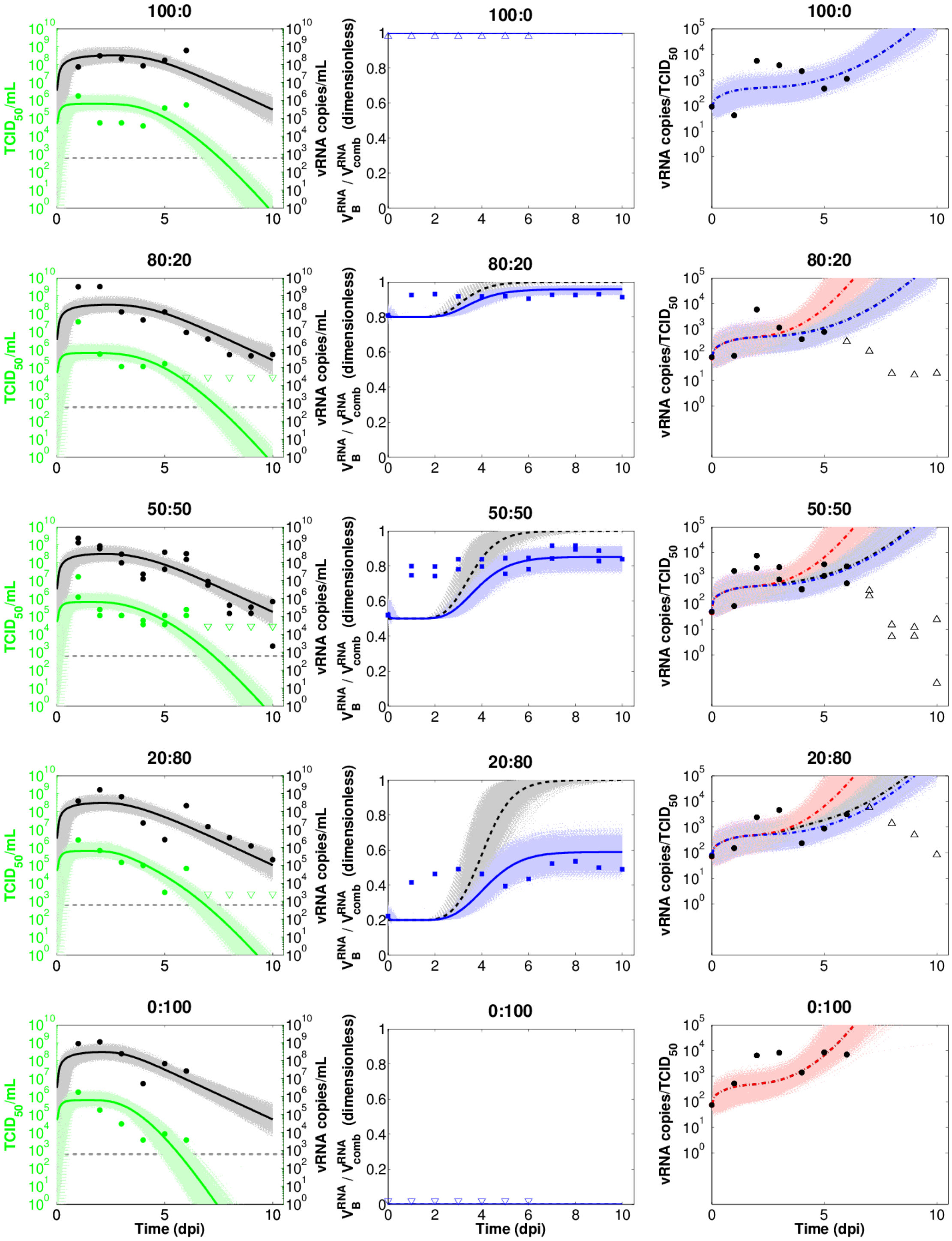

Figure S9: **Fits of the τ_I-diff model to data from the *rgNew17 OR vs. rgNew17 I241V OR* experiment.** Same as Figure S5, except for the τ_I-diff model fitted to the *rgNew17 OR vs. rgNew17 I241V OR* experiment.

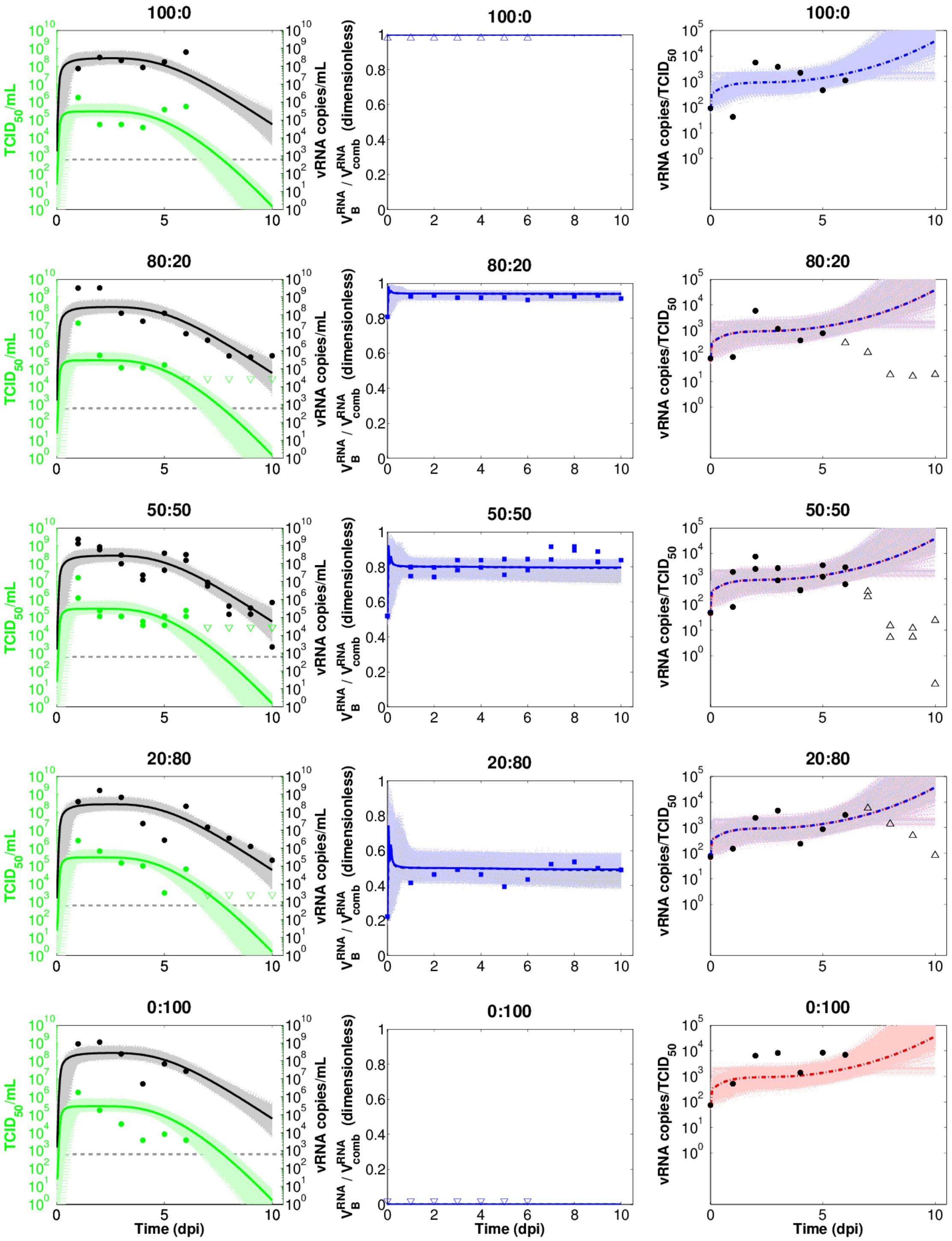

Figure S10: **Fits of the *k*-diff model to data from the *rgNew17 OR vs. rgNew17 I241V OR* experiment.** Same as Figure S5, except for the *k*-diff model fitted to the *rgNew17 OR vs. rgNew17 I241V OR* experiment.

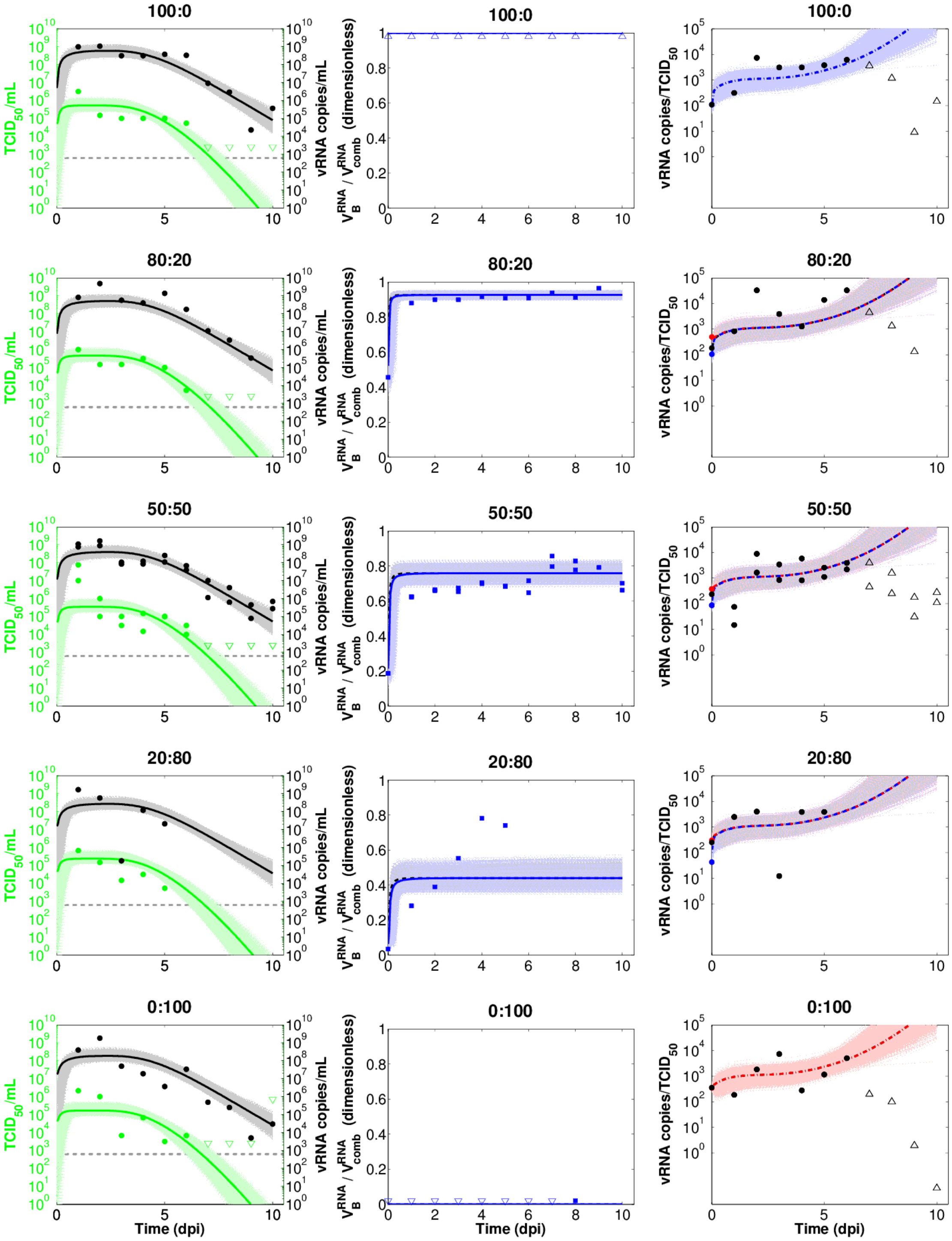

Figure S11: **Fits of the p-diff model to data from the *rgNew17 OR vs. rgNew17 K369N OR* experiment.** Same as Figure S5, except for the p-diff model fitted to the *rgNew17 OR vs. rgNew17 K369N OR* experiment.

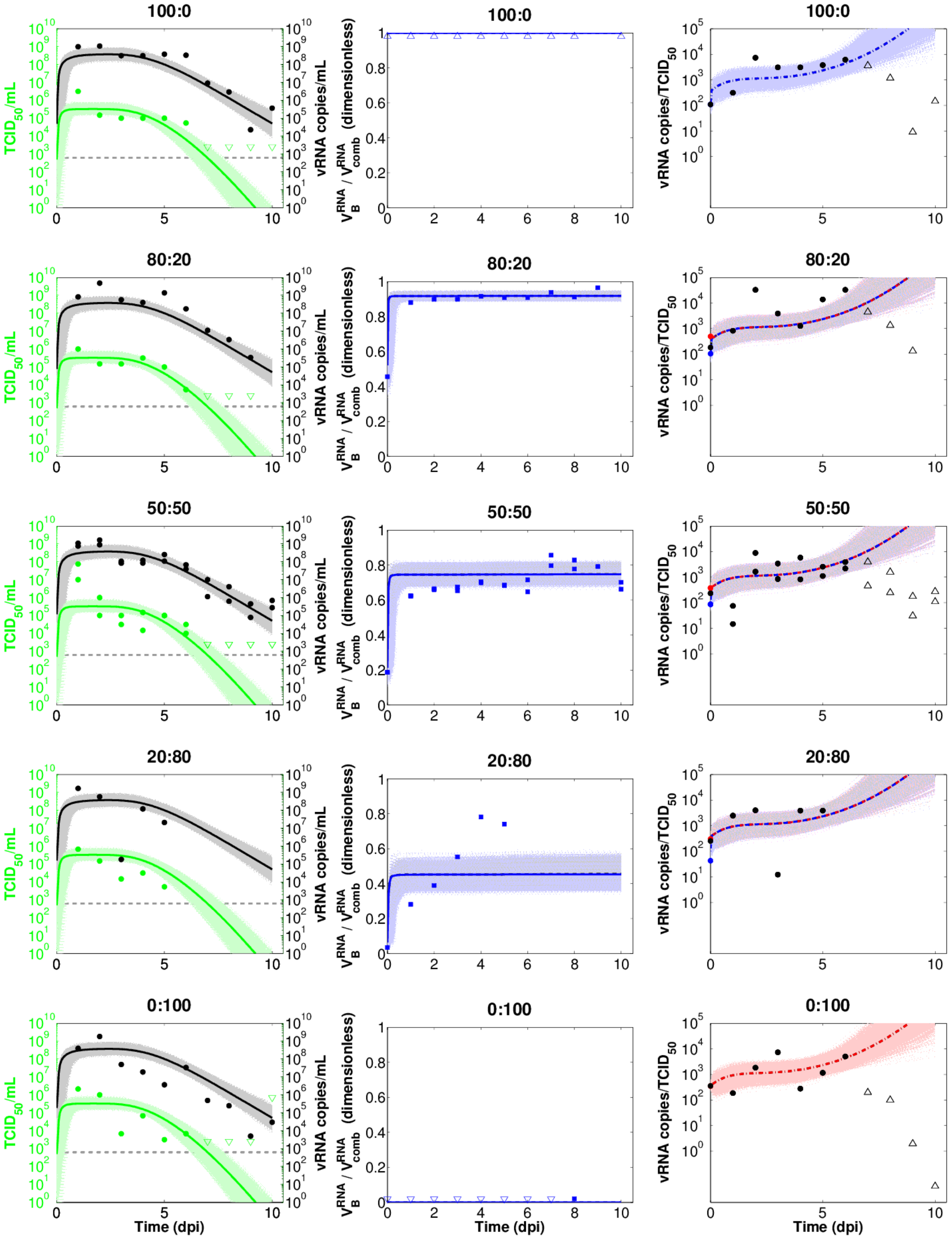

Figure S12: **Fits of the β-diff model to data from the *rgNew17 OR vs. rgNew17 K369N OR* experiment.** Same as Figure S5, except for the β-diff model fitted to the *rgNew17 OR vs. rgNew17 K369N OR* experiment.

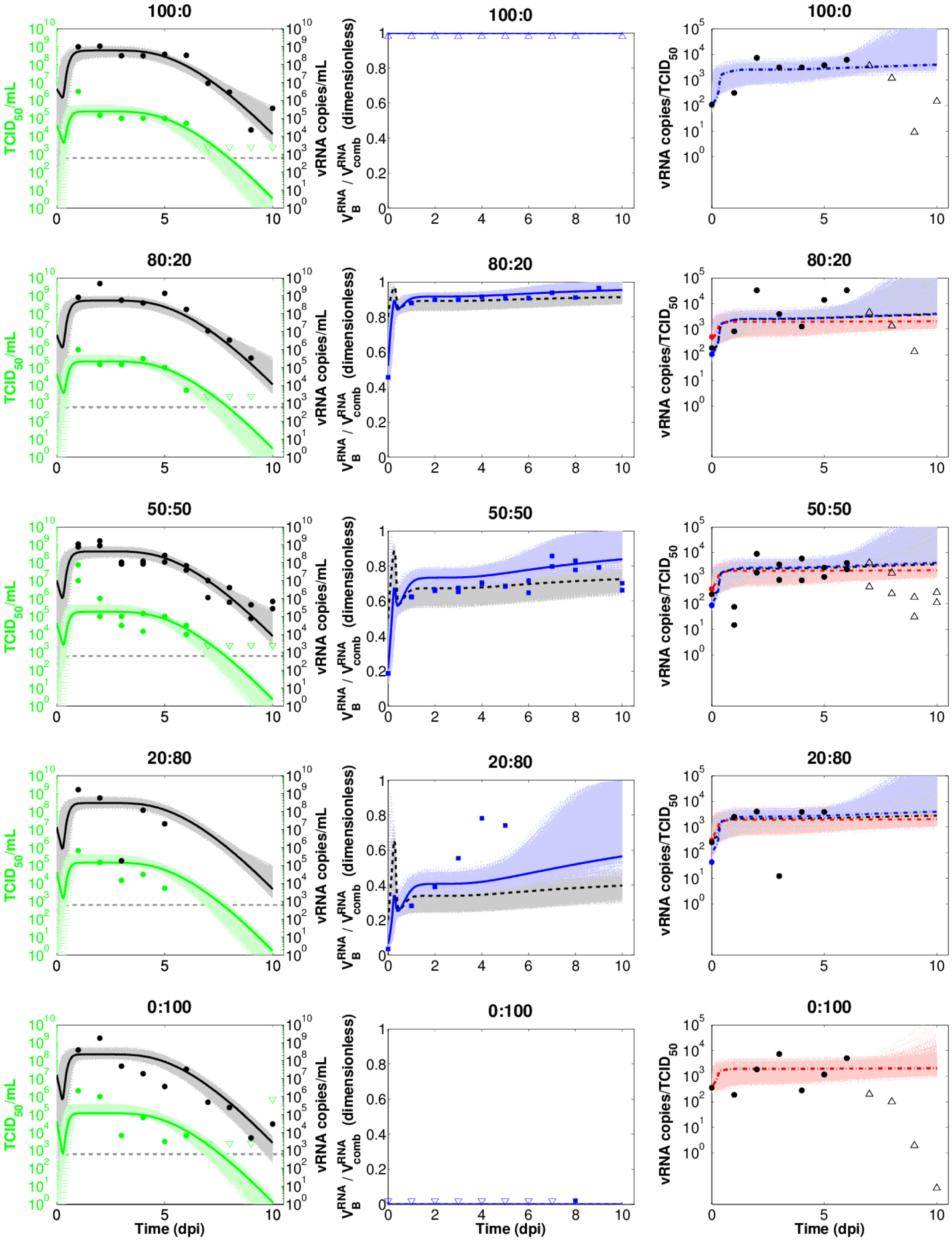

Figure S13: **Fits of the τ_V-diff model to data from the *rgNew17 OR vs. rgNew17 K369N OR* experiment.** Same as Figure S5, except for the τ_V-diff model fitted to the *rgNew17 OR vs. rgNew17 K369N OR* experiment.

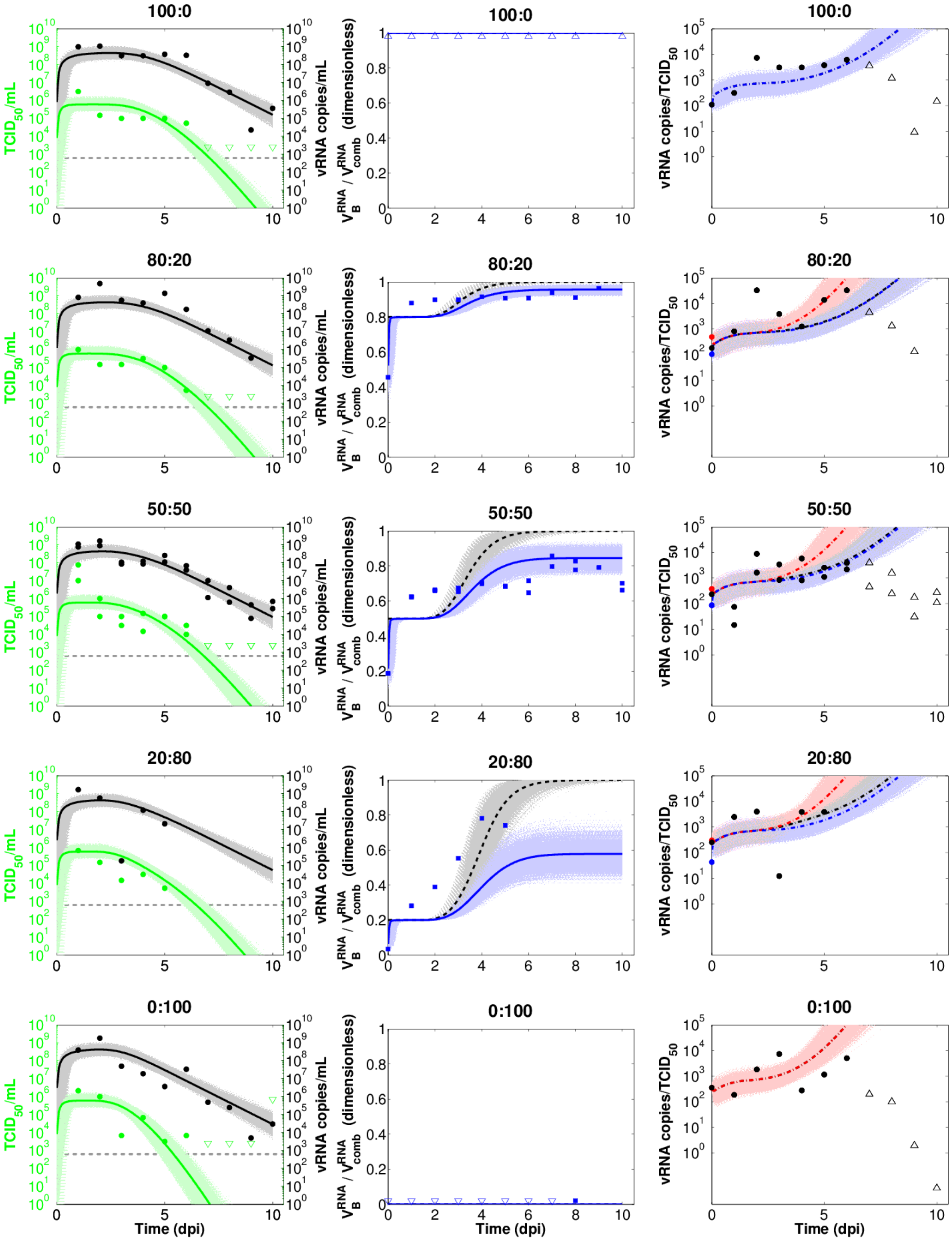

Figure S14: **Fits of the τ_I-diff model to data from the *rgNew17 OR vs. rgNew17 K369N OR* experiment.** Same as Figure S5, except for the τ_I-diff model fitted to the *rgNew17 OR vs. rgNew17 K369N OR* experiment.

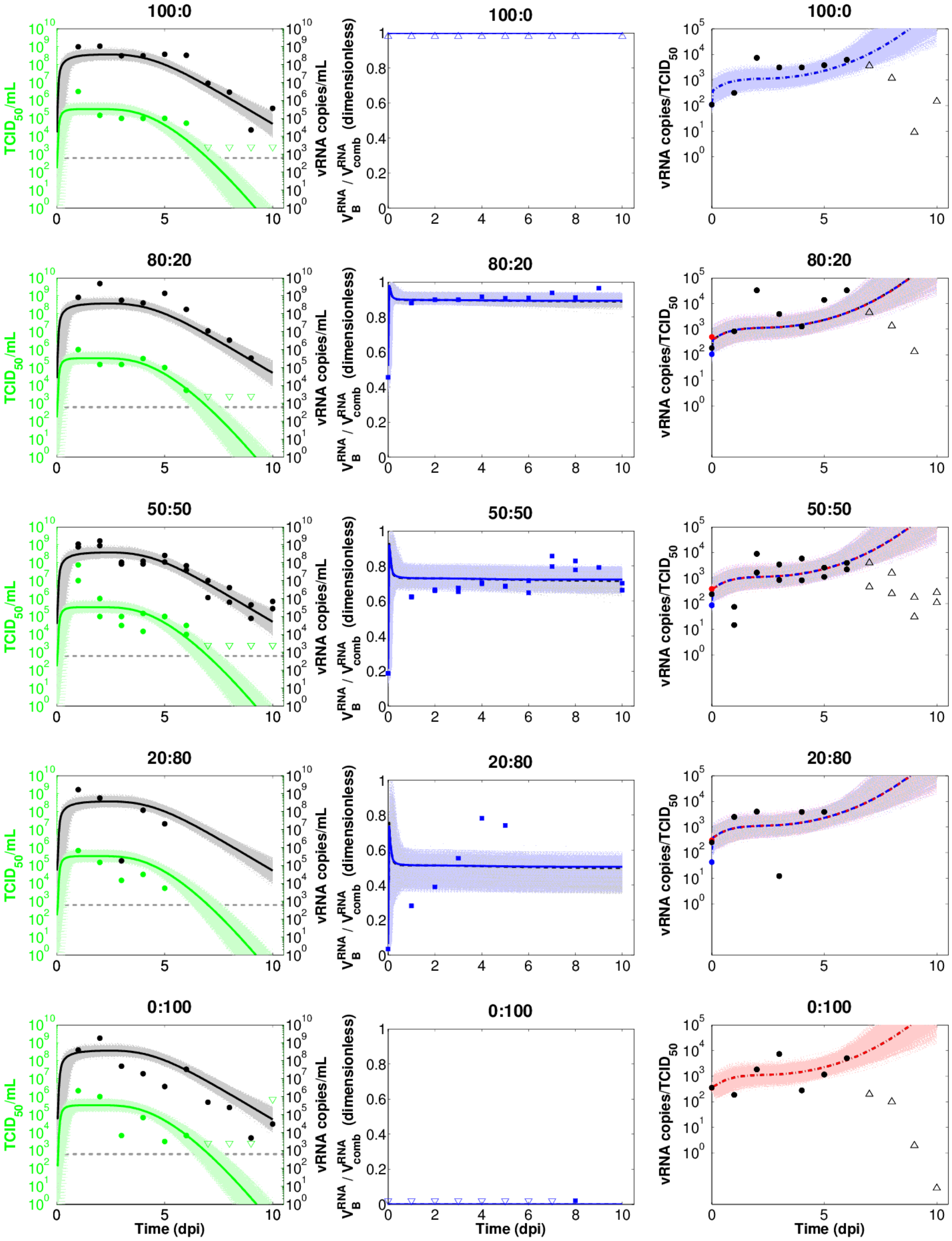

Figure S15: **Fits of the *k*-diff model to data from the *rgNew17 OR vs. rgNew17 K369N OR* experiment.** Same as Figure S5, except for the *k*-diff model fitted to the *rgNew17 OR vs. rgNew17 K369N OR* experiment.

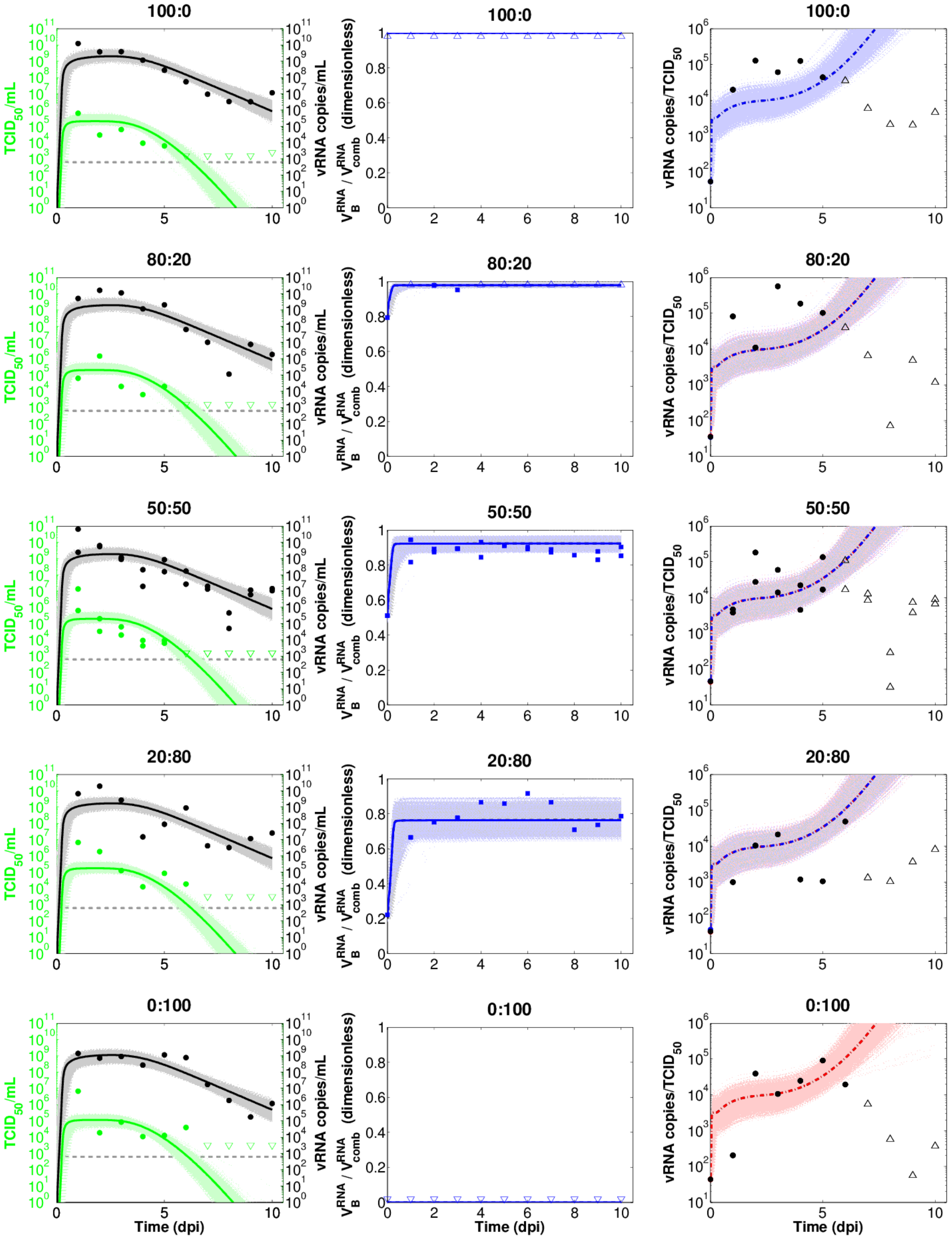

Figure S16: **Fits of the *p*-diff model to data from the *rgNew17 OR vs. rgNew17 I241V, K369N OR* experiment.** Same as Figure S5, except for the *p*-diff model fitted to the *rgNew17 OR vs. rgNew17 I241V, K369N OR* experiment.

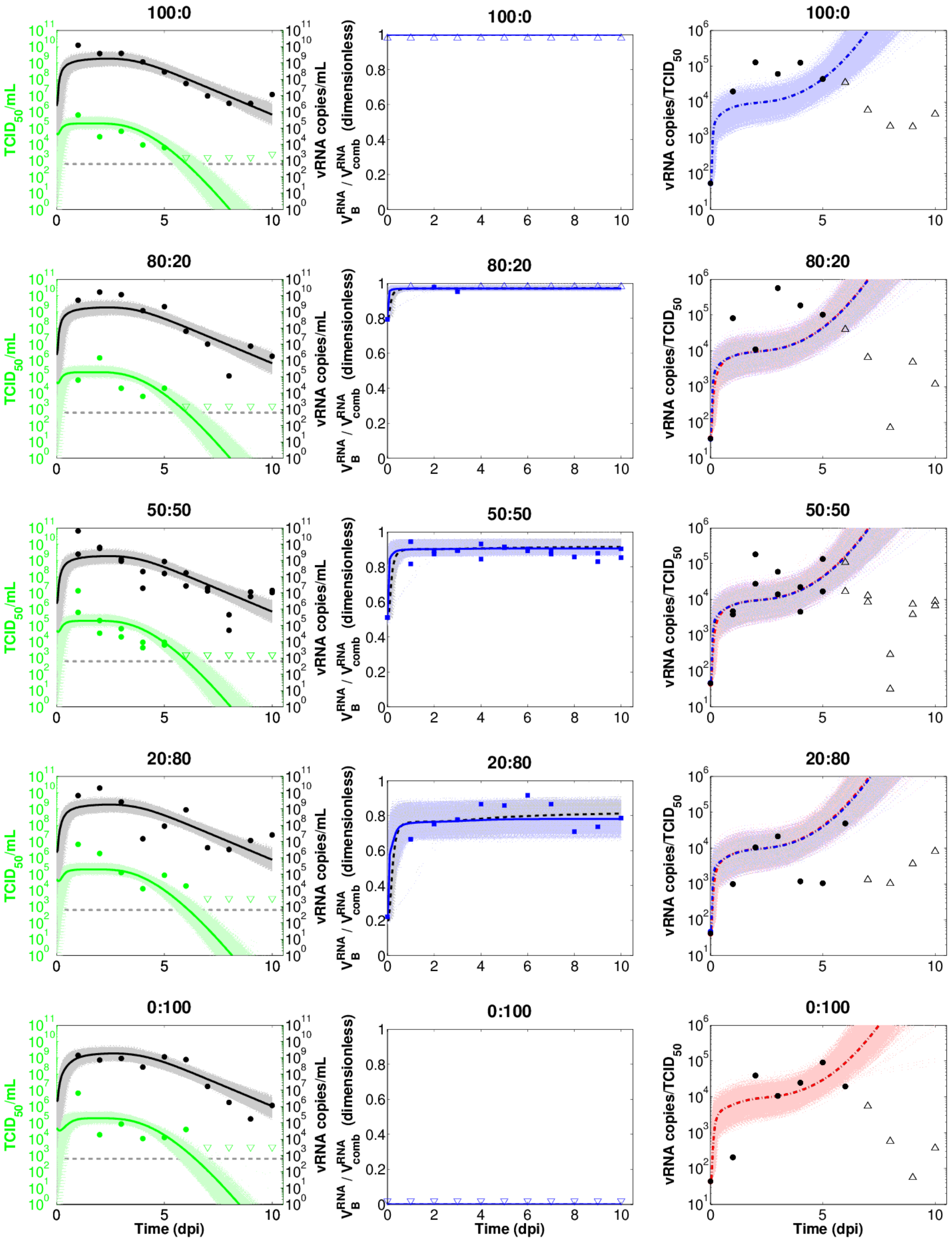

Figure S17: **Fits of the β-diff model to data from the *rgNew17 OR vs. rgNew17 I241V, K369N OR* experiment.** Same as Figure S5, except for the β-diff model fitted to the *rgNew17 OR vs. rgNew17 I241V, K369N OR* experiment.

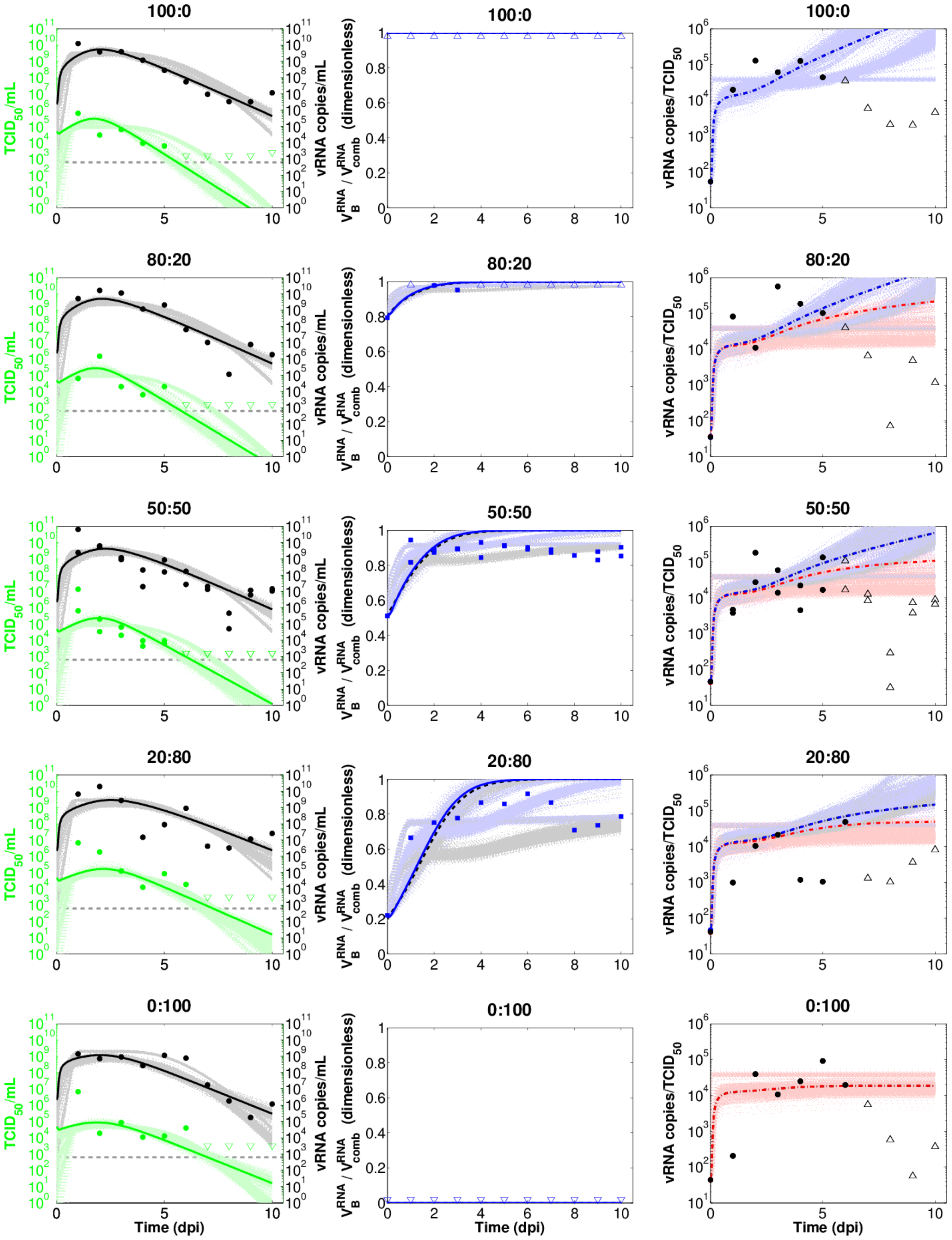

Figure S18: **Fits of the τ_V-diff model to data from the *rgNew17 OR vs. rgNew17 I241V, K369N OR* experiment.** Same as Figure S5, except for the τ_V-diff model fitted to the *rgNew17 OR vs. rgNew17 I241V, K369N OR* experiment.

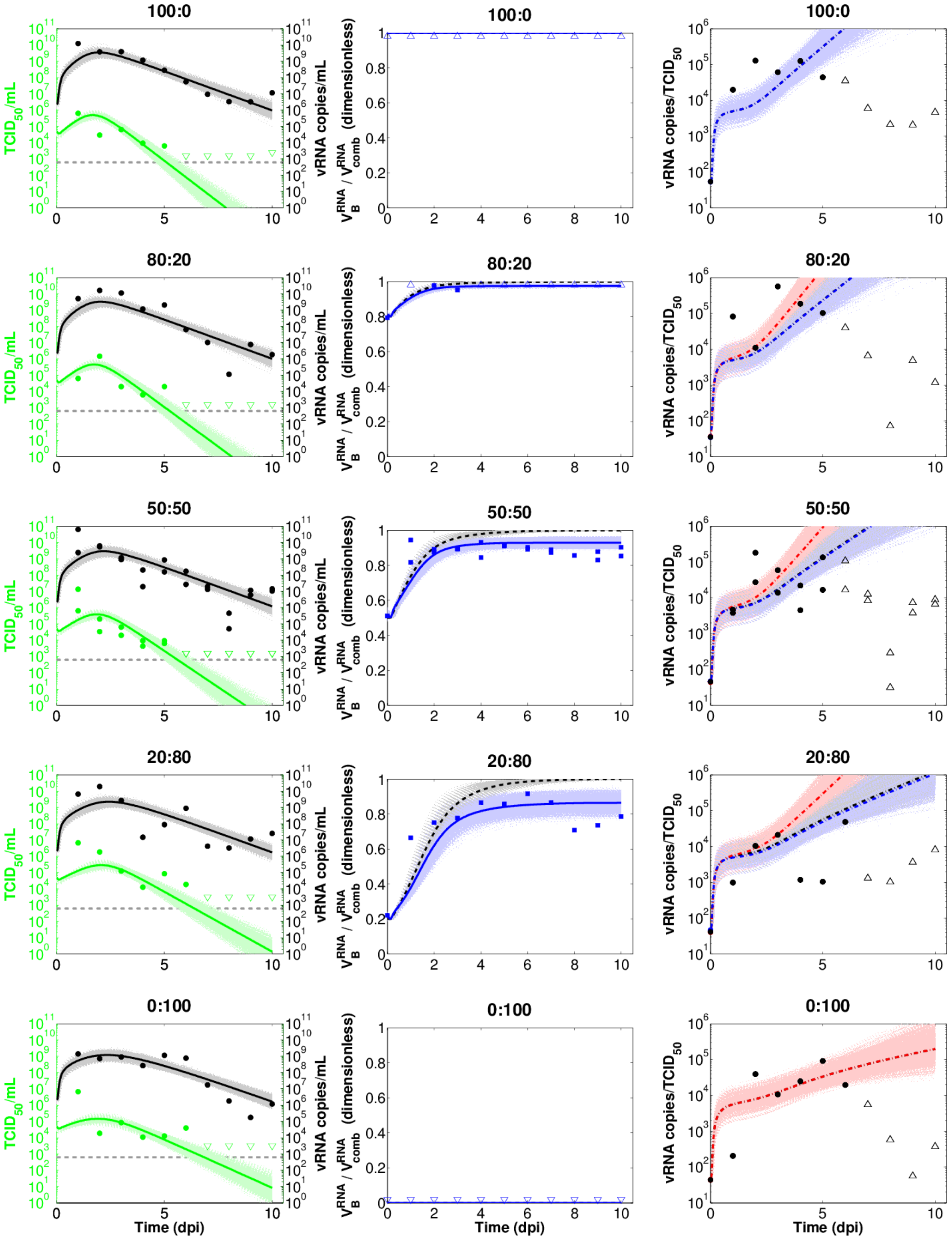

Figure S19: **Fits of the τ_I-diff model to data from the *rgNew17 OR vs. rgNew17 I241V, K369N OR* experiment.** Same as Figure S5, except for the τ_I-diff model fitted to the *rgNew17 OR vs. rgNew17 I241V, K369N OR* experiment.

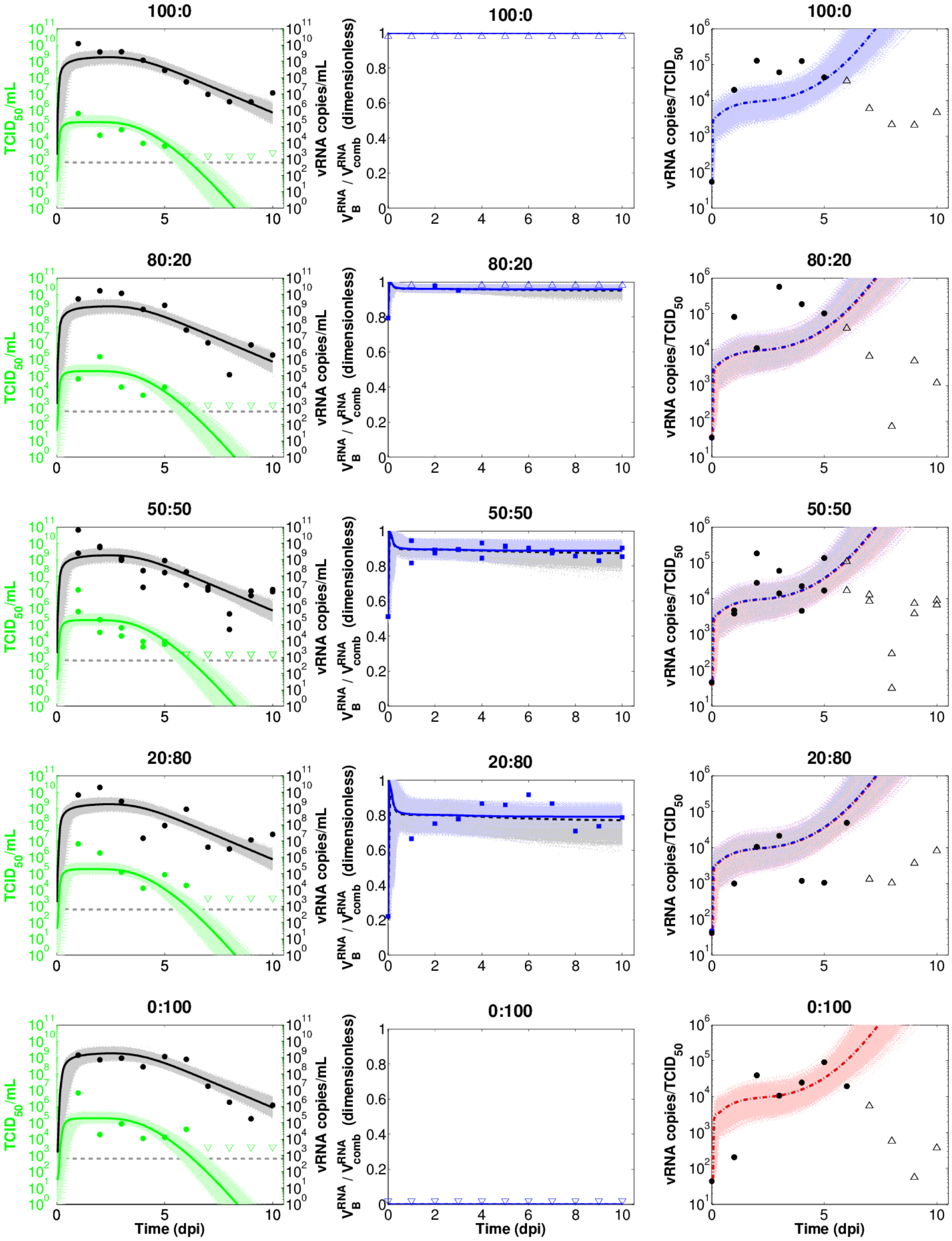

Figure S20: **Fits of the *k*-diff model to data from the *rgNew17 OR vs. rgNew17 I241V, K369N OR* experiment.** Same as Figure S5, except for the *k*-diff model fitted to the *rgNew17 OR vs. rgNew17 I241V, K369N OR* experiment.

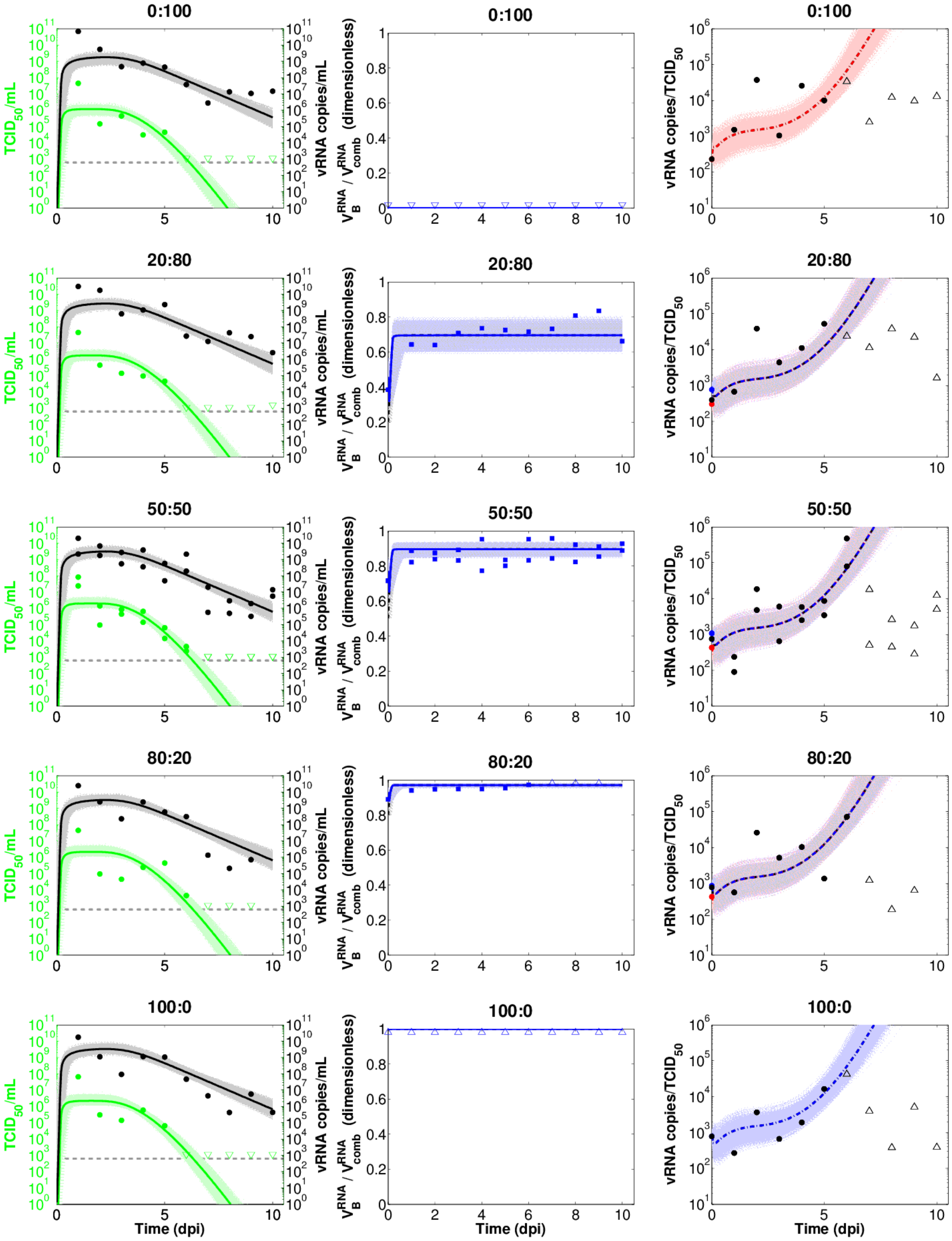

Figure S21: **Fits of the** ***p*****-diff model to data from the** ***rgPerth261 V241I, N369K OR vs. rgPerth261 OR*** **experiment.** Same as Figure S5, except for the *p*-diff model fitted to the *rgPerth261 V241I, N369K OR vs. rgPerth261 OR* experiment.

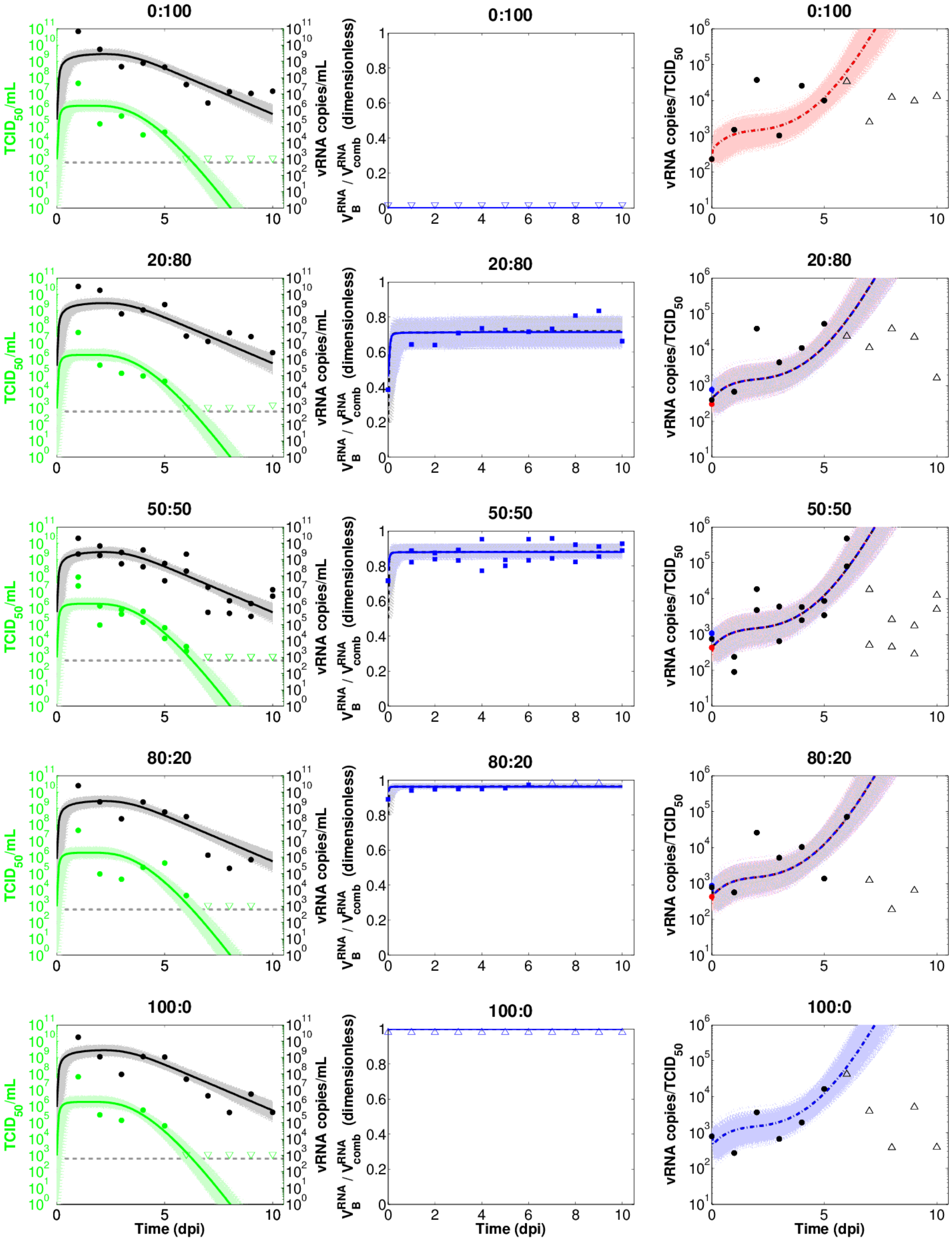

Figure S22: **Fits of the β-diff model to data from the *rgPerth261 V241I, N369K OR vs. rgPerth261 OR* experiment.** Same as Figure S5, except for the β-diff model fitted to the *rgPerth261 V241I, N369K OR vs. rgPerth261 OR* experiment.

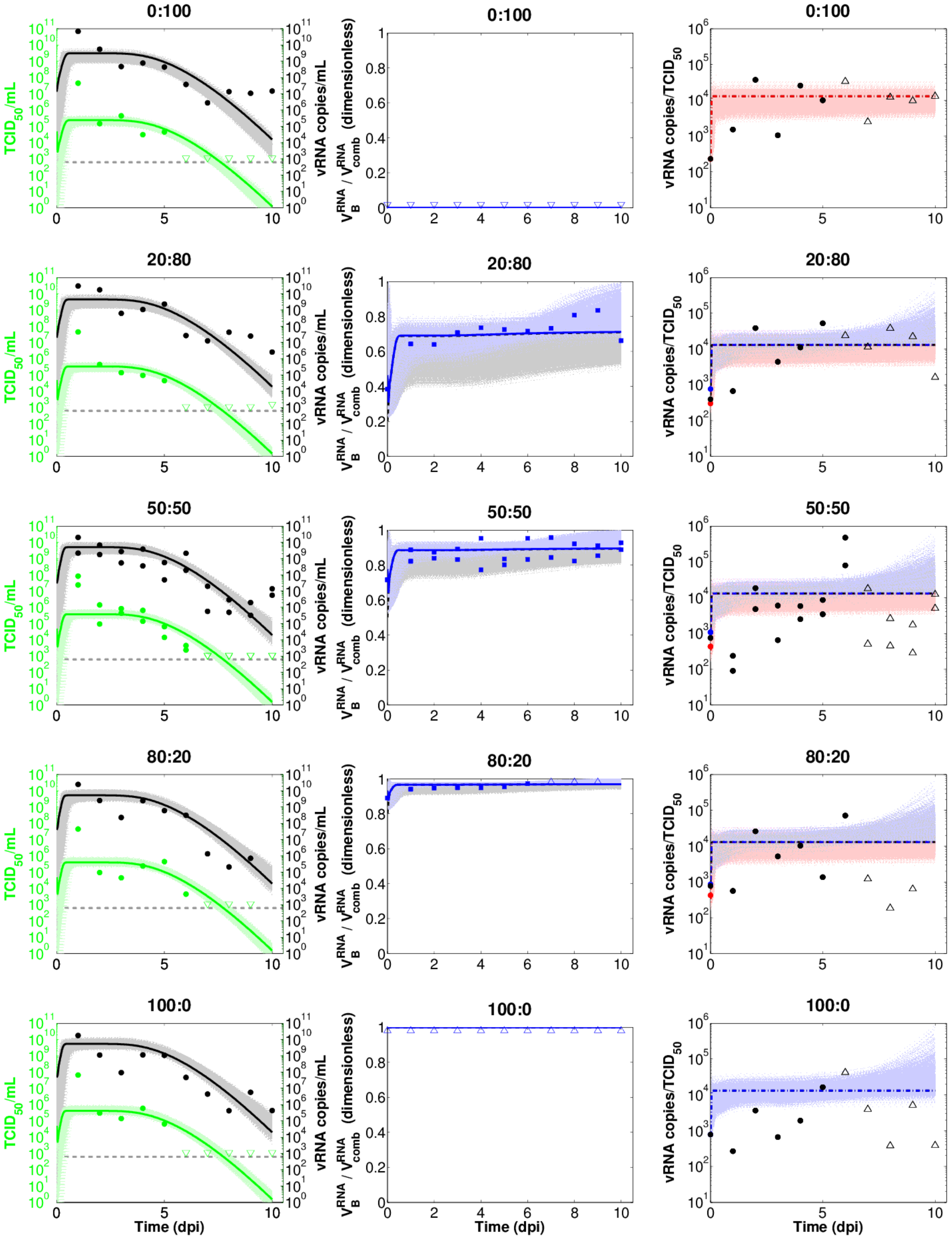

Figure S23: **Fits of the τ_V-diff model to data from the *rgPerth261 V241I, N369K OR vs. rgPerth261 OR* experiment.** Same as Figure S5, except for the τ_V-diff model fitted to the *rgPerth261 V241I, N369K OR vs. rgPerth261 OR* experiment.

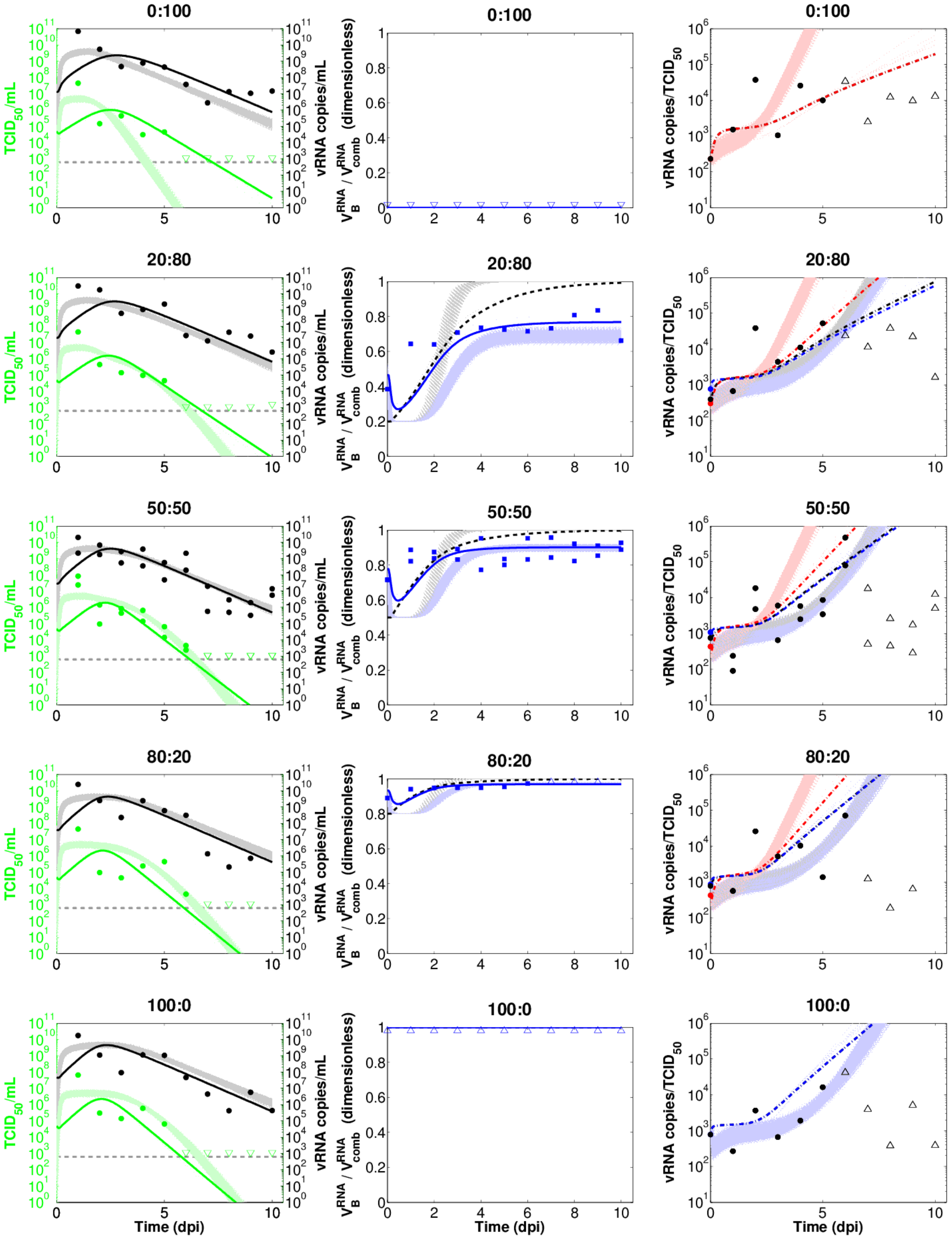

Figure S24: **Fits of the τ_I-diff model to data from the *rgPerth261 V241I, N369K OR vs. rgPerth261 OR* experiment.** Same as Figure S5, except for the τ_I-diff model fitted to the *rgPerth261 V241I, N369K OR vs. rgPerth261 OR* experiment.

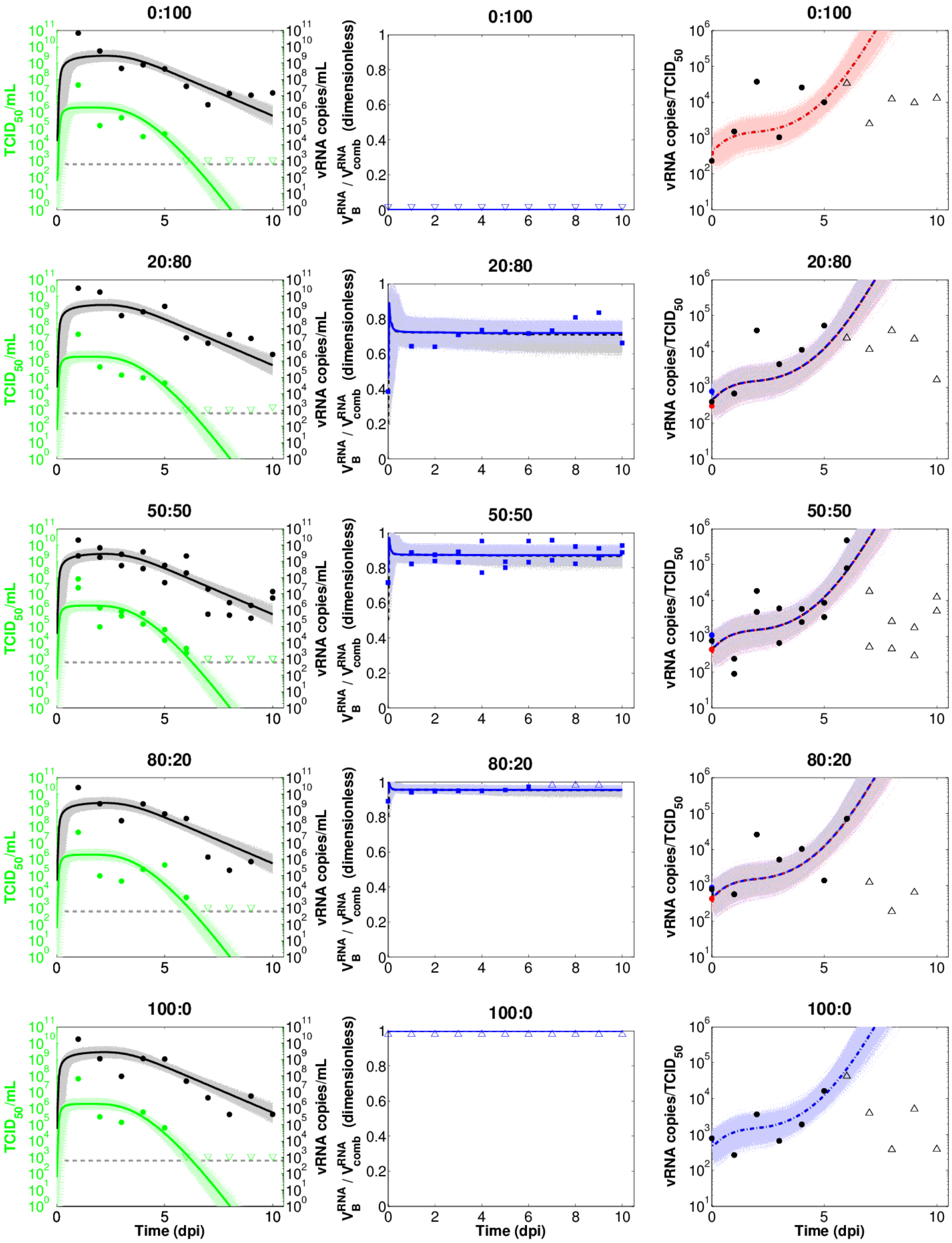

Figure S25: **Fits of the *k*-diff model to data from the *rgPerth261 V241I, N369K OR vs. rgPerth261 OR* experiment.** Same as Figure S5, except for the *k*-diff model fitted to the *rgPerth261 V241I, N369K OR vs. rgPerth261 OR* experiment.

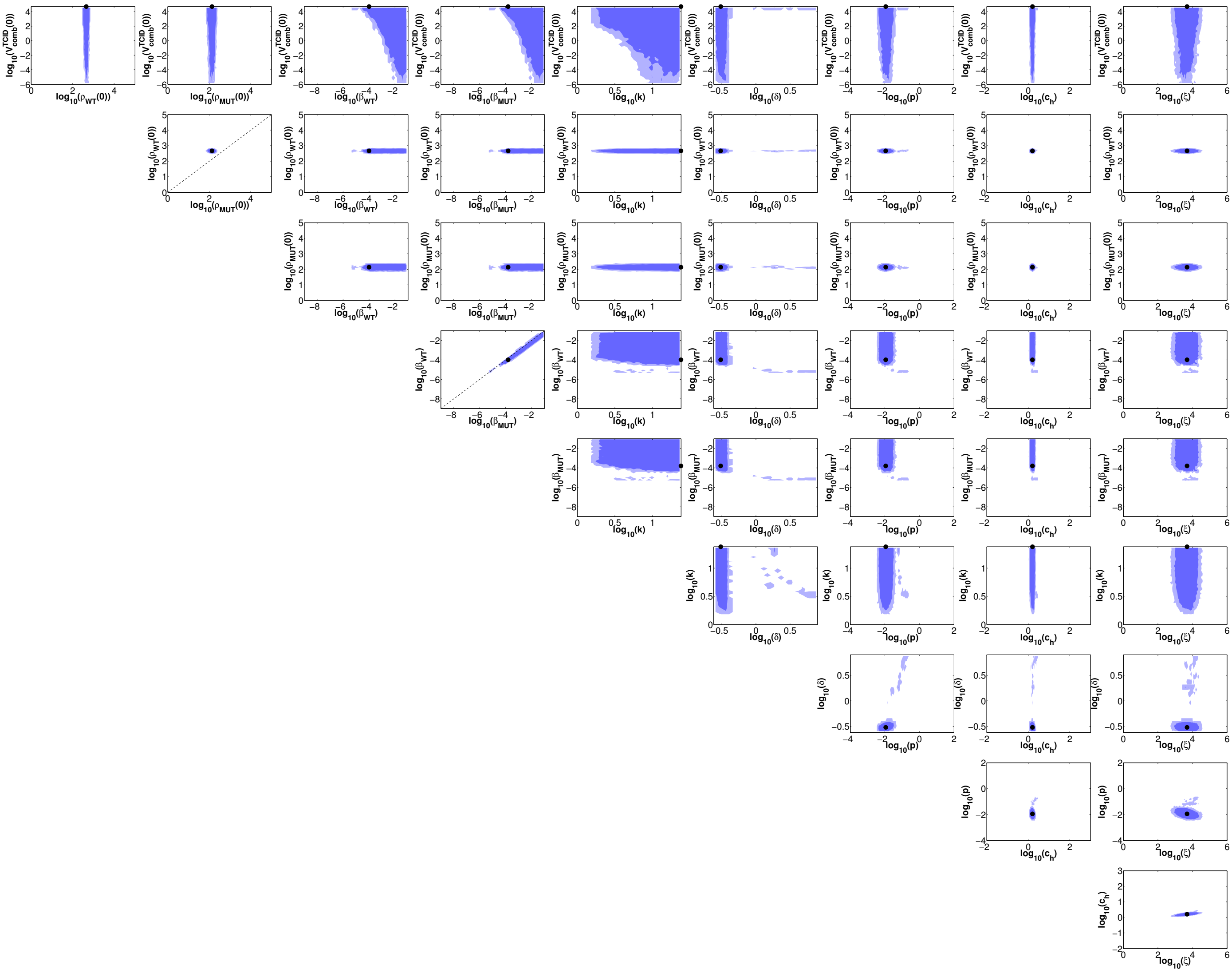

Figure S26: **LCR projections for the β-diff model fitted to the natural isolate dataset.** Best-fits (black dots) and 2-dimensional projections of the 68% LCR (dark blue contours) and 95% LCR (light blue contours) are shown for each model parameter, for the β-diff model fitted to data from the natural isolate experiment. Dashed lines show $\rho_{WT}(0) = \rho_{MUT}(0)$ and $\beta_{WT} = \beta_{MUT}$. All axis bounds correspond to the biologically realistic ranges imposed during fitting (see Table 2).

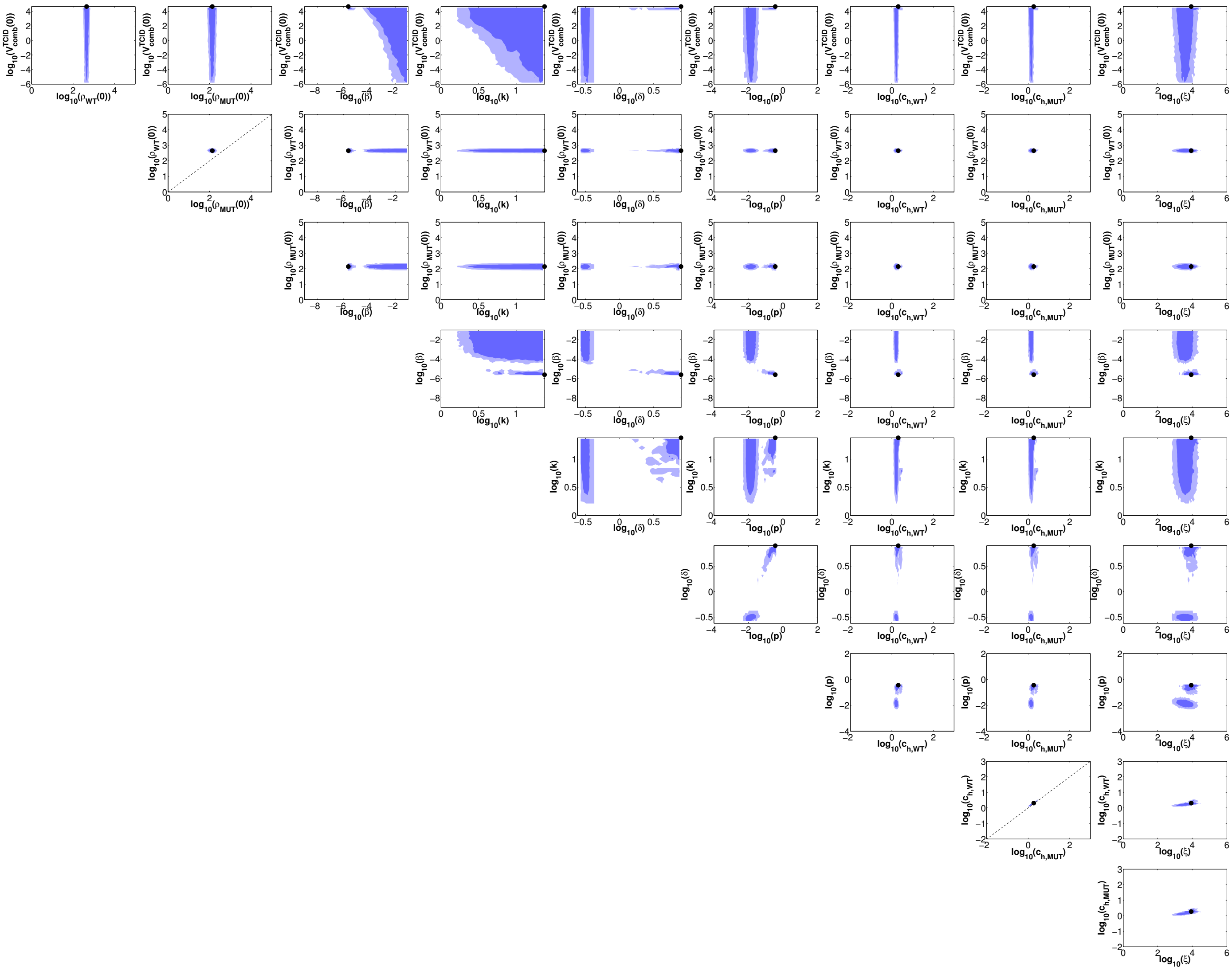

Figure S27: **LCR projections for the τ_V-diff model fitted to the natural isolate dataset.** Best-fits (black dots) and 2-dimensional projections of the 68% LCR (dark blue contours) and 95% LCR (light blue contours) are shown for each model parameter, for the τ_V-diff model fitted to data from the natural isolate experiment. Dashed lines show $\rho_{WT}(0) = \rho_{MUT}(0)$ and $c_{h,WT} = c_{h,MUT}$. All axis bounds correspond to the biologically realistic ranges imposed during fitting (see Table 2).

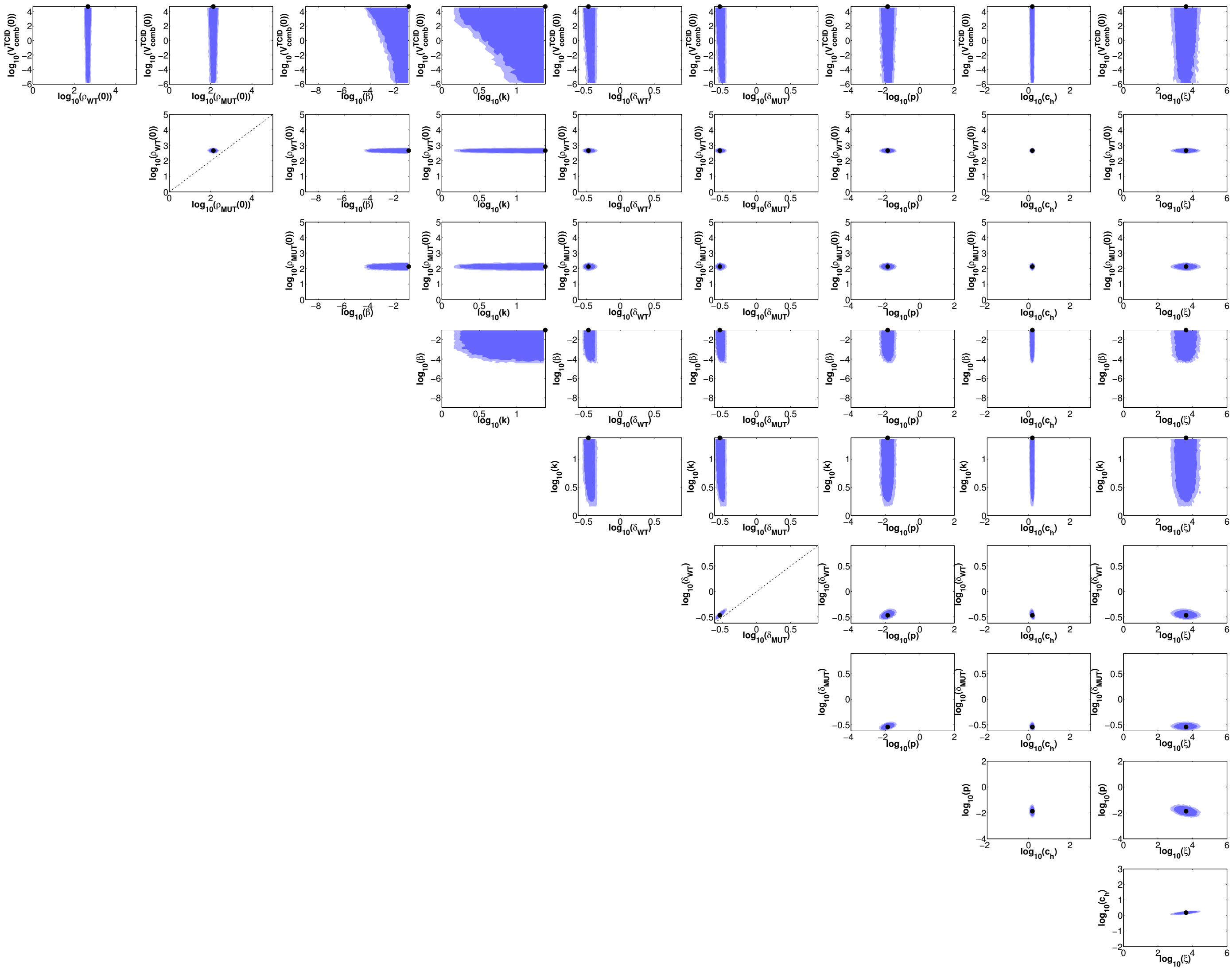

Figure S28: **LCR projections for the τ_I-diff model fitted to the natural isolate dataset.** Best-fits (black dots) and 2-dimensional projections of the 68% LCR (dark blue contours) and 95% LCR (light blue contours) are shown for each model parameter, for the τ_I-diff model fitted to data from the natural isolate experiment. Dashed lines show $\rho_{WT}(0) = \rho_{MUT}(0)$ and $\delta_{WT} = \delta_{MUT}$. All axis bounds correspond to the biologically realistic ranges imposed during fitting (see Table 2).

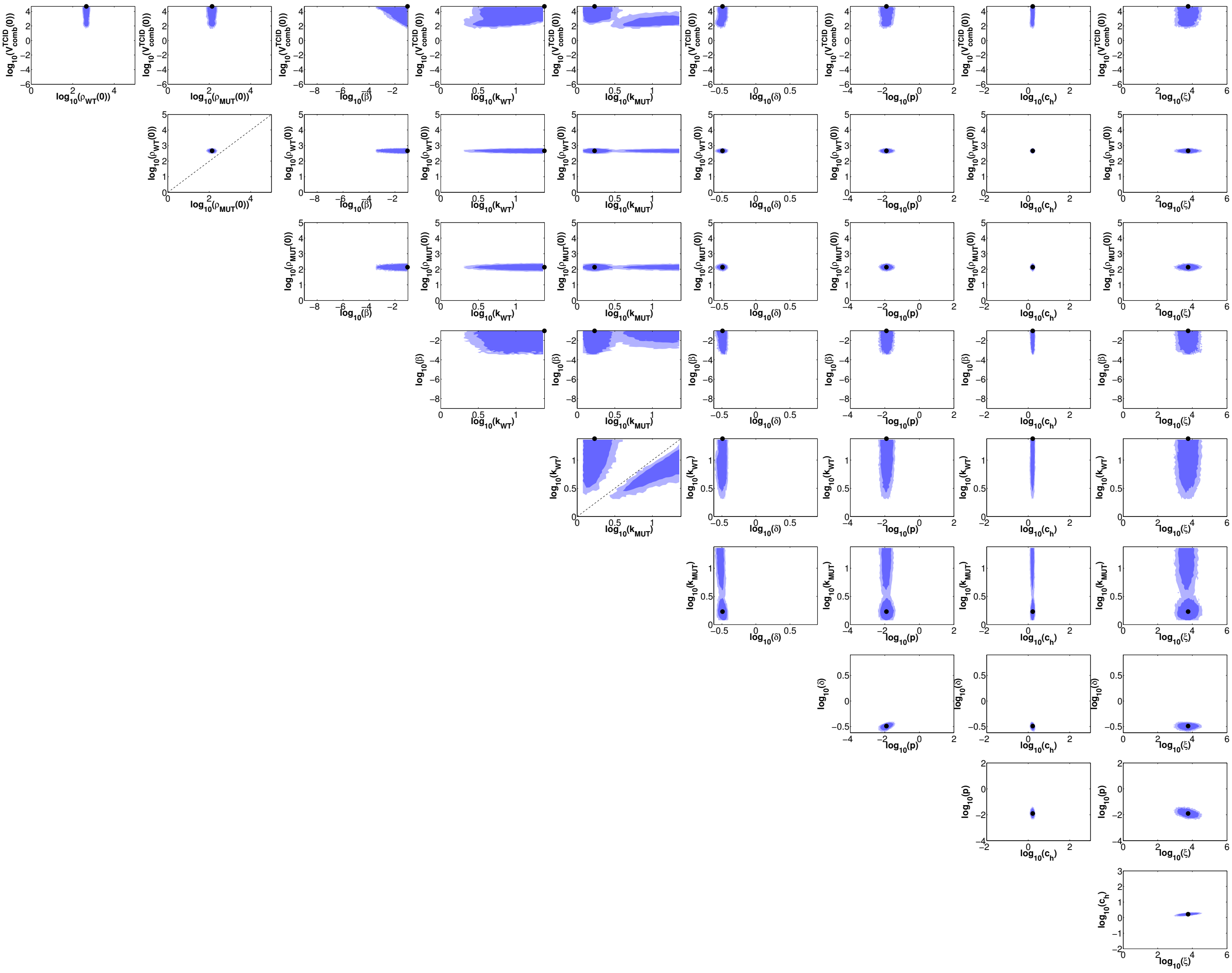

Figure S29: **LCR projections for the *k*-diff model fitted to the natural isolate dataset.** Best-fits (black dots) and 2-dimensional projections of the 68% LCR (dark blue contours) and 95% LCR (light blue contours) are shown for each model parameter, for the *k*-diff model fitted to data from the natural isolate experiment. Dashed lines show $\rho_{WT}(0) = \rho_{MUT}(0)$ and $k_{WT} = k_{MUT}$. All axis bounds correspond to the biologically realistic ranges imposed during fitting (see Table 2).

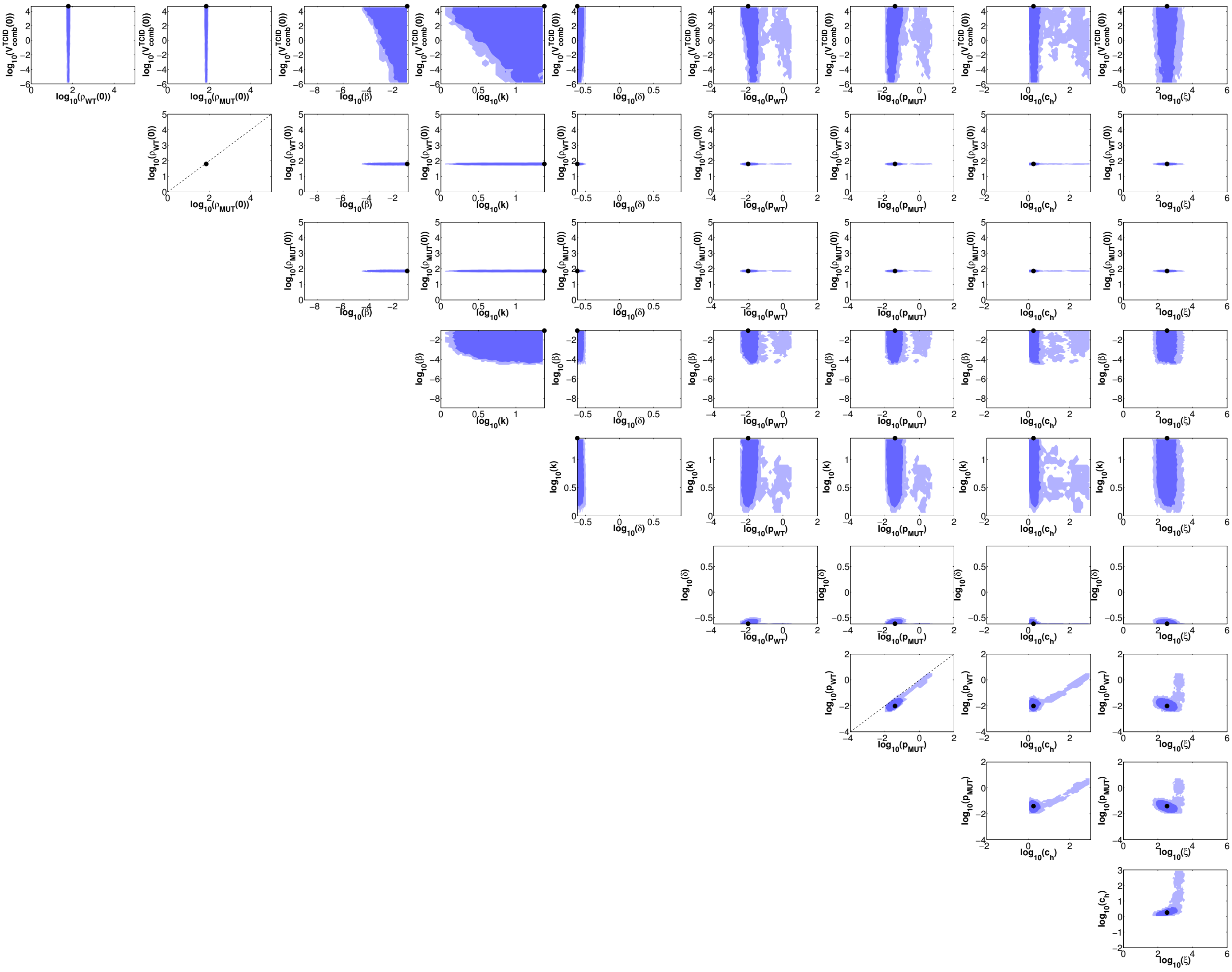

Figure S30: **LCR projections of the** p**-diff model fitted to the** ***rgNew17 OR vs. rgNew17 I241V OR*** **dataset.** Same as Figure S29, except for the p-diff model fitted to the *rgNew17 OR vs. rgNew17 I241V OR* experiment.

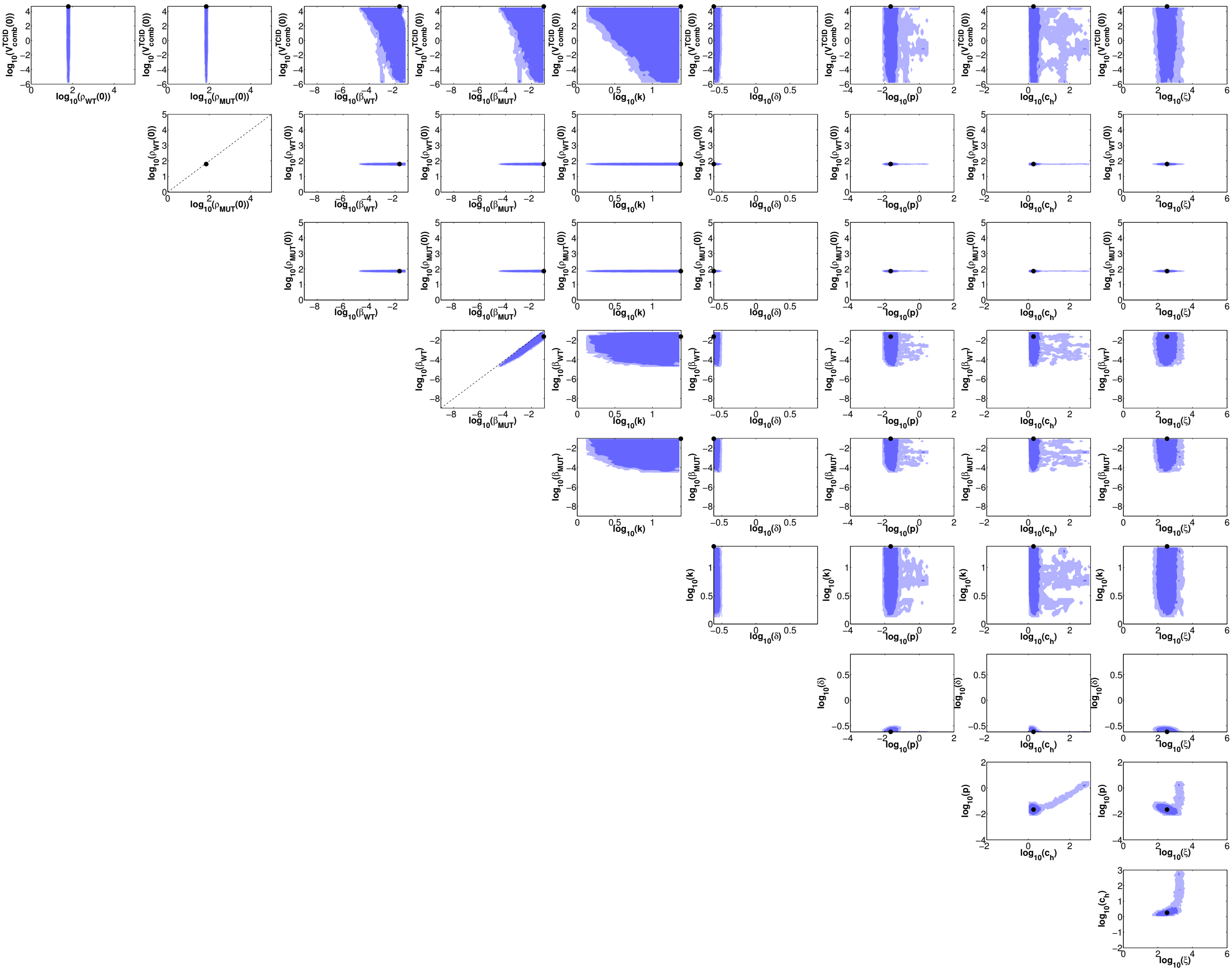

Figure S31: **LCR projections for the β-diff model fitted to the *rgNew17 OR vs. rgNew17 I241V OR* dataset.** Same as Figure S29, except for the β-diff model fitted to the *rgNew17 OR vs. rgNew17 I241V OR* dataset.

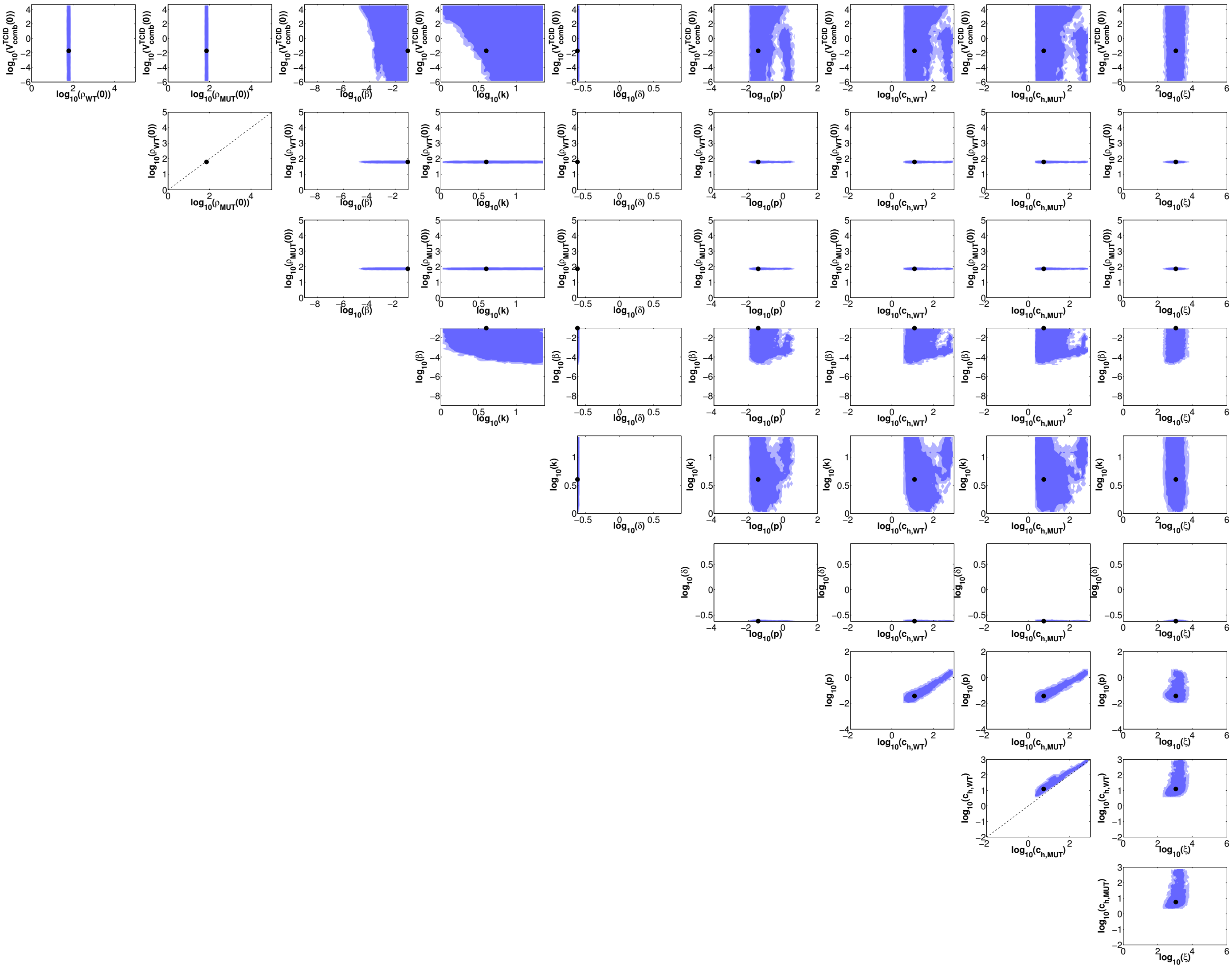

Figure S32: **LCR projections of the τ_V-diff model fitted to the *rgNew17 OR vs. rgNew17 I241V OR* dataset.** Same as Figure S29, except for the τ_V-diff model fitted to the *rgNew17 OR vs. rgNew17 I241V OR* experiment.

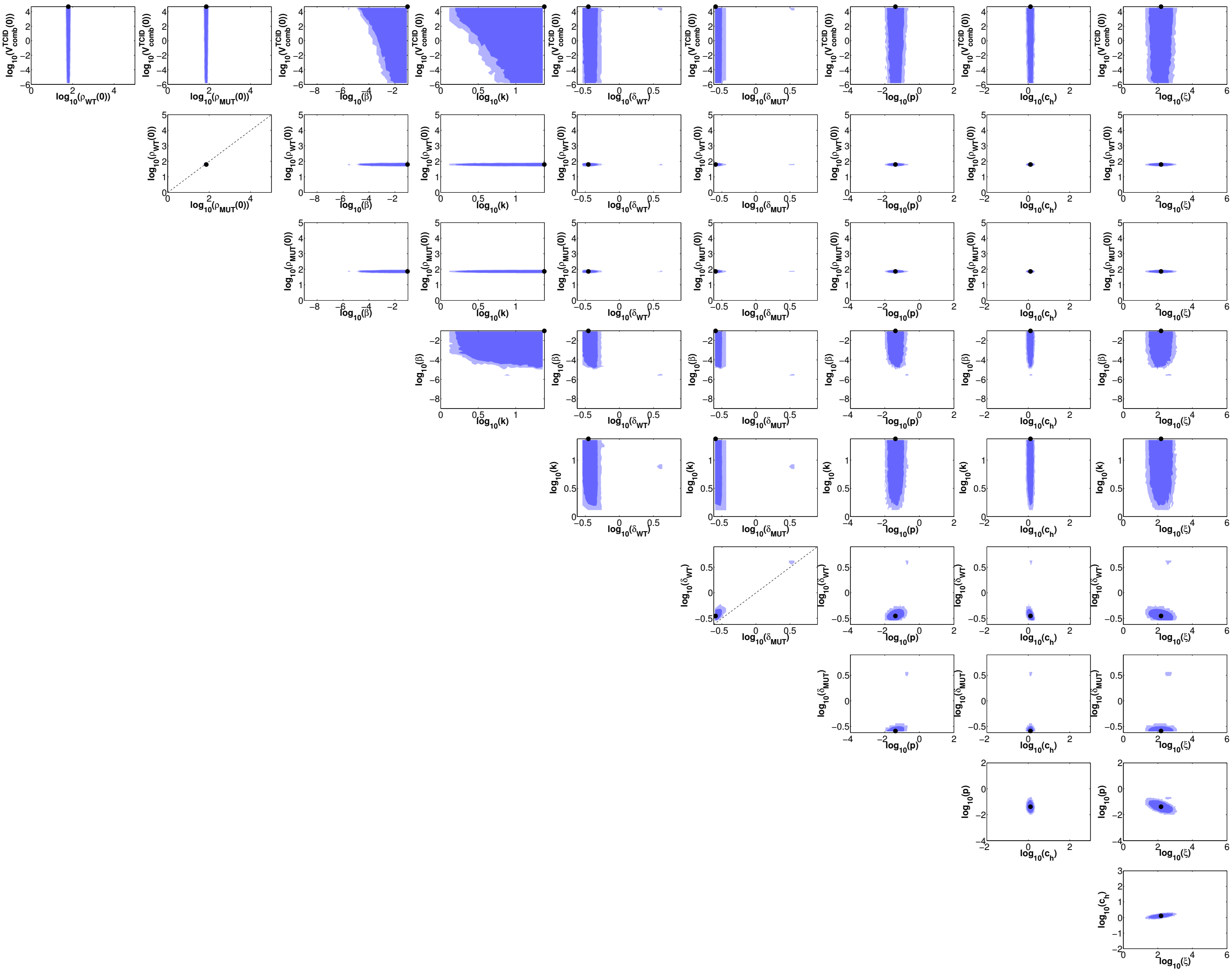

Figure S33: **LCR projections of the τ_I-diff model fitted to the *rgNew17 OR vs. rgNew17 I241V OR* dataset.** Same as Figure S29, except for the τ_I-diff model fitted to the *rgNew17 OR vs. rgNew17 I241V OR* experiment.

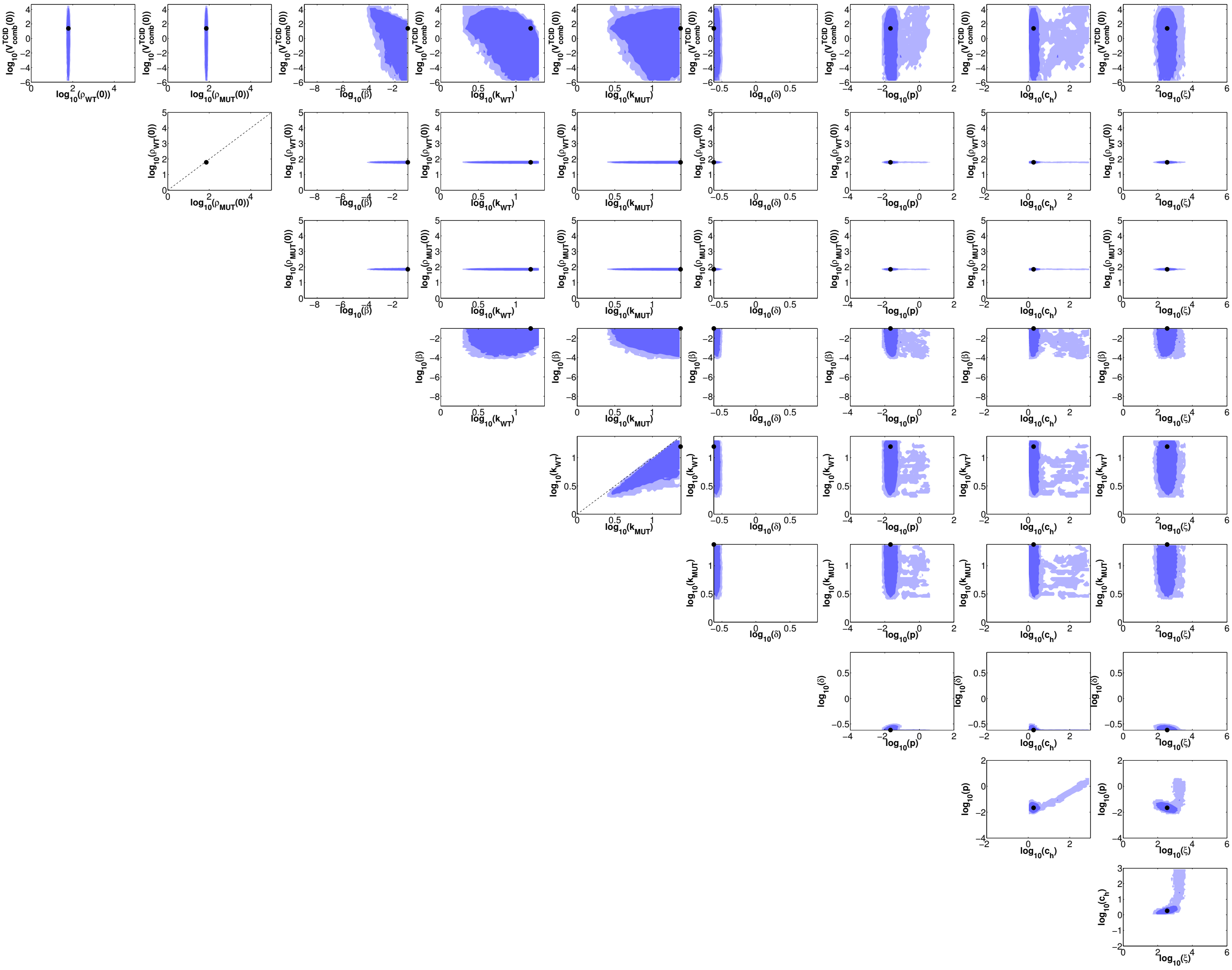

Figure S34: **LCR projections of the** ***k*****-diff model fitted to the** ***rgNew17 OR vs. rgNew17 I241V OR*** **dataset.** Same as Figure S29, except for the *k*-diff model fitted to the *rgNew17 OR vs. rgNew17 I241V OR* experiment.

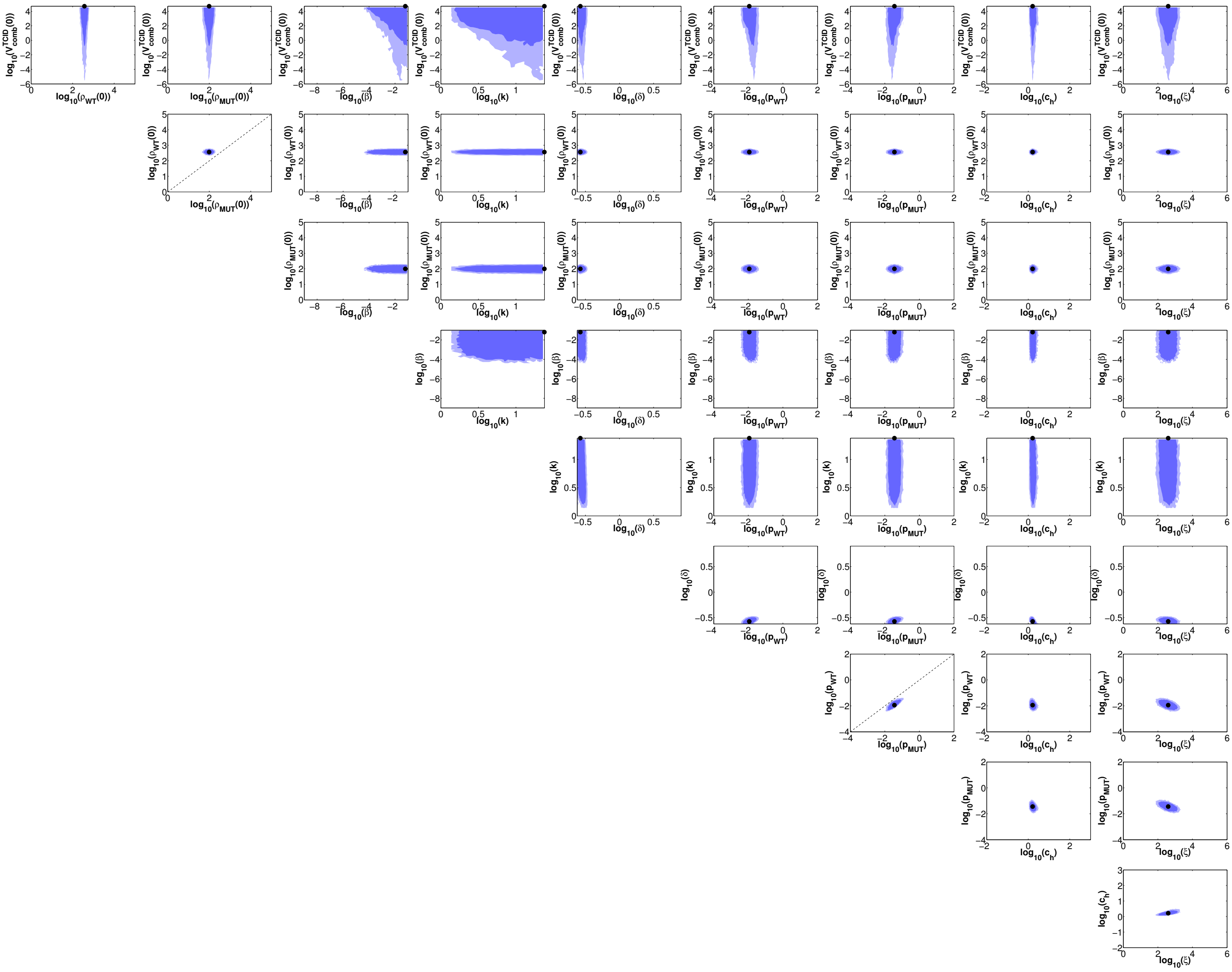

Figure S35: **LCR projections of the p-diff model fitted to the *rgNew17 OR vs. rgNew17 K369N OR* dataset.** Same as Figure S29, except for the p-diff model fitted to the *rgNew17 OR vs. rgNew17 K369N OR* experiment.

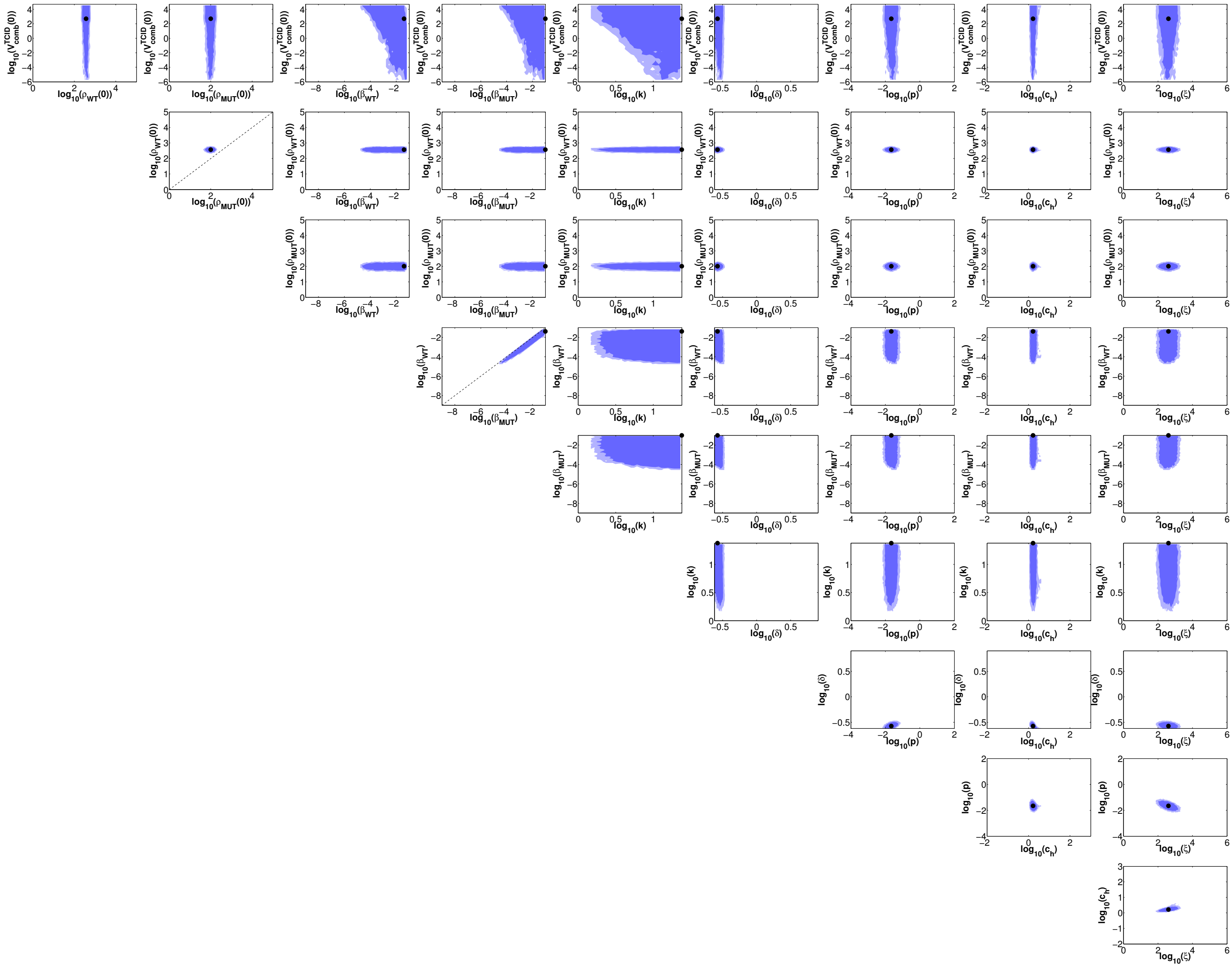

Figure S36: **LCR projections for the β-diff model fitted to the *rgNew17 OR vs. rgNew17 K369N OR* dataset.** Same as Figure S29, except for the β-diff model fitted to the *rgNew17 OR vs. rgNew17 K369N OR* dataset.

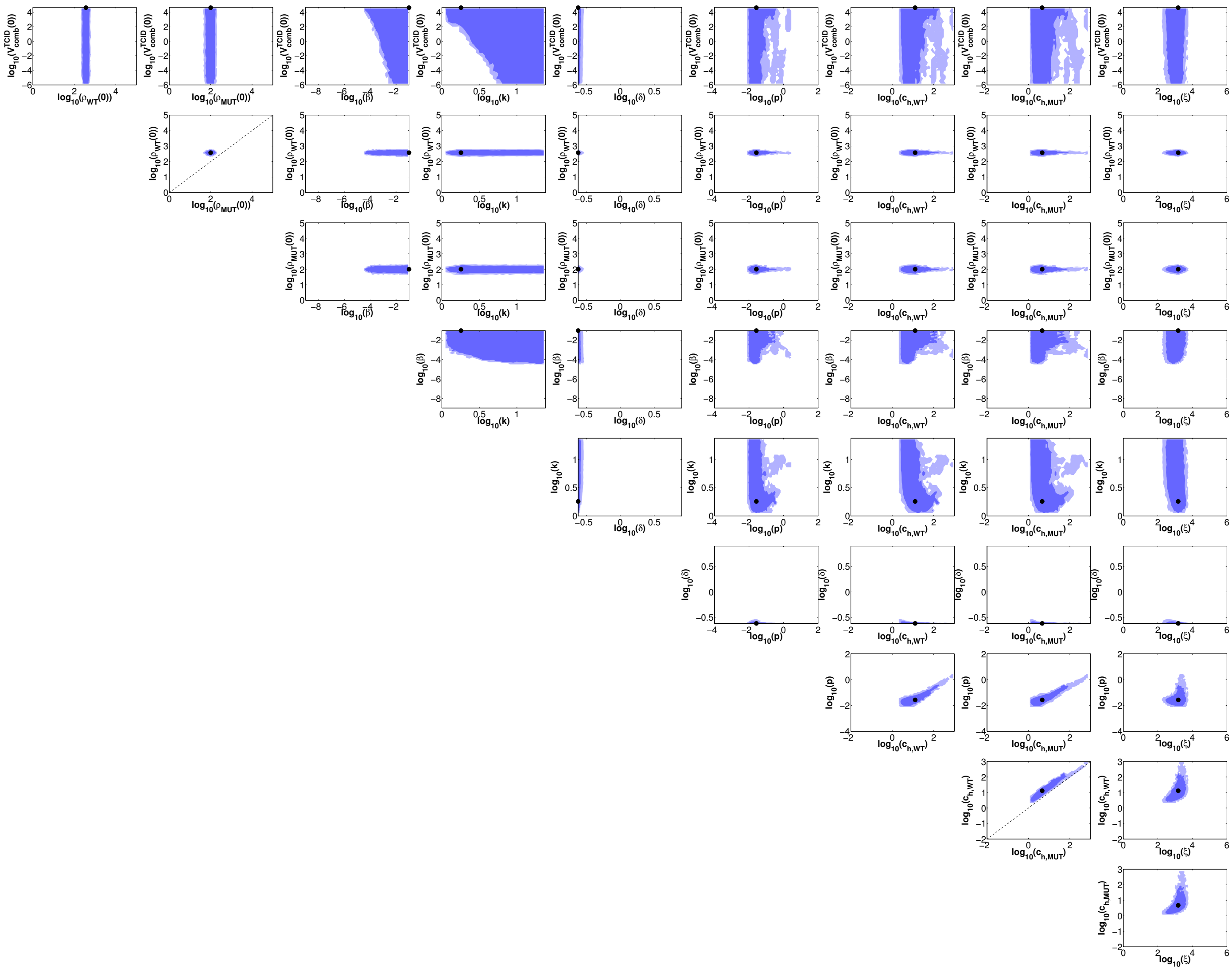

Figure S37: **LCR projections of the τ_V-diff model fitted to the *rgNew17 OR vs. rgNew17 K369N OR* dataset.** Same as Figure S29, except for the τ_V-diff model fitted to the *rgNew17 OR vs. rgNew17 K369N OR* experiment.

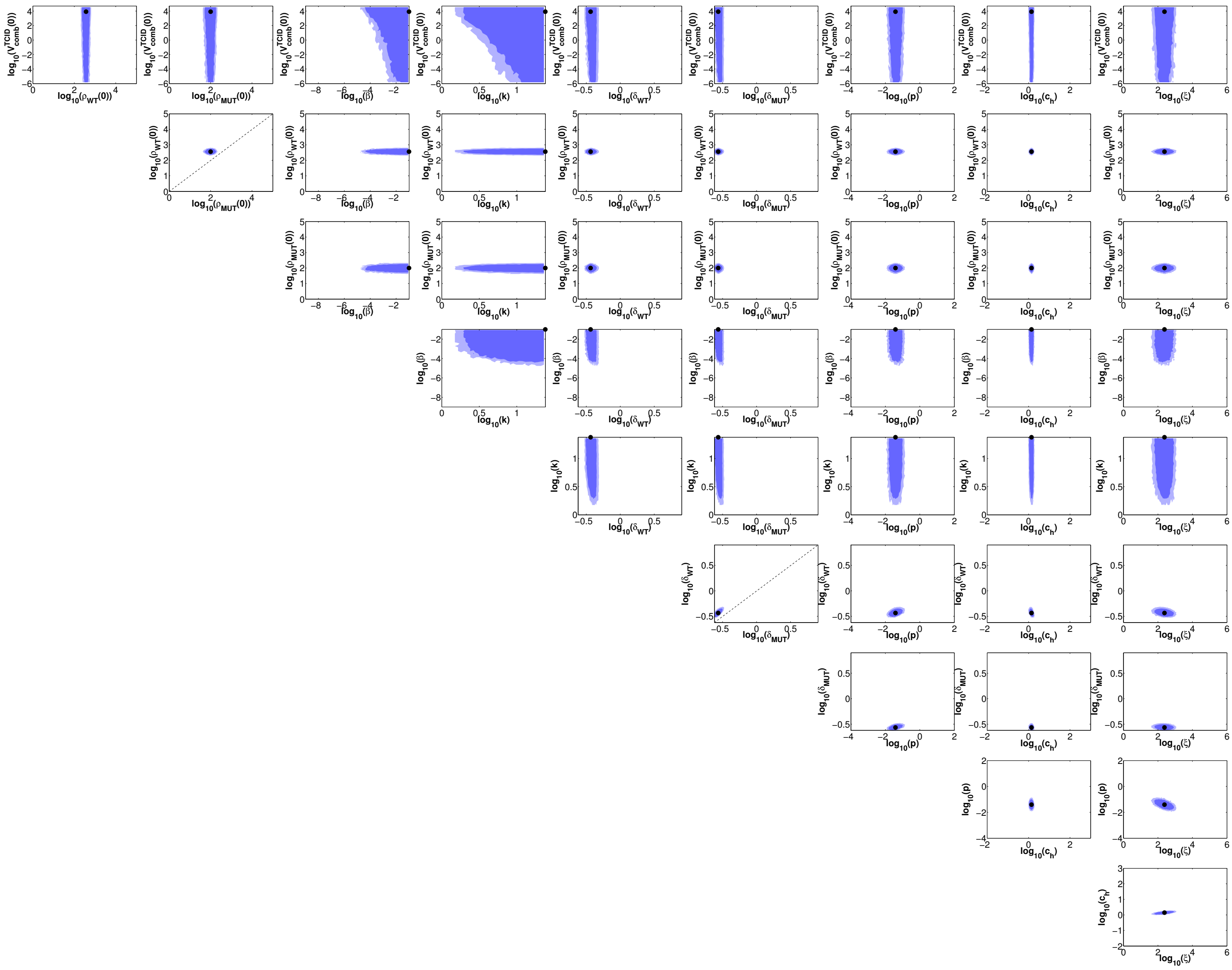

Figure S38: **LCR projections of the τ_I-diff model fitted to the *rgNew17 OR vs. rgNew17 K369N OR* dataset.** Same as Figure S29, except for the τ_I-diff model fitted to the *rgNew17 OR vs. rgNew17 K369N OR* experiment.

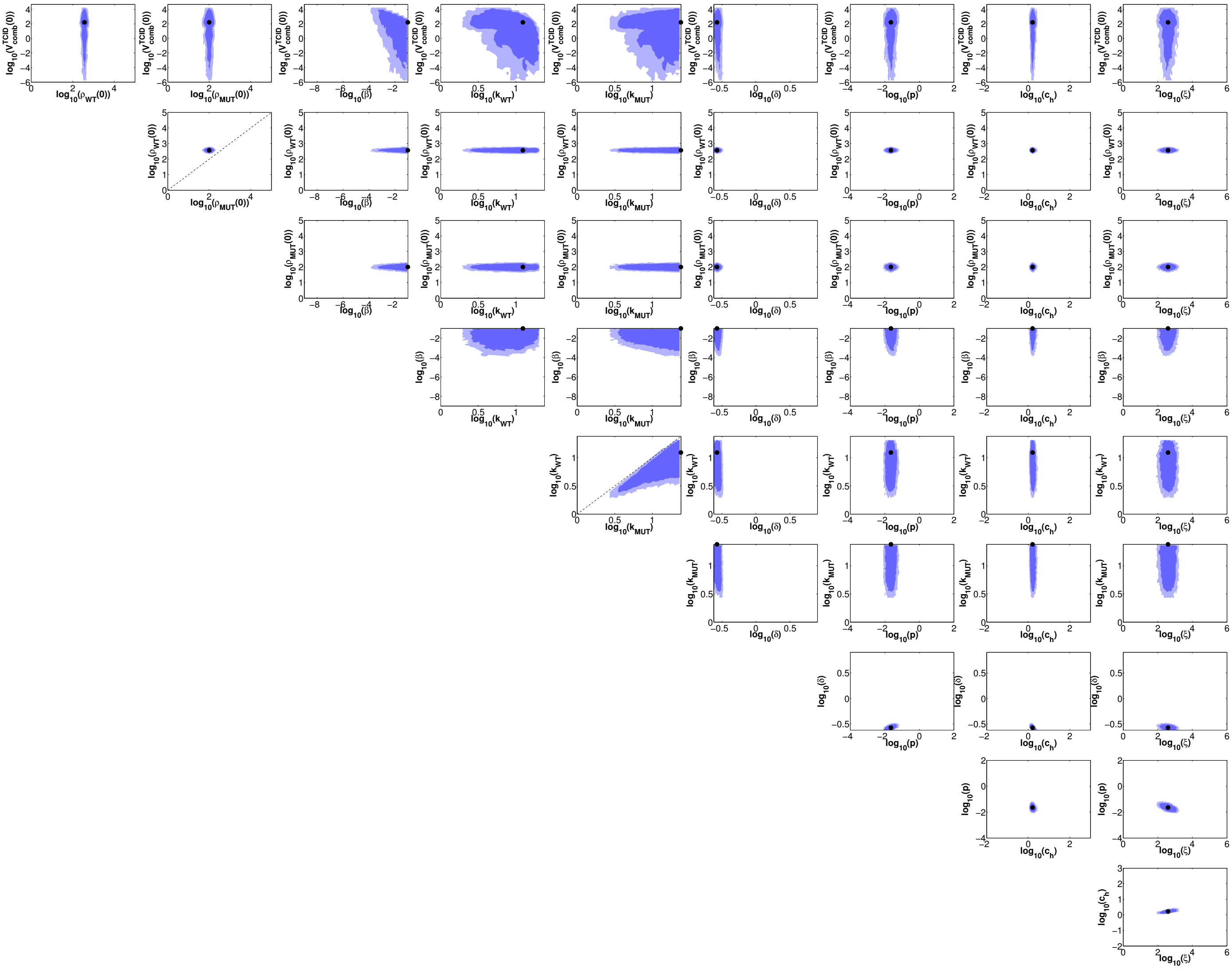

Figure S39: **LCR projections of the *k*-diff model fitted to the *rgNew17 OR vs. rgNew17 K369N OR* dataset.** Same as Figure S29, except for the *k*-diff model fitted to the *rgNew17 OR vs. rgNew17 K369N OR* experiment.

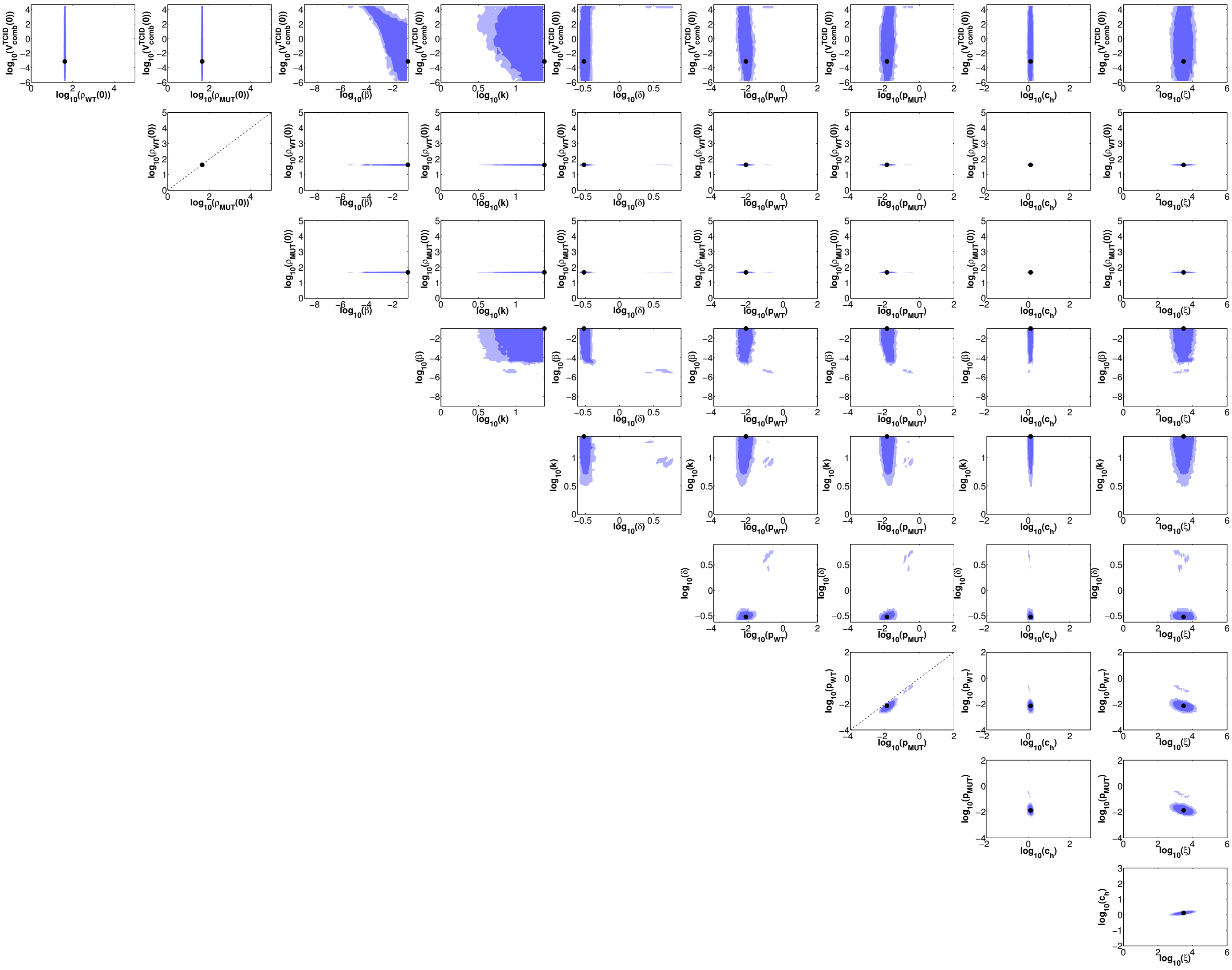

Figure S40: **LCR projections of the** p**-diff model fitted to the *rgNew17 OR vs. rgNew17 I241V, K369N OR* dataset.** Same as Figure S29, except for the p-diff model fitted to the *rgNew17 OR vs. rgNew17 I241V, K369N OR* experiment.

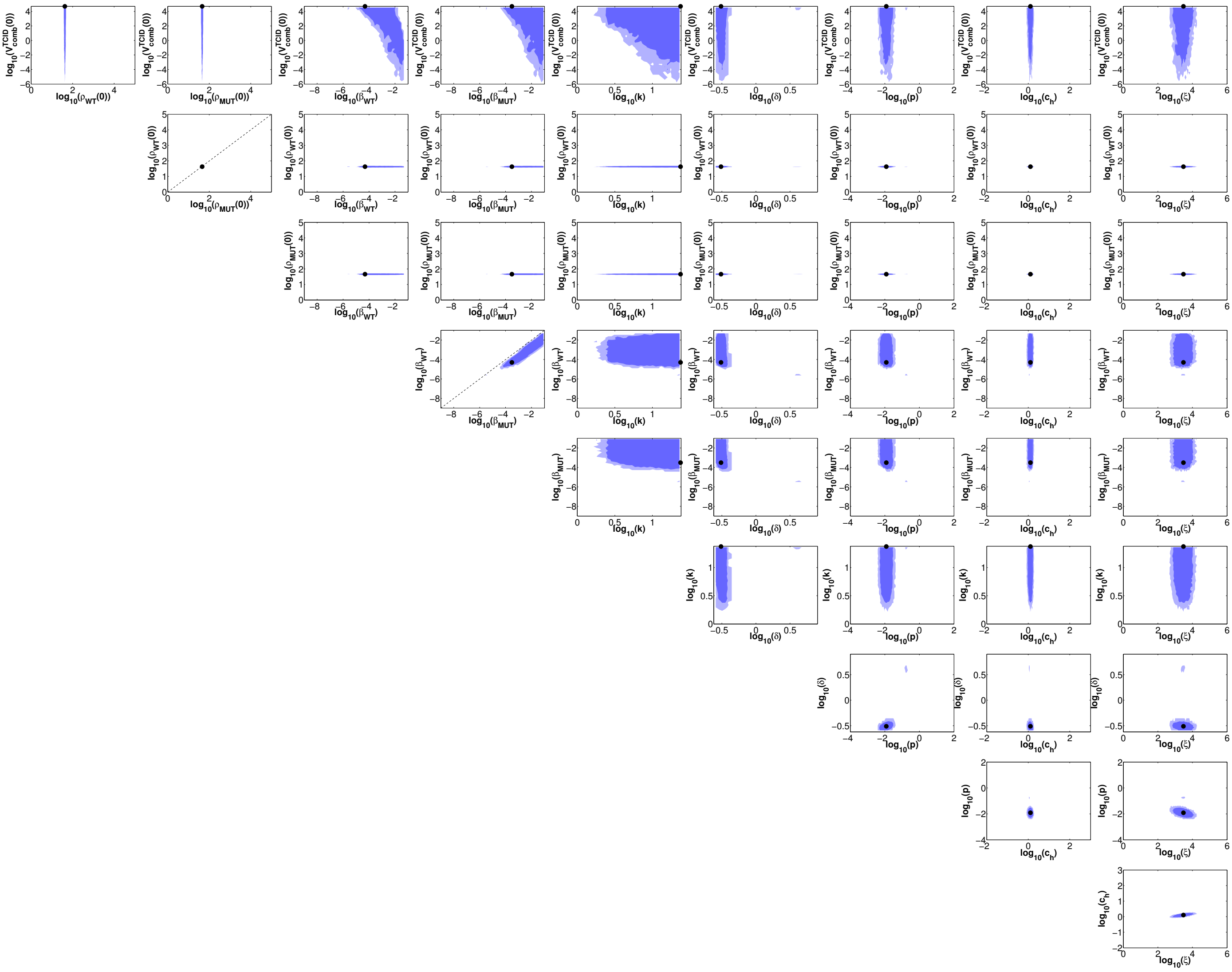

Figure S41: **LCR projections for the β-diff model fitted to the *rgNew17 OR vs. rgNew17 I241V, K369N OR* dataset.** Same as Figure S29, except for the β-diff model fitted to the *rgNew17 OR vs. rgNew17 I241V, K369N OR* dataset.

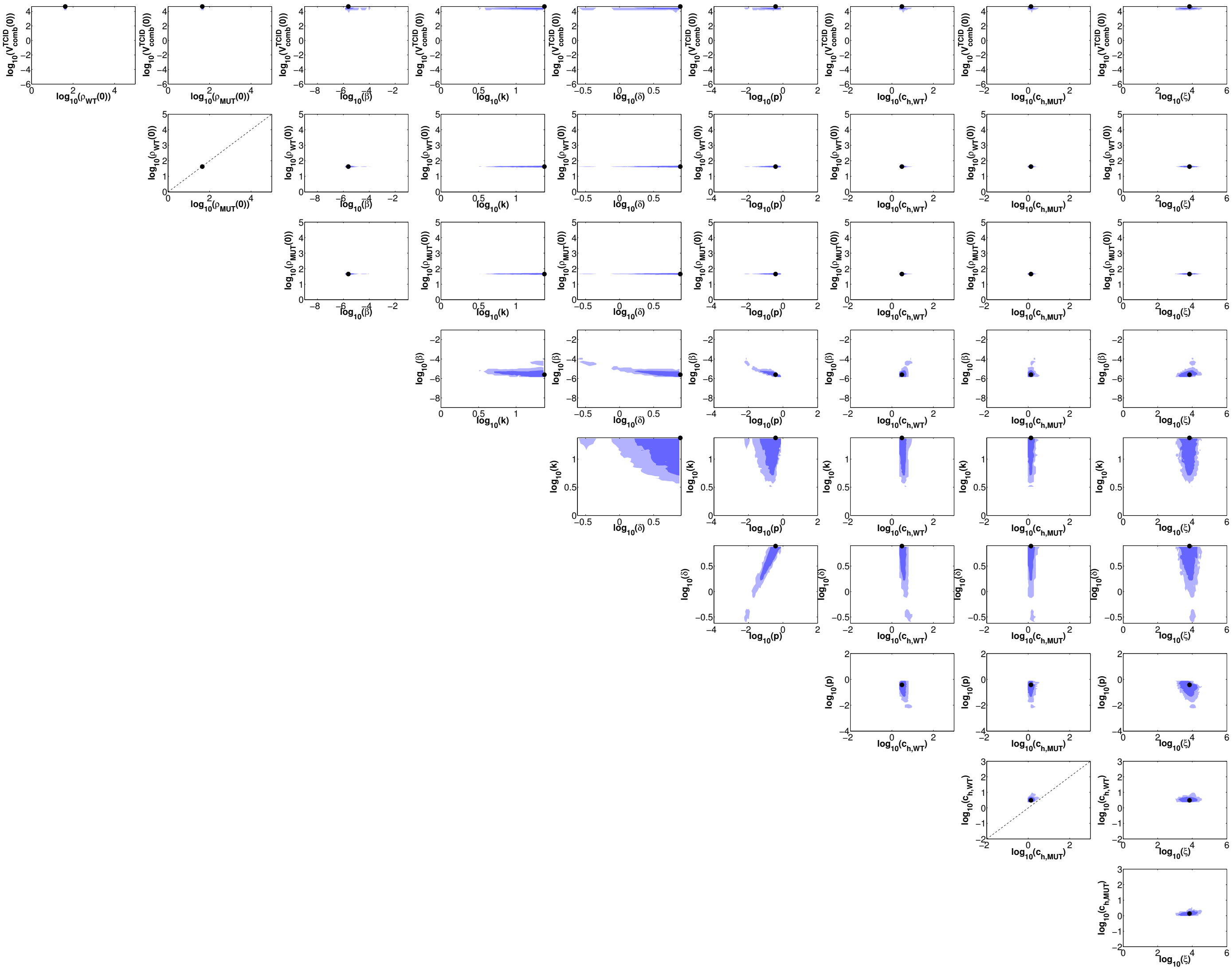

Figure S42: **LCR projections of the τ_V-diff model fitted to the *rgNew17 OR vs. rgNew17 I241V, K369N OR* dataset.** Same as Figure S29, except for the τ_V-diff model fitted to the *rgNew17 OR vs. rgNew17 I241V, K369N OR* experiment.

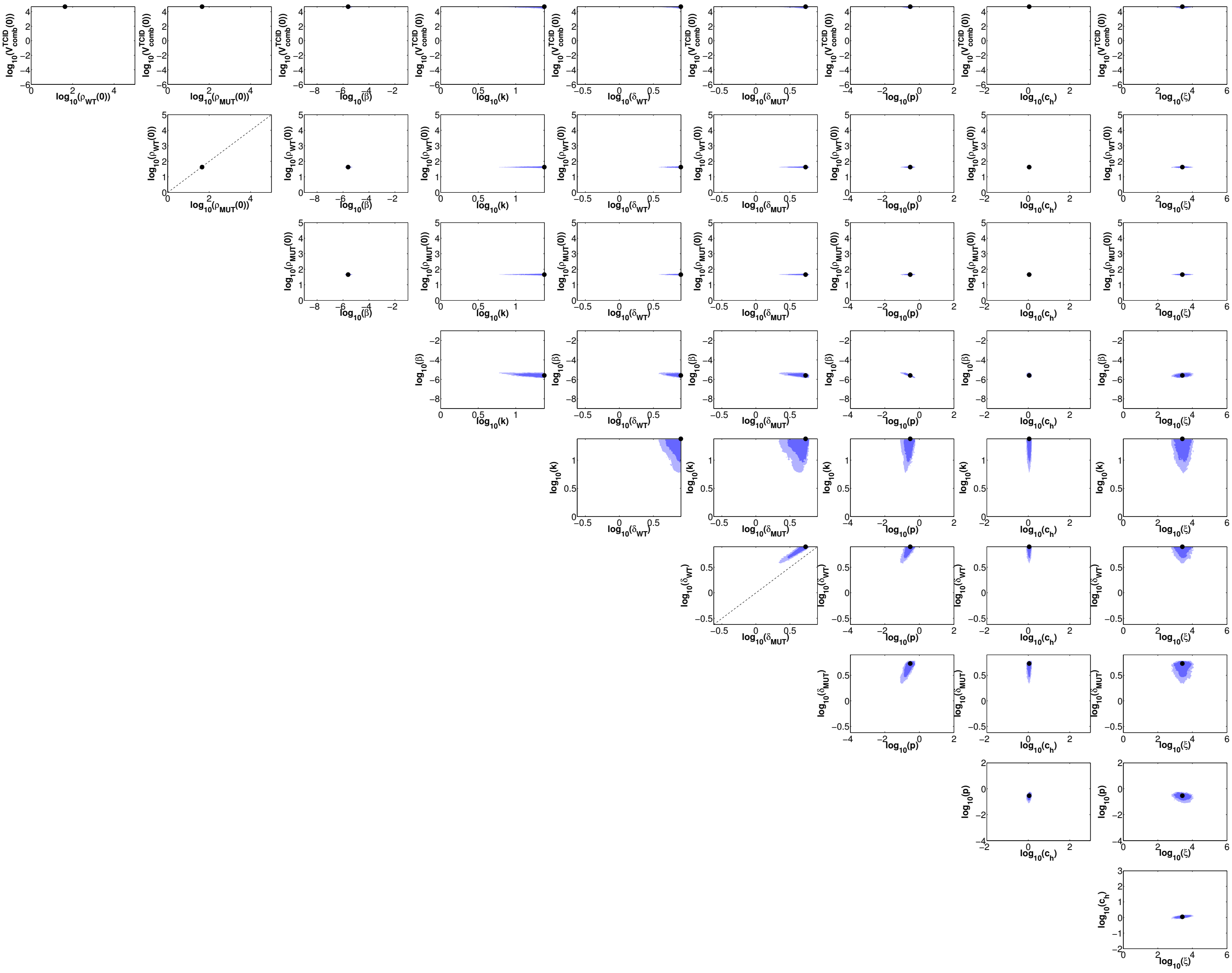

Figure S43: **LCR projections of the τ_I-diff model fitted to the *rgNew17 OR vs. rgNew17 I241V, K369N OR* dataset.** Same as Figure S29, except for the τ_I-diff model fitted to the *rgNew17 OR vs. rgNew17 I241V, K369N OR* experiment.

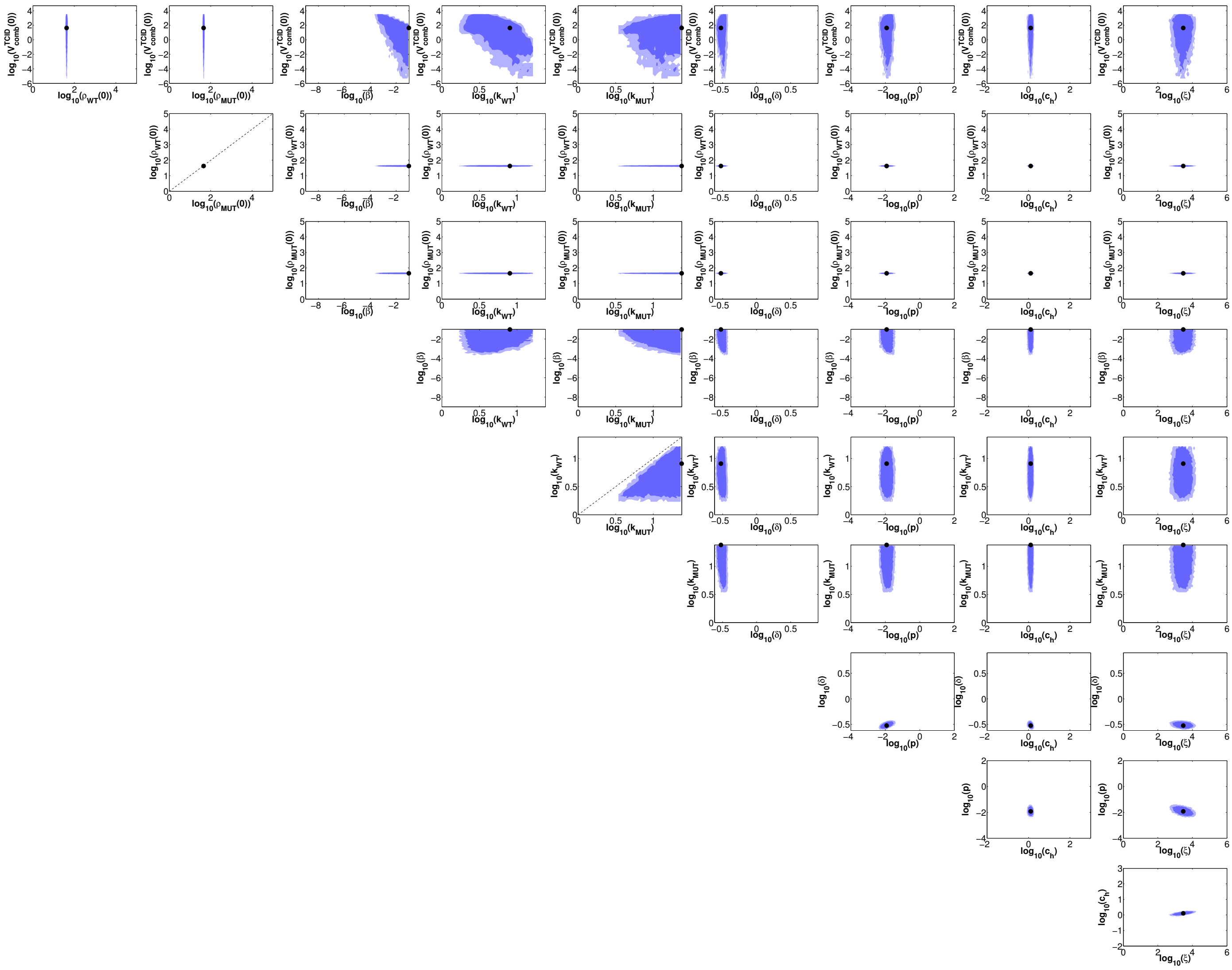

Figure S44: **LCR projections of the k-diff model fitted to the *rgNew17 OR vs. rgNew17 I241V, K369N OR* dataset.** Same as Figure S29, except for the k-diff model fitted to the *rgNew17 OR vs. rgNew17 I241V, K369N OR* experiment.

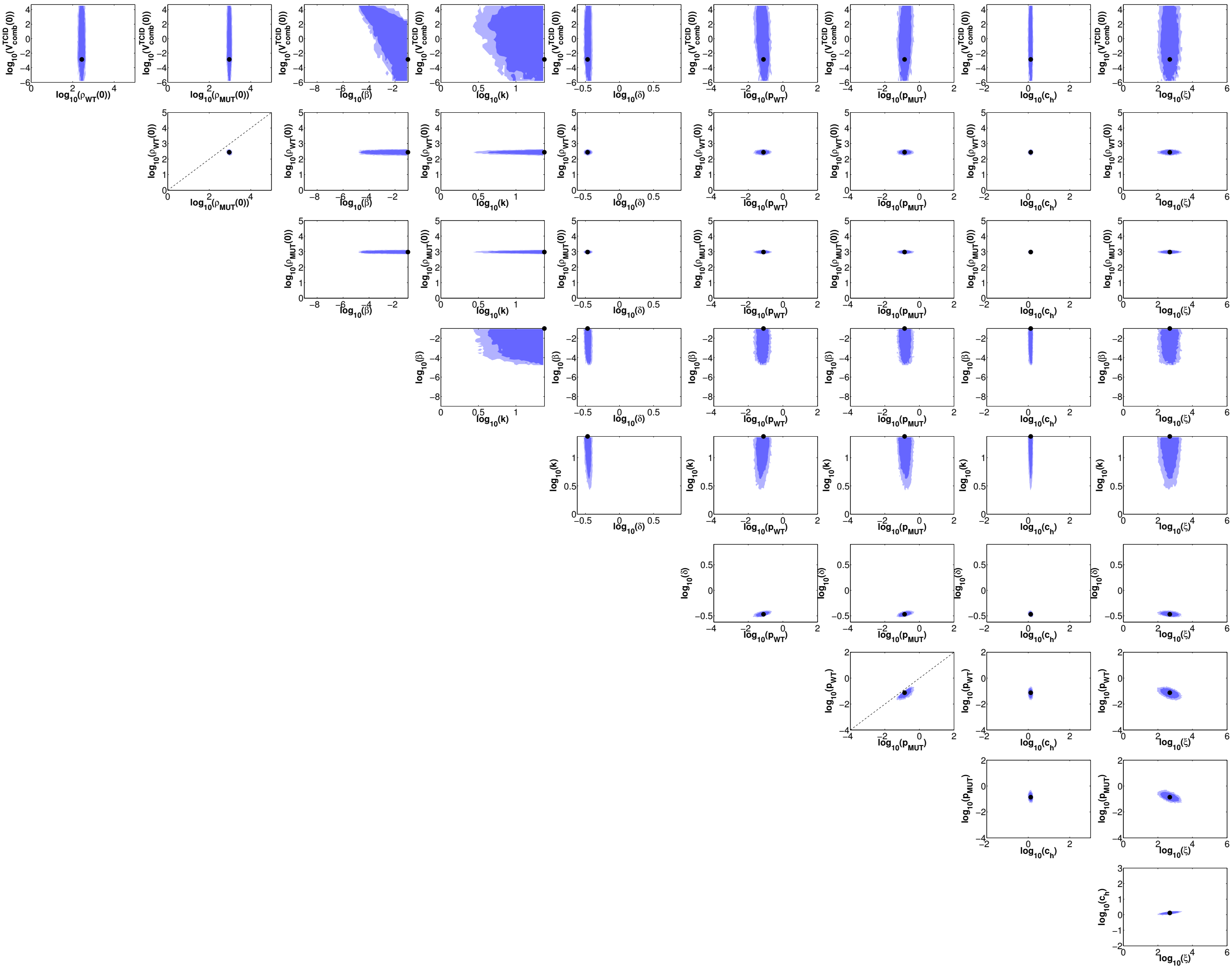

Figure S45: **LCR projections of the p-diff model fitted to the *rgPerth261 V241I, N369K OR vs. rgPerth261 OR* dataset.** Same as Figure S29, except for the p-diff model fitted to the *rgPerth261 V241I, N369K OR vs. rgPerth261 OR* experiment.

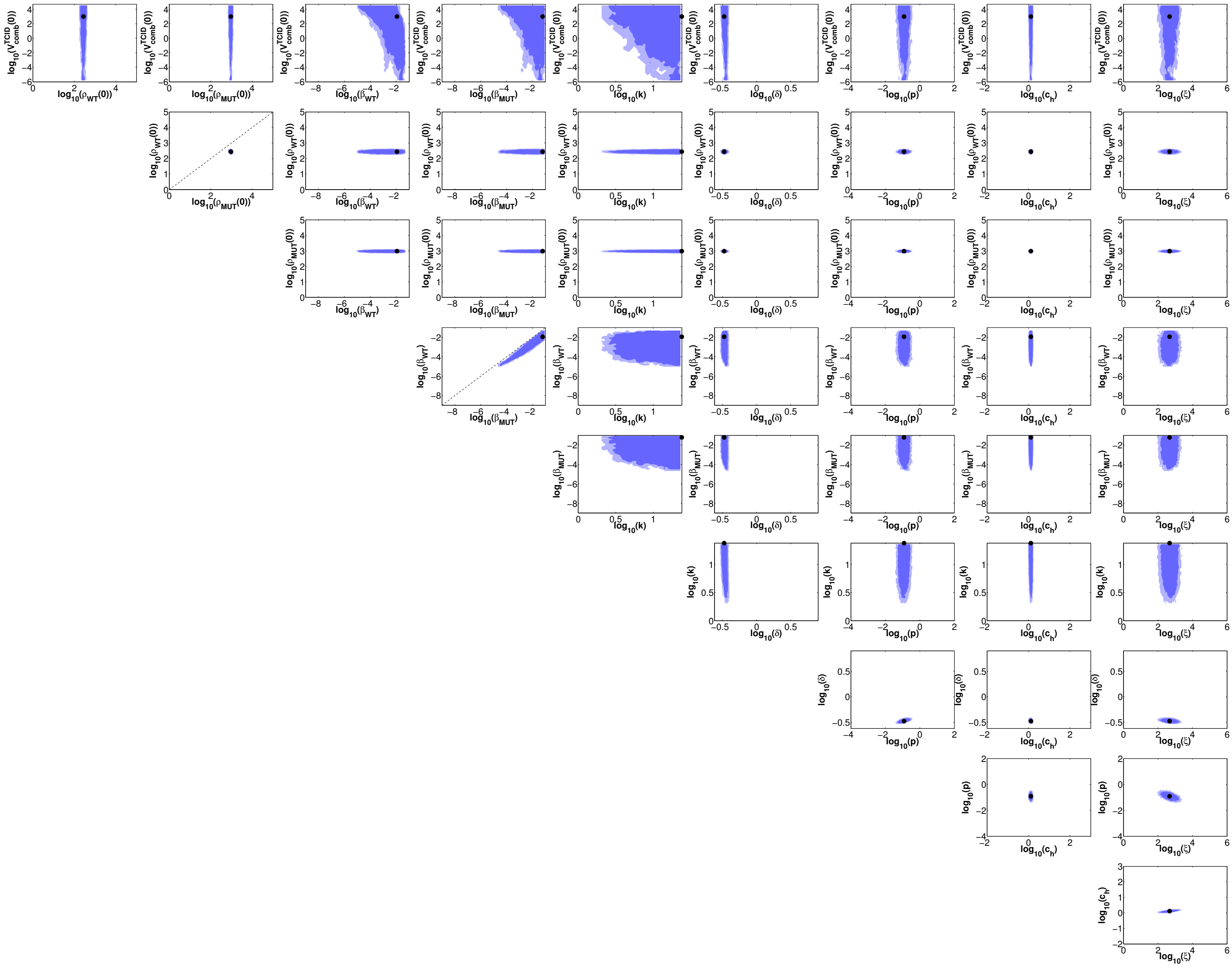

Figure S46: **LCR projections for the β-diff model fitted to the *rgPerth261 V241I, N369K OR vs. rgPerth261 OR* dataset.** Same as Figure S29, except for the β-diff model fitted to the *rgPerth261 V241I, N369K OR vs. rgPerth261 OR* dataset.

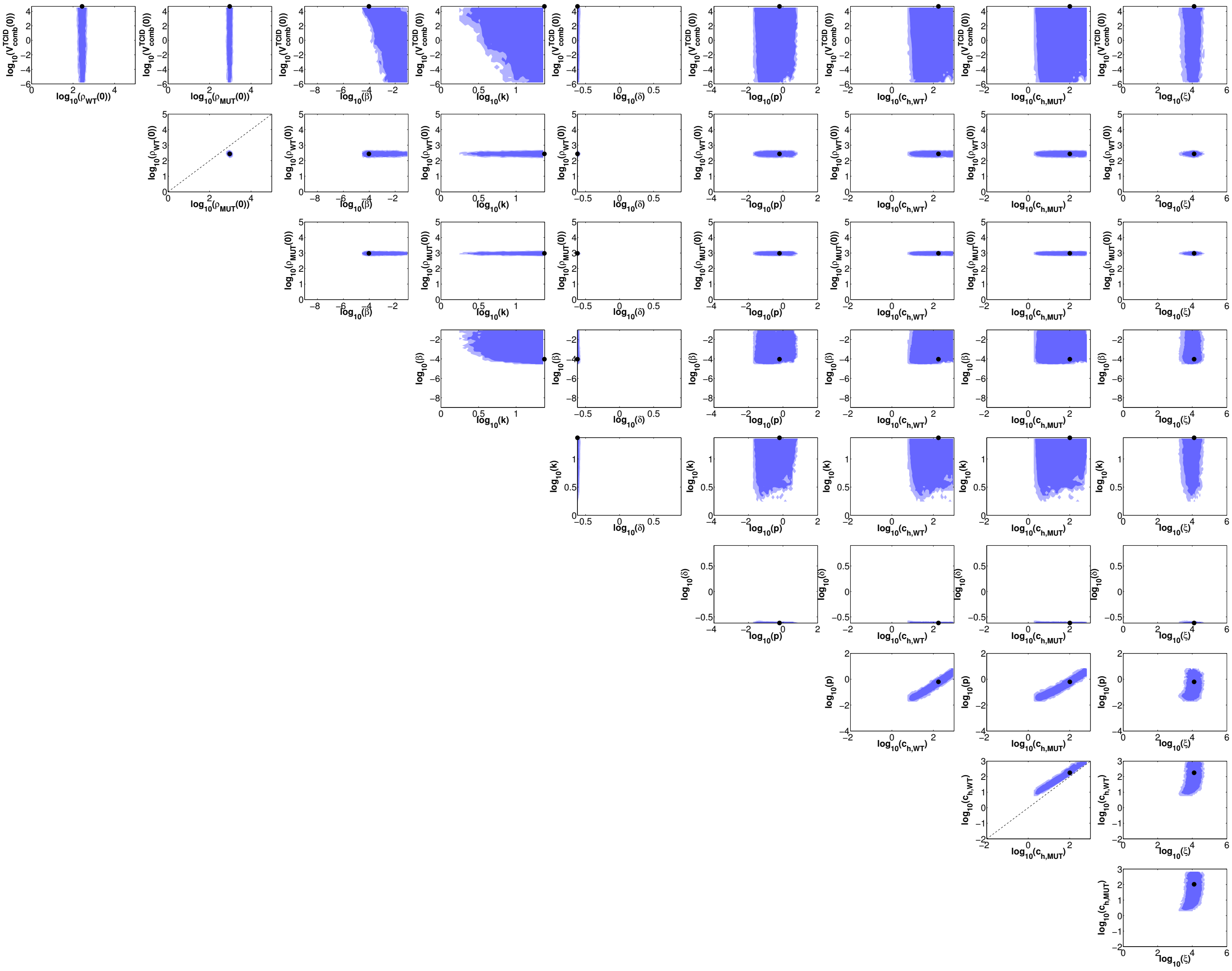

Figure S47: **LCR projections of the τ_V-diff model fitted to the *rgPerth261 V241I, N369K OR vs. rgPerth261 OR* dataset.** Same as Figure S29, except for the τ_V-diff model fitted to the *rgPerth261 V241I, N369K OR vs. rgPerth261 OR* experiment.

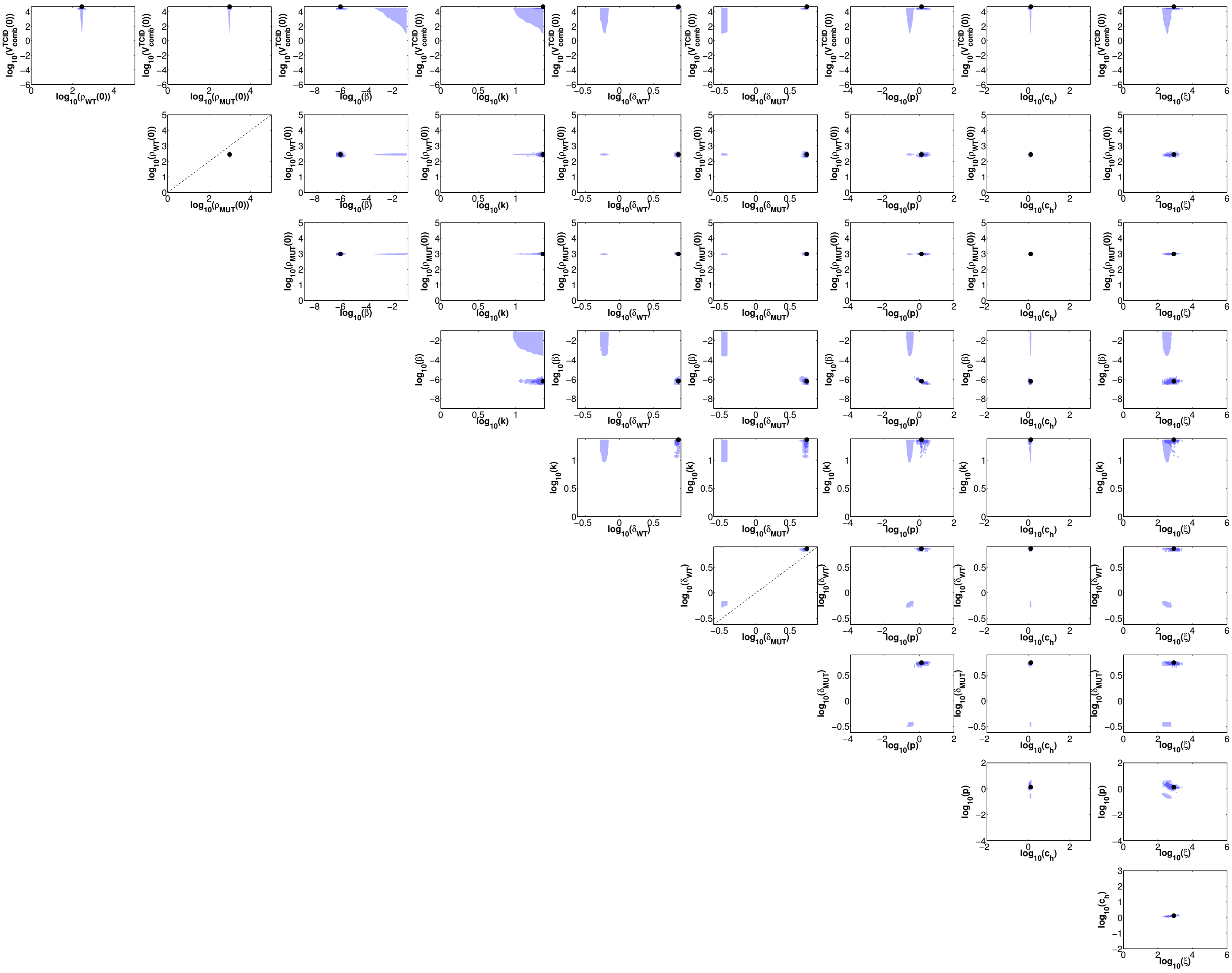

Figure S48: **LCR projections of the τ_I-diff model fitted to the *rgPerth261 V241I, N369K OR vs. rgPerth261 OR* dataset.** Same as Figure S29, except for the τ_I-diff model fitted to the *rgPerth261 V241I, N369K OR vs. rgPerth261 OR* experiment.

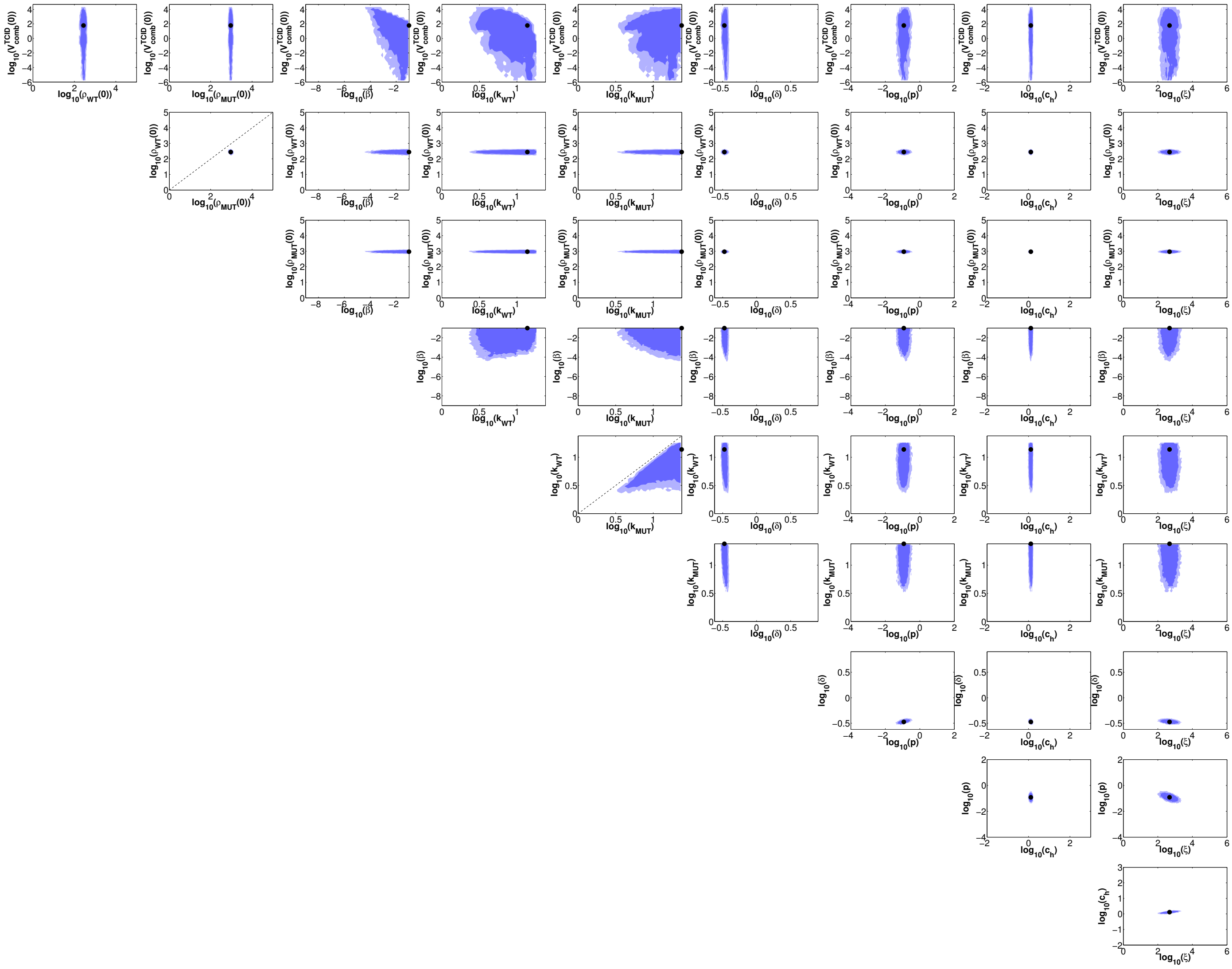

Figure S49: **LCR projections of the *k*-diff model fitted to the *rgPerth261 V241I, N369K OR vs. rgPerth261 OR* dataset.** Same as Figure S29, except for the *k*-diff model fitted to the *rgPerth261 V241I, N369K OR vs. rgPerth261 OR* experiment.